HELSINKI UNIVERSITY OF TECHNOLOGY
Department of Electrical and Communications Engineering

Uula Kantojärvi

Feature-specific on-board technology for airborne spectral imaging

Master's Thesis submitted in partial fulfilment of the requirements for the degree of Master of Science in Technology.

Espoo, October 23, 2006

Supervisor: Prof. Martti Hallikainen, Helsinki University of Technology

Instructor: Dr. Tech. Heikki Saari, VTT Technical Research Centre of Finland

HELSINKI UNIVERSITY OF TECHNOLOGY

ABSTRACT OF THE MASTER'S THESIS

Author:	Uula Kantojärvi
Title:	Feature-specific on-board technology for airborne spectral imaging
Date:	October 23, 2006 **Number of pages:** 81 + 29
Department:	Department of Electrical and Communications Engineering
Professorship:	S-92 Space Engineering
Supervisor:	Prof. Martti Hallikainen
Instructor:	Dr. Tech. Heikki Saari

This thesis describes the feasibility of a novel concept utilising on-board optical data processing for airborne spectral imaging. The main goal was to characterise the laboratory version of the instrument with the aid of simulations and measurements. Compared with traditional imaging spectrometers, this instrument radically reduces data processing time and data input, thus enabling real-time recognition and analysis. The instrument can be used in applications where the algorithm is known beforehand.

A mathematical model was developed for the instrument and its performance was evaluated in order to compare different concept variations. All components were measured and characterised individually, and the results were used in the simulations. Performance was then analysed by means of radiometric throughput and spatial and spectral resolutions. The simulations were performed at wavelengths of 450 nm to 900 nm. The throughput was found to be between 1% and 4.5%.

The set-up was characterised using a neon lamp and slit at a distance of two and a half metres. The measurements were performed on-axis at wavelengths between 600 nm and 680 nm. There was good correlation between the simulations and measurements. The spectral resolution was found to be 3 nm. For a modulation of 20%, the spatial frequency on the image sensor was 24 lp/mm.

The results show that the concept is suitable for feature-specific airborne spectral imaging thanks to its good spectral resolution and reasonable radiometric throughput and spatial resolution.

Keywords: optical data processing, spectral imaging, hyperspectral, spatial light modulation, LCD

TEKNILLINEN KORKEAKOULU DIPLOMITYÖN TIIVISTELMÄ

Tekijä:	Uula Kantojärvi		
Työn nimi:	Kohdeominainen tekniikka lentokoneesta suoritettavaan spektraaliseen kuvantamiseen		
Päivämäärä:	23.10.2006	**Sivuja:**	81 + 29
Osasto:	Sähkö- ja tietoliikennetekniikan osasto		
Professuuri:	S-92 Avaruustekniikka		
Työn valvoja:	Prof. Martti Hallikainen		
Työn ohjaaja:	TkT Heikki Saari		

Tässä työssä tutkitaan optisen datan käsittelykonseptin toimivuus lentokoneesta tapahtuvaan spektraaliseen kuvantamiseen. Laboratoriolaitteen suorituskyky määritettiin simulointien ja mittauksien avulla. Nykyisissä kuvaavissa spektrometreissä suurimmat ongelmat ovat kertyvä suuri datan määrä sekä sen pitkä käsittelyaika. Tässä laitteessa nämä molemmat ongelmat on poistettu mahdollistaen reaaliaikaisen tunnistamisen ja analysoinnin. Laite käy sovelluksiin, joissa tiedetään datan käsittelyalgoritmi jo etukäteen.

Erilaisten konseptivaihtoehtojen suorituskykyä vertailtiin tässä työssä kehitetyllä matemaattisella mallilla. Yksittäiset komponentit mitattiin ja tuloksia käytettiin mallissa, jolla simuloitiin laboratoriolaitteen suorituskykyä. Määritettävät ominaisuudet olivat kokonaisvalotehon läpäisy sekä paikka- ja spektrierottelukyky. Simuloinnit suoritettiin aallonpituuksien 450 nm ja 900 nm välillä. Kokonaisvalotehon läpäisy oli 1-4.5%.

Laboratoriolaitteen suorityskyky määritettiin käyttämällä neonlamppua sekä kapeaa rakoa kahden ja puolen metrin etäisyydellä. Mittaukset suoritettiin aallonpituuksien 600 nm ja 680 nm välillä. Mittaustulokset ja simuloinnit vastasivat toisiaan erittäin hyvin. Spektrierottelukyvyksi saatiin 3 nm. Modulaatio oli 20%, kun viivataajuus kuvasensorilla oli 24 lp/mm.

Tuloksien perusteella voidaan sanoa, että konsepti sopii hyvin spektraaliseen kuvantamiseen lentokoneesta. Etuja ovat hyvä spektrierottelukyky sekä kohtuullinen kokonaisvalotehon läpäisy ja paikkaerottelukyky.

Avainsanat: optinen datan käsittely, spektraalinen kuvantaminen, valon modulointi, LCD

Acknowledgements

The work described in this Master's Thesis was conducted at the Optical Sensors and Space Instruments team of VTT Technical Research Centre of Finland during 2006. The team is lead by Dr. Tech. Heikki Saari. The work was part of the project under the contract 19754/06/NL/PA of the European Space Agency (ESA). I would like to thank all project participants; VTT, ESA and Specim Ltd for giving me this opportunity to work on such an interesting and challenging task. Special thanks go to Dr. Bernd Harnisch from ESA for his encouragements and Mr. Esko Herrala from Specim for his advice and helping hand.

I would like to thank my instructor Dr. Tech. Heikki Saari for his advice and guidance during this work. I also give thanks to my supervisor Prof. Martti Hallikainen for accepting to supervise this work and for all his guidelines.

Many thanks go to all my fellow workers at the Optical Sensors and Space Instruments team for their help along this educative task. Special thanks go to Mr. Rami Mannila, Mr. Christer Holmlund and Mr. Jarkko Antila for their expert advice. I would also like to thank Mr. Pekka Teppola from VTT for the discussions concerning industrial applications.

I want to thank my family and friends for their support and encouragement during my studies and especially during this work.

Finally, I want to express my greatest thanks to my fiancée Teea for her love and patience.

Espoo, October 9, 2006

Uula Kantojärvi

Contents

Notations

A	area	[m^2]
A_{obj}	objective aperture size	[m^2]
c	speed of light in vacuum	[m/s]
C	contrast-ratio	
d	thickness	[m]
D	distance between mirrors	[m]
D_{ap}	aperture diameter	[m]
d_i	thickness of i:th element	[m]
d_1	thickness of first element	[m]
D_λ	dispersion	[nm/mm]
E	electric field strength	[V/m]
E_λ	spectral irradiance	[$Wm^{-1}nm^{-1}$]
f	focal length	[m]
F	fill-factor	
FOV	field-of-view	[rad]
$FWHM$	full-width at half-maximum	[m]
$f/\#$	f-number	
$GSD_{\|\|}$	along-track ground sampling distance	[m]

$GSD_{\perp}$	across-track ground sampling distance	[m]
h	Planck's constant	[Js]
H	flying altitude	[m]
H_{CCD}	image height on image sensor	[m]
H_{slit}	slit height	[m]
H_{SLM}	image height on SLM	[m]
i	index	
$IFOV_{\parallel}$	along-track instantaneous field-of-view	[rad]
$IFOV_{\perp}$	across-track instantaneous field-of-view	[rad]
I_{dark}	dark current	[rms e^-/s]
I_{λ}	spectral radiant intensity	[$Wsr^{-1}nm^{-1}$]
k	wavenumber	[m^{-1}]
K	camera gain	[e^-/ADU]
k_B	Boltzmann's constant	[Ws/K]
K_e	effective elastic constant	[N]
L_{λ}	spectral radiance	[$Wm^{-1}sr^{-1}nm^{-1}$]
$L_{\lambda,a}$	spectral radiance at objective	[$Wm^{-1}sr^{-1}nm^{-1}$]
m	modulation	
M	optics magnification	
MTF	modulation transfer function	
M_{λ}	spectral exitance	[$Wm^{-1}nm^{-1}$]
n_e	refractive index of extraordinary ray	
$n_{electrons}$	number of electrons	
n_o	refractive index of ordinary ray	

$n_{photons}$	number of photons	
Δn	birefringence	
N	integer	
N_c	number of components	
N_i	pixel number of i:th pixel	
N_{offset}	pixel number offset	
N_s	number of spatial points	
OTF	optical transfer function	
OTF_i	optical transfer function of i:th component	
POL	pixel overlapping	
PSF	point spread function	
PSF_i	point spread function of i:th component	
$PSF_{i,i+1}$	point spread function of two serial components	
p	edge steepness parameter	
ΔP_{CCD}	image sensor pixel pitch	[m]
ΔP_{SLM}	SLM pixel pitch	[m]
q	number of elements	
Q	radiant energy	[J]
r	retardance	[rad]
s	spatial position	[m]
S	signal	[ADU]
SNR	signal-to-noise ratio	
s_{max}	maximum spatial position	[m]
S_{max}	maximum signal	[ADU]

s_{min}	minimum spatial position	[m]
S_{min}	minimum signal	[ADU]
s_1	mirror distance from optical axis	[m]
s_2	distance between aperture and image plane	[m]
Δs	spatial position step	[m]
t	time	[s]
T	transmission	
T_B	temperature of black body	[K]
T_i	transmission of i:th component	
t_{int}	integration time	[s]
$t_{int,max}$	maximum integration time	[s]
T_{LCD}	transmission of LCD for linear polarised light	
T_p	transmission of single polariser for linear polarised light	
$T_{\parallel}$	transmission of two parallel polarisers	
$T_{\parallel,p+LCD}$	transmission of two parallel polarisers and LCD	
$T_{\perp}$	transmission of two perpendicular polarisers	
T_θ	transmission of two polarisers as function of mutual rotation	
Δt	time delay	[s]
v	flying speed	[m/s]
W_{slit}	slit width	[m]
x	spatial dimension	[m]
y	spatial dimension	[m]
α	marginal ray angle	[°]
β	tilting angle	[°]

γ	rotation viscosity	[Ns/m]
ϵ_0	dielectric constant in vacuum	[F/m]
$\Delta\epsilon$	anisotropic dielectric constant	
η	quantum efficiency	
θ	rotation	[rad]
λ	wavelength	[m]
λ_i	wavelength on i:th pixel	[m]
$\Delta\lambda$	wavelength band	[m]
ν	spatial frequency	[lp/mm]
ν_N	Nyquist frequency	[lp/mm]
ν_s	sampling frequency	[lp/mm]
$\Delta\nu$	spatial frequency step	[lp/mm]
ρ	reflectance	
σ_{ro}	read-out noise	[rms e^-]
σ_{tot}	total noise	[rms e^-]
τ_{off}	off-response time	[s]
τ_{on}	on-response time	[s]
Φ_λ	spectral radiant flux	[W/nm]
$\Phi_{\lambda,i}$	spectral radiant flux after i:th component	[W/nm]
ψ	angle between normal and observation direction	[rad]
Ω	solid angle	[sr]

Abbreviations

ADU	Analogue to Digital conversion Unit
AOTF	Acousto-Optic Tunable Filter
AVIRIS	Airborne Visible/Infrared Imaging Spectrometer
CCD	Charge-Coupled-Device
ESA	European Space Agency
FOV	Field-of-View
FWHM	Full-Width at Half-Maximum
GSD	Ground Sampling Distance
HTPS	High-Temperature Polycrystalline Silicon
IFOV	Instantaneous Field-of-View
IR	Infrared
ISSI	Imaging Spectral Signature Instrument
LC	Liquid Crystal
LCD	Liquid Crystal Display
LCoS	Liquid Crystal on Silicon
LCTF	Liquid Crystal Tunable Filter
MMA	Micro-Mirror Array
MTF	Modulation Transfer Function

NIR	Near-Infrared
OTF	Optical Transfer Function
PCB	Printed Circuit Board
PGP	Prism-Grating-Prism
POL	Pixel Overlapping
PSF	Point Spread Function
RF	Radio Frequency
RMS	Root-Mean-Square
SLM	Spatial Light Modulator
SNR	Signal-to-Noise ratio
UV	Ultraviolet
1D	One-dimensional
2D	Two-dimensional
3D	Three-dimensional

List of Figures

List of Tables

Chapter 1

Introduction

Remote sensing concerns the collection of information of the Earth without direct contact [1]. Usually this information is related to natural resources or environment. Data is primarily collected by satellites and aircraft systems, but ground-based on-site measurements are also needed for calibration purposes. There are three main aims for remote sensing. First, to improve our ability to inventory and hence manage the Earth's natural resources. Second, to monitor changes in our environment. And third, to avoid political and economically ill-advised international trade of natural resources. In all of these cases, global information is essential and remote sensing systems are a means to acquire the required data.

1.1 Background

A traditional framing camera consists of the fore optics and an image sensor [2]. The fore optics creates the image of the target on the image sensor. A block diagram of a traditional framing camera is shown in Figure 1.1(a). The image sensor can be panchromatic or colour sensitive. The first one doesn't distinguish between different wavelengths, i.e. colours, and the image is shown in shades of grey. The latter detects three different colours; red, green and blue, and reproduces the image by combining these colour components.

An imaging spectrometer measures several narrow wavelength bands at the target location [2], i.e. it measures the spectrum of the target which is usually referred to as a spectral signature [1]. This way the spectral properties of the target can be examined and the target can be identified or at least distinguished. The amount of generated data is approximately 4 to 1000 times higher in comparison to the framing camera, depending on the number of wavelength bands used. Usually an imaging spectrometer contains

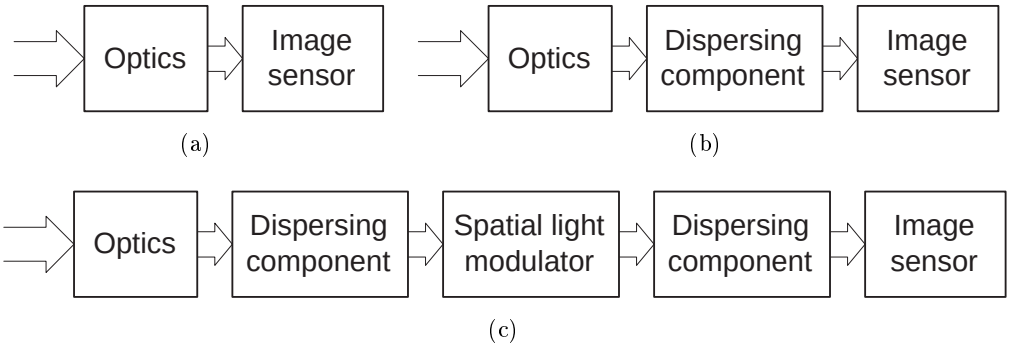

Figure 1.1. Different kinds of imaging instruments. (a) Traditional framing camera, (b) conventional imaging spectrometer and (c) spectral imaging instrument with on-board optical data processing.

a dispersing component that discriminates the wavelengths in a spatial dimension. A block diagram is shown in Figure 1.1(b). There are also many other methods to acquire the spectrum, which are discussed in Chapter 2.

The vision of imaging spectrometry originated from the geological disciplines [3]. Geologists who make maps have a direct need to identify and plot the outlines of geological units. Nowadays imaging spectrometers are used for target detection, material mapping, material identification and for mapping details of surface properties [4]. A common factor for all of these application areas is the huge amount of data that is acquired during a measurement session. Upcoming difficulties are the need for large data storage, slowness of data handling and complex and massive data processing algorithms.

In applications where the algorithm is known before the measurement session, the amount of data can be dramatically reduced using on-board optical data processing such that only the data that is needed is stored. Compared with traditional imaging spectrometers, this kind of instrument radically reduces data processing time and data input, thus enabling real-time recognition and analysis. A block diagram for the instrument is shown in Figure 1.1(c). The main idea is to disperse the spectrum, modulate it in the spectral domain and combine the spatially dispersed spectrum back to the spatial domain. The modulation is chosen to represent the feature-specific properties of a target such that only the desired targets are observed. The amount of stored data is the same as in a framing camera because the spectral data processing has already been carried out on-board. As a drawback, the optical data processing is an irreversible operation. Therefore, stored data can only be used for the beforehand planned purposes.

Possible applications for this kind of instrument may be the remote sensing of the Earth by means of thematic mapping of roads, water systems, forests and other objects that need to be recognised. There are numerous applications where the spectral signature of a target is already known and the target is desirable to be recognised by means of this signature.

There are also other application areas for the instrument in addition to airborne or spaceborne remote sensing. One possible application area could be the quality monitoring of a conveyor belt manufacturing process from the spectral point of view. Also, object recognition by means of spectral properties could be utilised. Slow and clumsy filter wheel or scanning mirror based measurement systems could be replaced with the fast spectral imaging system.

1.2 Objectives and Contents of Thesis

The objective of this thesis is to study the feasibility of a spectral imaging instrument with on-board optical data processing shown in Figure 1.1(c) by means of instrument simulations and breadboard characterisation measurements. The most interesting properties are spatial and spectral resolutions, radiometric throughput and the number of light modulation steps. The proposed spectral imaging instrument is later referred to as ISSI after Imaging Spectral Signature Instrument.

Remote sensing theories, previously built imaging spectrometers, available spectrograph techniques and applicable spatial light modulation techniques are studied in Chapter 2. Proposed novel instrument concepts are introduced and discussed in Chapter 3. Chapter 4 describes the characterisation measurements carried out for the ISSI components. The developed instrument performance simulator and simulations carried out for the proposed concepts are reported in Chapter 5. In Chapter 6 the adjustment procedure of the ISSI breadboard components is reported and performed characterisation measurements are analysed. Finally, Chapter 7 is devoted to discussions and further proposals while conclusions are presented in Chapter 8.

Additionally, measurement set-up photographs are shown in Appendix A and simulation parameters are listed in Appendix B. Also, more detailed figures showing measurement results are presented in Appendix C and information about filters is given in Appendix D.

All surveys, simulator developments, simulations, measurements, analysis, drawings and discussions in this Master's Thesis are done by the author. The ISSI concepts in Chapter 3 were created by the other members of the ISSI project team, but the discussions and comparisons have been carried out by the author.

Chapter 2

Previous Work

In this chapter, the underlying theories of remote sensing and hyperspectral imaging are reviewed and previously built related instruments and spectrograph techniques are discussed. Finally, applicable spatial light modulation techniques are reviewed.

2.1 Principles of Spectral Imaging in Remote Sensing

Remote sensing is essentially imaging the surface of the Earth at various parts of the electromagnetic spectrum. The spectrum of electromagnetic radiation between gamma-rays and radio waves is shown in Figure 2.1.

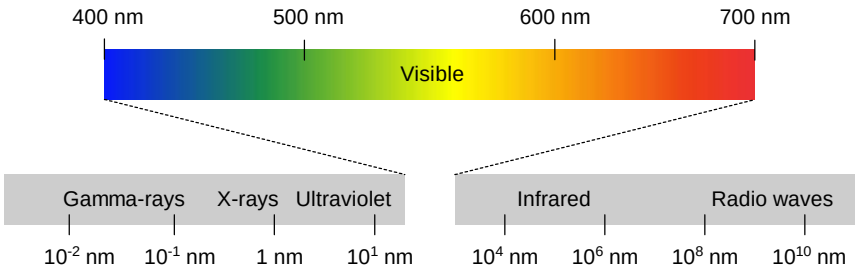

Figure 2.1. Electromagnetic spectrum between gamma-rays and radio waves. Visible light is a narrow band between ultraviolet and infrared.

There are active and passive remote sensing instruments. Active instruments observe the signal that they have transmitted, for example, laser pulses or microwaves. Passive instruments receive directly and indirectly the radiation of the Sun. The five main radiation components received by a passive remote sensing instrument are shown in Figure 2.2. Radiation emitted by the ground and atmosphere are only significant at wavelengths longer than 4 μm [1]. The dominating component at visible wavelengths

is the radiation of the Sun reflected by the ground and atmosphere when the direct radiation from the Sun is omitted [5]. There is also multiple scattered radiation but these components are mostly insignificant.

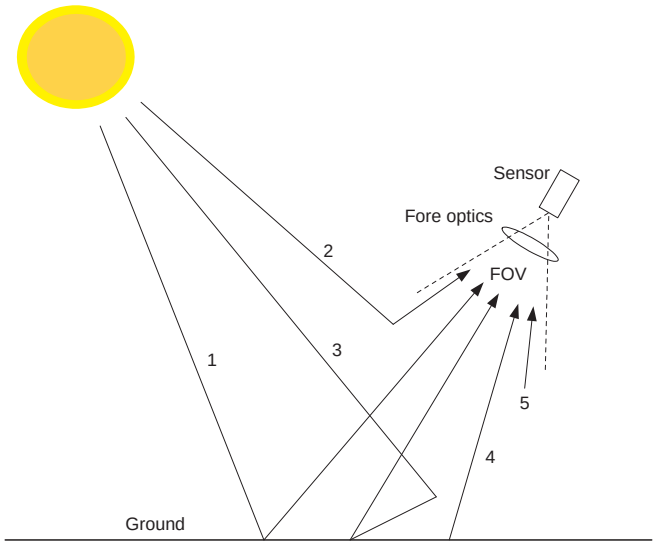

Figure 2.2. Signal scattering paths in atmosphere. Sensor receives all radiation components from it's field-of-view (FOV) . The components are 1) ground reflected radiation, 2) radiation reflected from atmosphere, 3) radiation reflected through the atmosphere or ground target and ground, 4) ground emitted radiation and 5) atmosphere emitted radiation.

The radiant energy of electromagnetic radiation is defined as [1]

$$Q = \frac{hc}{\lambda} \tag{2.1}$$

where $h = 6.6262 \ \cdot 10^{-34}$ Js is Planck's constant, c is the speed of light and λ is wavelength. The radiant energy is therefore inversely proportional to wavelength. Spectral radiant flux [1]

$$\Phi_\lambda = \frac{\partial^2 Q}{\partial t \cdot \partial \lambda}, \tag{2.2}$$

where t is time, is the rate at which radiant energy is transferred from a point or a surface to another surface per unit wavelength interval. Spectral radiant flux density at a surface [1]

$$M_\lambda = E_\lambda = \frac{\partial \Phi_\lambda}{\partial A}, \tag{2.3}$$

where A is an area of a surface, is the radiant flux divided by the area of the surface. The spectral radiant flux density emitted from a surface is referred to as spectral radiant

exitance M_λ and the density incident on a surface is called spectral irradiance E_λ. Spectral radiant intensity [1]

$$I_\lambda = \frac{\partial \Phi_\lambda}{\partial \Omega}, \tag{2.4}$$

where Ω is a solid angle, is the spectral radiant flux proceeding from the source per unit of solid angle. Spectral radiance [1]

$$L_\lambda = \frac{\partial^2 \Phi_\lambda}{\partial \Omega \cdot \partial A \cdot \cos \psi} \tag{2.5}$$

where ψ is the angle between the normal of the element and the observation direction, is the spectral radiant flux leaving an element of the surface surrounding the point divided by the solid angle of the cone and the area of the orthogonal projection of the element.

Figure 2.3 shows top-of-atmosphere and sea level irradiances after the atmosphere attenuation. The atmosphere attenuates the radiation from the Sun through scattering and absorption. In the wavelength range 0.3 μm to 2.6 μm attenuation is mainly caused by the absorption of ozone (O_3), water vapour (H_2O), oxygen (O_2) and carbon dioxide (CO_2) molecules [6]. Attenuation is also caused by the absorption and scattering due to aerosols, optical turbulence, reflection and refraction [7]. Figure 2.4 contains MODTRAN4 [8] simulated atmosphere transmission in the wavelengths from 0.3 μm to 2.6 μm.

Spectral exitance according to Planck's law of black body radiation is [6]

$$M_\lambda = \frac{2hc^2}{\lambda^5} \left(\exp\left(\frac{hc}{k_B T_B \lambda} \right) - 1 \right)^{-1} \tag{2.6}$$

where T_B is the temperature of the black body and $k_B = 1.3805 \cdot 10^{-23}$ Ws/K is Boltzmann's constant. Spectral irradiance of black body at $T_B = 5900$ K is shown in Figure 2.3 computed from Equation 2.6, which approximates the radiation of the Sun at the top-of-atmosphere.

2.2 Hyperspectral Remote Sensing Instruments

One way to classify spectral remote sensing instruments is to compare the number of wavelength bands that the instrument is capable of discriminating. An instrument is referred to as being multispectral if there are more than two wavelength bands and hyperspectral if there are more than a hundred bands.

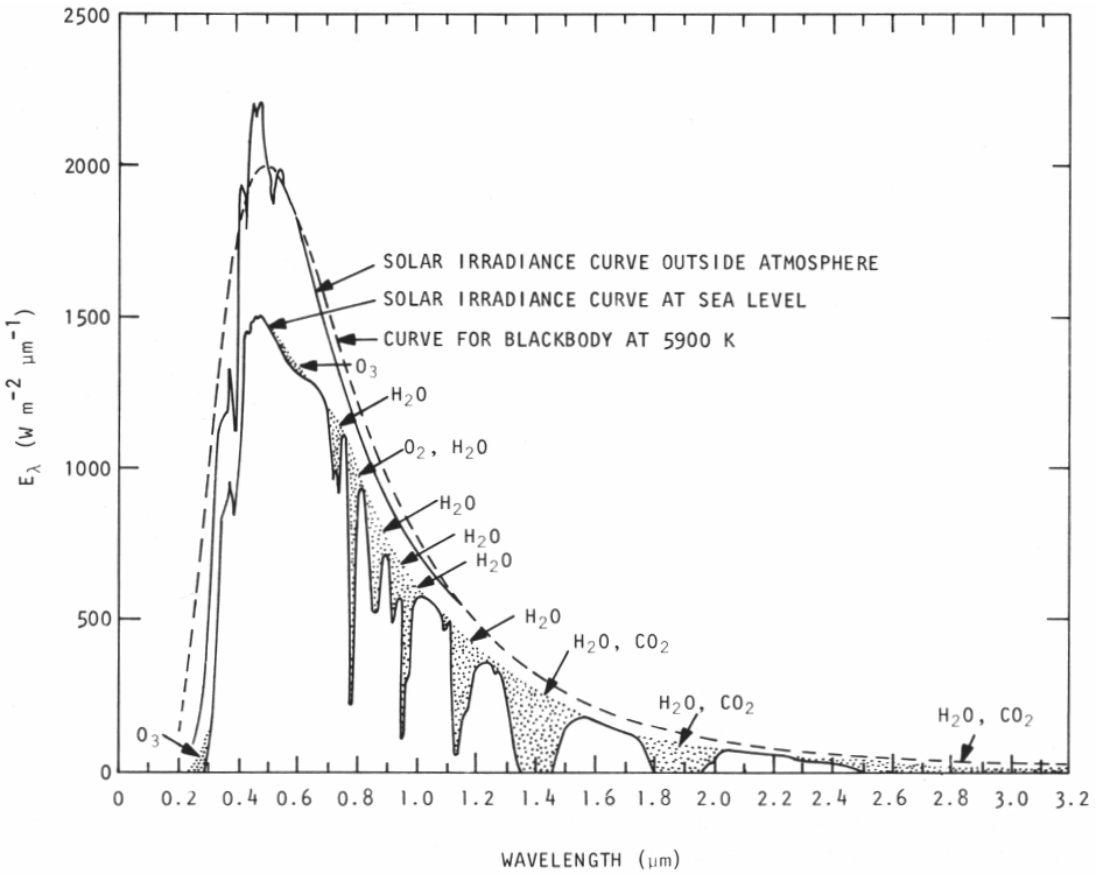

Figure 2.3. Top-of-atmosphere and sea level radiation [1]. Exitance for black body at $T_B = 5900$ K approximates the radiation of the Sun.

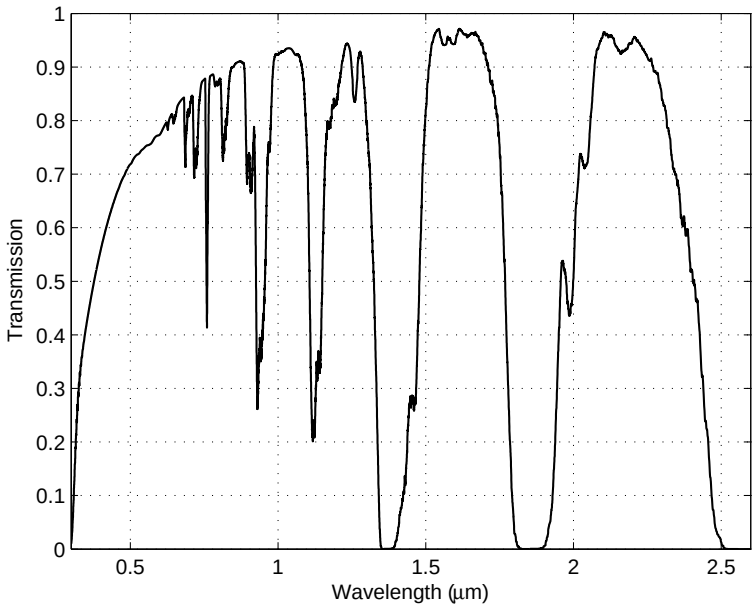

Figure 2.4. Simulated transmission through atmosphere using MODTRAN4. Molecule absorptions can be clearly seen.

The concept of imaging spectroscopy is shown in Figure 2.5. The instrument samples simultaneously multiple spectral wavelength bands over a large area in a scene, typically ground. The across-track dimension, swath width, is acquired simultaneously but the other direction, along-track, is built up by the relative motion of the instrument. After the data processing, the data for each ground pixel contains the spectral signature of the target because each ground type has reflectance distinguishable from other types.

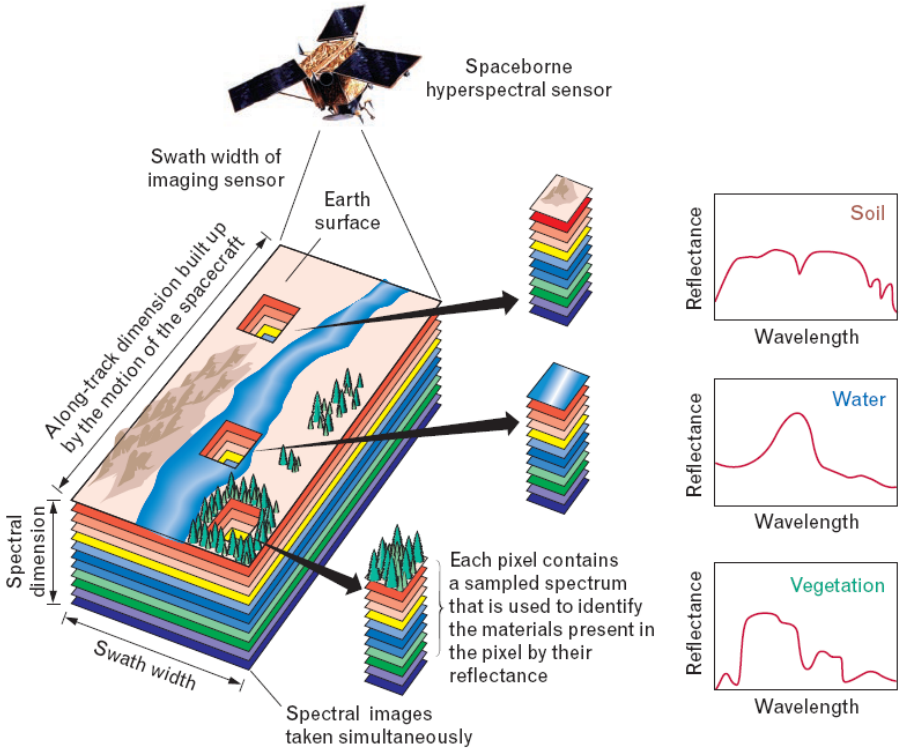

Figure 2.5. Concept of imaging spectroscopy [9].

A conventional imaging spectrometer consists of the fore optics, dispersing component and imaging sensor, as shown in Figure 1.1(b). The function of the dispersing element is to spread the spectrum of the input light spatially to the different locations on a 1D or 2D detector. In the case of a 1D detector, only the spectrum of a single ground pixel can be detected at a time. Therefore, a scanning mirror is needed to create an image. This kind of design is shown in Figure 2.6(a) and is known as a whiskbroom scanner. In a pushbroom design, in Figure 2.6(b), a 2D detector is used and therefore a line of ground pixels can be detected simultaneously. In both of these designs, only one spatial axis can be imaged at one position, the other spatial axis takes a form as a consequence of moving instrument.

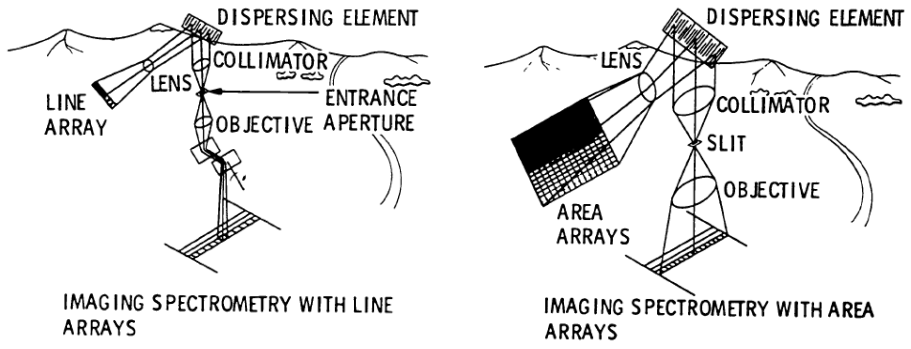

(a) (b)

Figure 2.6. Different imaging spectrometer constructions [3]. (a) Whiskbroom and (b) pushbroom.

Figure 2.7 shows data acquisition modes characteristic of several conventional spectrometer types defined by Descour and Dereniak in 1995 [10]. There are three dimensions in the acquired data of spectral instruments, two spatial, x and y, and one spectral, λ. A whiskbroom spectrometer (a) samples multiple wavelengths only from a single target location at a time. A framing camera (b) samples a 2D area of a target by the narrow wavelength band ($\Delta\lambda$). And a pushbroom spectrometer (c) samples a line of a target by the multiple wavelengths.

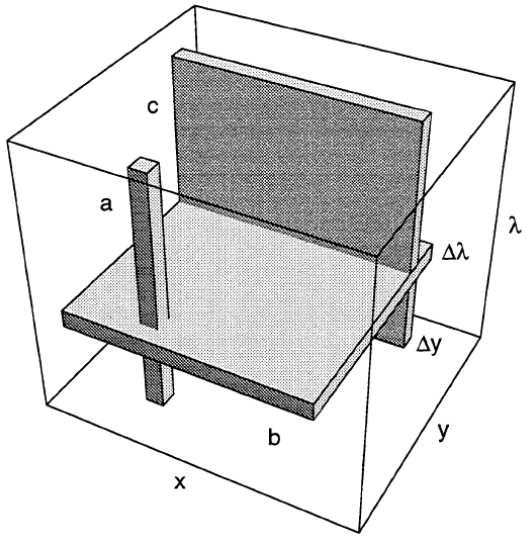

Figure 2.7. Data cube and data acquisition modes characteristic of several conventional spectrometer types [10]. (a) Whiskbroom, (b) framing camera and (c) pushbroom.

The first remarkable imaging spectrometer was the Airborne Visible/Infrared Imaging Spectrometer (AVIRIS) developed at the Jet Propulsion Laboratory [11]. The initial scientific objectives were the investigation of the vegetation between red and near-infrared (NIR) and mineral absorption in the spectral region of 2.2 μm. The development of this whiskbroom type scanner began in 1983 and the first measurements were carried out four years later, in 1987. The AVIRIS was the first imaging spectrometer to measure the reflected radiation of the Sun from the ground between 400 nm and 2500 nm at intervals of 10 nm. The great advantage of a whiskbroom scanner is that the light for every ground element passes through the same path of the optical system.

After the AVIRIS, a number of airborne and spaceborne imaging spectrometers have been built for both experimental and operational purposes. Some instruments are dedicated for the ultraviolet (UV) wavelengths (< 0.4 μm) and others for the visible and NIR ($0.4 - 1.4$ μm) or for the longer infrared (IR) wavelengths (> 1.4 μm).

2.3 Applications for Hyperspectral Imaging

The main application areas for hyperspectral imaging instruments are the recognition and classification of natural resources, water monitoring and recognition of man-made targets, traffic and urbanisation monitoring.

The first application of hyperspectral imaging was material identification. Individual materials were identified based upon their reflectance characteristics. Later airborne imagers were used for vegetation analysis to understand the contribution of land to the global carbon cycle [3].

The identification of dissolved constituents and water quality in lakes and other water bodies and near-shore environment are the major objectives of some instruments [12]. Remote sensing of oil spills by satellite may provide the capability to monitor oil on the sea around the clock [7].

Gomez has made a review of hyperspectral applications that are related to transportation and traffic [7]. Hyperspectral imaging has been used for car recognition based on the library of vehicle paint signatures, which enhances the monitoring of traffic flows. Remote sensing can also be very effective in the monitoring of the extent of urbanisation and infrastructure. Many applications still need a spectral signature database. The goal of the spectral database research is to automate the image processing of hyperspectral data for potential real-time material identification and mapping. The ability to perform an automated pattern recognition, extract information from the hyperspectral data and distribute the results to users in a timely manner is crucial for commercial operations.

To summarise, one of the major challenges of hyperspectral imaging is data handling and processing. The other challenge is to select the appropriate wavelength bands for the analysing algorithm. One of the objectives of the present ISSI study is to assess the feasibility of on-board data handling for facing the first above-mentioned challenge.

2.4 Techniques Used for Previously Built Spectrographs

In this section relevant spectrograph techniques are discussed. The main focus is to review the techniques in light of the ISSI requirements [13]. Imaging grating, prism-grating-prism component, liquid crystal tunable filter, acousto-optic tunable filter and interferometer based spectrographs are considered.

2.4.1 Aberration-Corrected Holographic Imaging Gratings

Saari has reviewed methods to manufacture an aberration-corrected holographic concave grating (see Figure 2.8(a)) for imaging spectrograph in 1995 [14]. The grating structure is created by two coherent laser beams on the substrate. Aberrations of the grating can be optimised by altering the recording geometry and the shape of the grating curvature. Gratings were simulated, manufactured and finally characterised. This kind of method has been used for the spectrometer of the GOMOS instrument on ESA's Envisat satellite. The reasons for selecting a concave grating were its simplicity and high spectral efficiency over the total spectral range compared to a traditional imaging disperser consisting of a collimating telescope, plane grating and an imaging telescope. The traditional disperser based spectrographs are better for large FOV applications. The aberrations of a concave grating increase rapidly as a function of angle of incident light. Thus, concave gratings are feasible, for example, for star occultation instruments where the FOVs are narrow.

A typical Offner spectrograph (see Figure 2.8(b)) consists of two concave mirrors and a convex reflective grating. Mouroulis *et al.* have characterised Offner spectrographs according to efficiency and polarisation sensitivity [16]. The main finding was a 35% difference between the ordinary and extraordinary polarisation states at the wavelength of 450 nm but the difference was considerably less ($< 10\%$) at longer wavelengths.

2.4.2 Prism-Grating-Prism Spectrographs

The Prism-Grating-Prism (PGP) component was invented by Aikio in 1991 [17]. The PGP is a direct vision optical component, which consists of two prisms and a transmissive grating mounted between these two prisms. The PGP concept is shown in

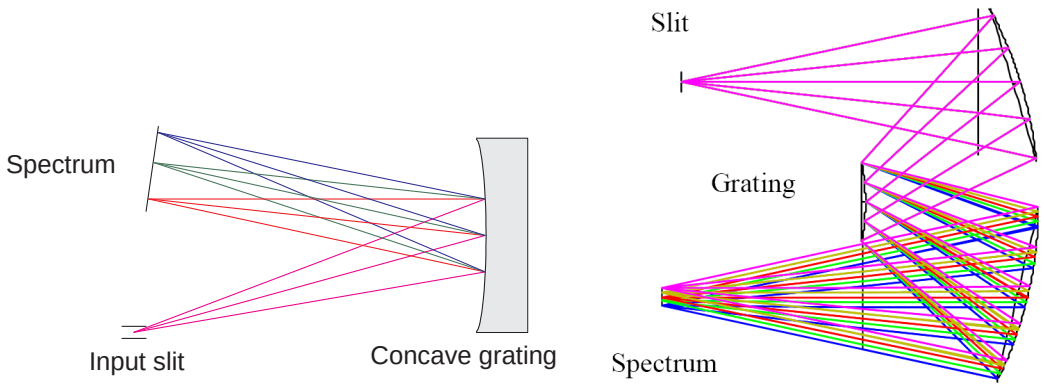

(a) Concave grating. (b) Offner grating [15].

Figure 2.8. Concave and Offner gratings.

Figure 2.9. The objective focuses the image of the target on the entrance slit, the PGP element disperses the image of the slit and focuses it on the imaging sensor. As a consequence, the spectral content from many target locations can be observed simultaneously.

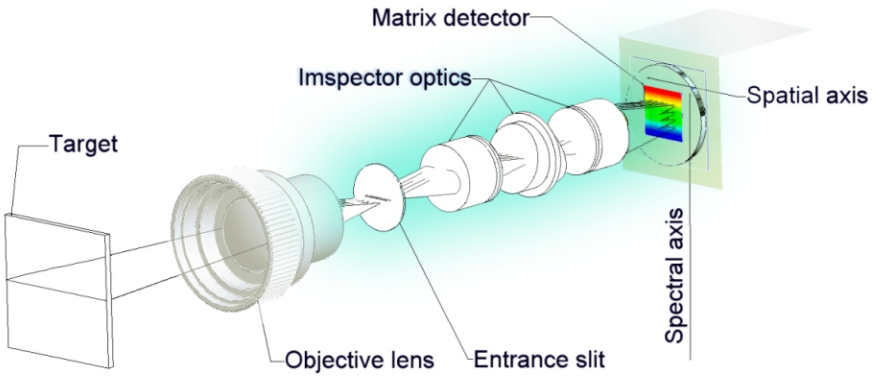

Figure 2.9. PGP concept [18].

The PGP component has many properties which make it attractive for the ISSI. The PGP provides large, linear dispersion due to its diffraction grating [17]. Also the PGP can be modified for different wavelength ranges quite freely by changing the vertex angles of the two prisms. In additional, the PGP has high diffraction efficiency and polarisation-independent throughput. The direct vision property permits a tubular mounting for a spectrometer.

ImSpector™ is a commercial product of Specim Ltd, Spectral Imaging Ltd, which design and manufacture many versions of this small imaging spectrograph [18]. One

of the widely known airborne spectral remote sensing instruments of Specim is the AISA [19,20]. Today the PGP component based spectrographs are used world-wide for industrial vision and spectral analysis, airborne remote sensing and scientific applications. The transmission of a typical ImSpector™, model V10E, is shown in Figure 2.10.

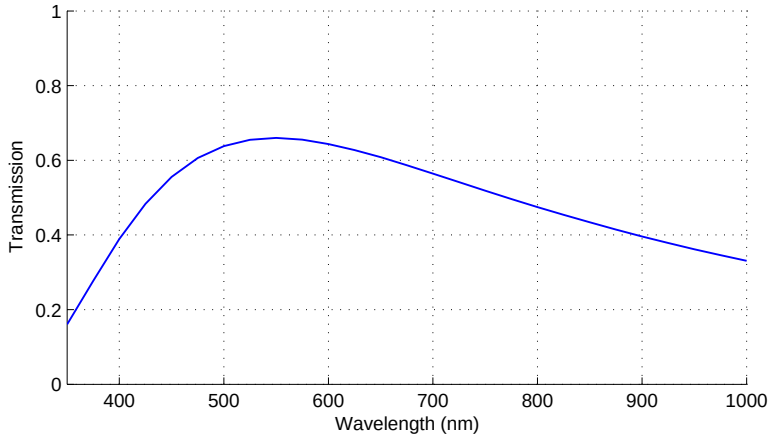

Figure 2.10. Transmission of typical ImSpector™, model V10E (Courtesy of Specim).

2.4.3 Liquid Crystal Tunable Filter Spectrographs

Tunable filters can also be used to separate the spectral information. In this section liquid crystal (LC) tunable filters are discussed mainly based on the articles written by Bland-Hawtworn *et al.* [21] and Masterson *et al.* [22]. In general, tunable filters have a narrow passband and tunable centre wavelength as shown in Figure 2.11.

The liquid crystal tunable filter (LCTF) is based on a Lyot filter, which is a stack of polarisers and tunable retardation liquid crystal plates. The basic element is shown in Figure 2.12(a). In a birefringent material, light is split into two rays, the ordinary and extraordinary, each experiencing a different refractive index, n_o and n_e, respectively, and thus having a different phase velocity. The difference of refractive indexes is called birefringence

$$\Delta n = n_e - n_o. \tag{2.7}$$

This leads to a time delay between ordinary and extraordinary rays,

$$\Delta t = \frac{\Delta n d}{c}, \tag{2.8}$$

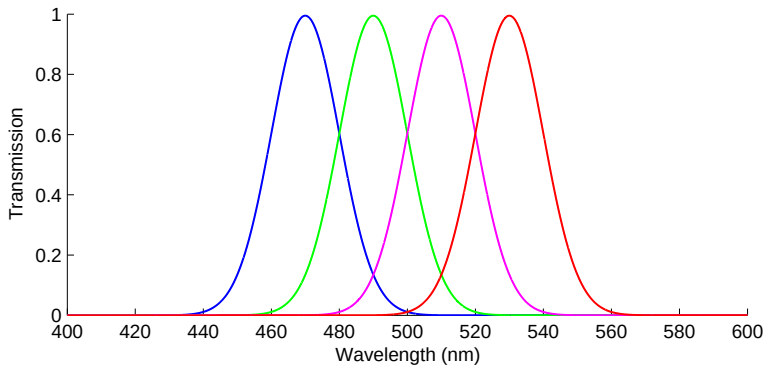

Figure 2.11. Transmission of tunable filter. The centre wavelength of a tunable filter can be adjusted either continuously or in discrete steps. Passband is generally quite narrow. The transmission of a fictional filter at four different centre wavelengths is shown.

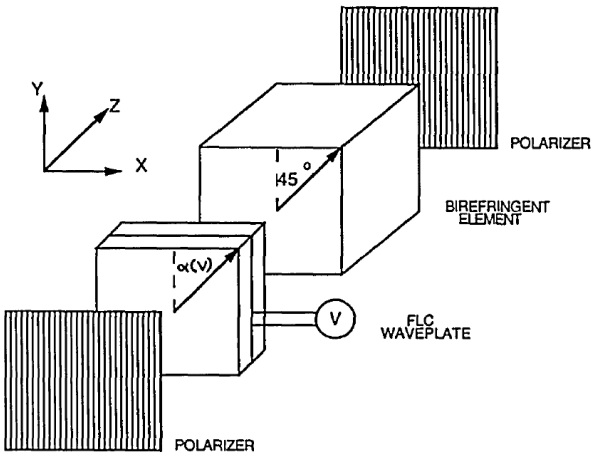

(a)

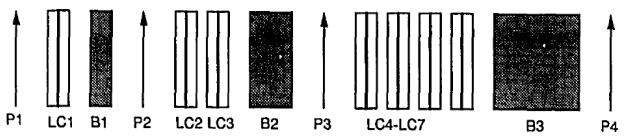

(b)

Figure 2.12. Structure of tunable Lyot filter [22]. (a) Single state and (b) filter stack. P1-P4 are polarisers. LC1-LC7 are LC elements and B1-B3 are birefringent materials.

where d is the thickness of the element. As a consequence, the polarisation state of the light is rotated, also know as retardance

$$r = 2\pi \frac{\Delta n d}{\lambda}. \tag{2.9}$$

In a basic element of the LCTF with surrounded polarisers, only wavelengths at which the optical path length equals an integer multiple of the wavelength are passed through the element. The transmission of two parallel polarisers as a function of retardance is

$$T = \cos^2\left(\frac{r}{2}\right). \tag{2.10}$$

Thus, the transmission of a single LCTF element is a periodic function

$$T = \cos^2\left(\frac{\pi \Delta n d}{\lambda}\right). \tag{2.11}$$

Transmission curves for three different thicknesses are shown in Figure 2.13(a). From Equation 2.11 it can be seen that transmission can be tuned by changing either birefringence Δn or thickness d. Usually the former is easier to implement.

Liquid crystal panels are birefringent components in which birefringence is controlled by varying an electric field. These are studied in more detail in Chapter 2.5.2. Quartz is one example of a birefringent material, retardance is changed by selecting a different thickness of the material.

The LCTF is a stack of these elements as shown in Figure 2.12(b). Lyot demonstrated that the thickness of the elements should be increased in powers of two, i.e.

$$d_i = d_1 2^{i-1}, \quad i = 1 \ldots q, \tag{2.12}$$

where d_1 is the thickness of the first element, d_i is the thickness of the i:th element and q is the number of elements in a stack. Transmission of an LCTF is the product of the transmissions of each element and thus the total transmission of a series of q elements is

$$T = \frac{1}{4^q} \frac{\sin^2(2^q \pi \Delta n d_1/\lambda)}{\sin^2(\pi \Delta n d_1/\lambda)}. \tag{2.13}$$

The total transmission of a stack of three stages is shown in Figure 2.13(b). The spectral period is determined by the thinnest element and the spectral resolution by the thickest element. Increasing the number of stacked elements increases the resolution but as a drawback the transmission efficiency is decreased due to the number of needed polarisers. This also increases the total thickness of the LCTF and thus increases

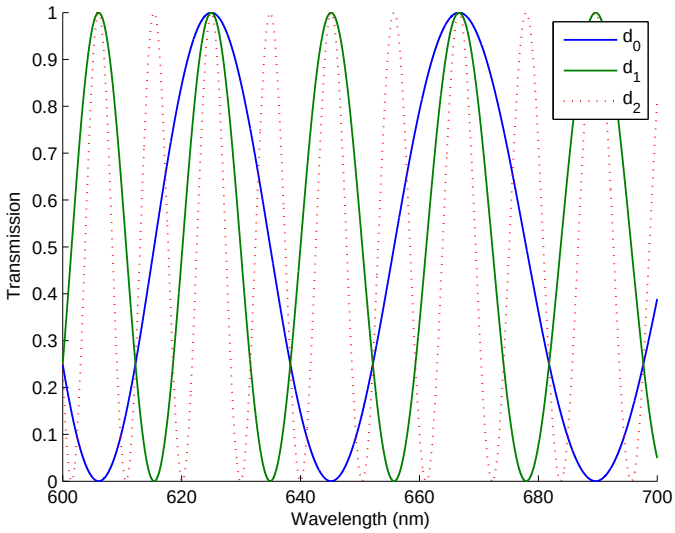

(a)

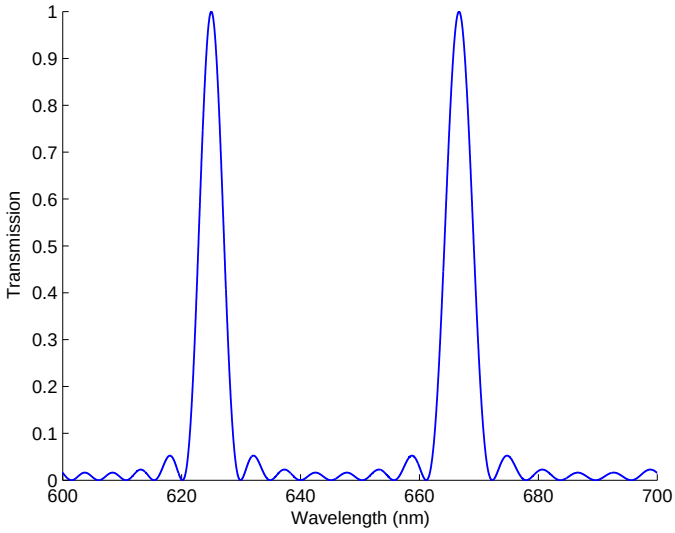

(b)

Figure 2.13. Transmission of tunable Lyot filter. (a) Transmission curves for the three different stages, and (b) transmission of the stack of three stages. $\Delta n = 0.01$, $d_1 = 1$ mm and $q = 3$.

distortion if used in an imaging instrument.

Boulder Nonlinear Systems manufactures commercially available liquid crystal based filters [23]. Table 2.1 presents some characteristics of a tunable Lyot filter demonstrated by Boulder Nonlinear Systems. Continuously tuned filters are best suited for low resolution applications. Higher resolution devices require so many stages that they are considered impractical because of high losses and increased device thickness.

Table 2.1. Characteristics of tunable Lyot filter [23]. Resolution is full-width at half-maximum (FWHM) at 600 nm and transmission efficiency is transmission for random polarised light. The FWHM defines the distance between points on the curve at which the value is half its maximum [24].

Number of stages	Resolution (nm)	Transmission efficiency	Device Thickness (mm)
1	209	32%	8
2	133	24%	16
3	63	18%	24
4	31	14%	32
5	16	10%	40
6	8	6%	48

An imaging Spectrometer using an LCTF was built and tested on a hot air balloon platform [25]. The prototype contains a six-stage LCTF with a spectral range between 430 nm and 680 nm. The transmission for unpolarised light was between 8% and 17%, depending on the wavelength. The bandwidth of the filter was between 30 nm and 50 nm, which changes almost linearly as a function of wavelength. Tuning can be done in 50 ms as random access between any two filter wavelengths. The field-of-view (FOV) was 6°. The main advantages of the LCTF are compact size, large aperture, large optical field-of-view, low wavefront distortion and low power consumption. The LCTF based framing camera was found to be feasible for use as an imaging spectrometer.

An airborne hyperspectral imaging system with an LCTF for biological and agricultural assessment was demonstrated [26]. The spectral range of the instrument ranged from 450 nm to 750 nm with the passband of 10 nm for each selected wavelength. The limited angle of acceptance of the LCTF was found to be ±7°, which caused some difficulties. Low transmission of the LTCF at the shorter wavelengths proved to be a problem. The transmission for unpolarised light was found to be about 6% and 14% at 450 nm and 490 nm, respectively.

An LCTF based spectroscopic imaging system for macroscopic samples was developed [27]. Poor transmission of the LCTF at the wavelengths of blue was very problematic. Despite that, relatively inexpensive spectroscopic imaging systems can be easily built and utilised using the LCTF.

2.4.4 Acousto-Optic Tunable Filter Spectrographs

An acousto-optic tunable filter (AOTF) is discussed based on the article written by Olson and Ninkow [28]. The AOTF is composed of birefringent crystalline material with a piezoelectric transducer attached to one side of the crystal and an acoustic absorber attached to the opposite side (Figure 2.14). When a radio frequency (RF) signal is applied to the transducer, it emits acoustic waves which propagate through the crystal. The waves cause the crystal lattice to be alternatively compressed and relaxed, leading to density changes and produces refractive index variations that act like a transmission diffraction grating (or Bragg diffracter) in a volume. Because the diffraction takes a place in a volume, the AOTF acts more like a filter, diffracting one specific wavelength of light, than a classical diffraction grating which is a surface or plane. It should be noted that the width of the passband varies as a function of wavelength. The transmitted intensity of light is proportional to the power of the RF signal.

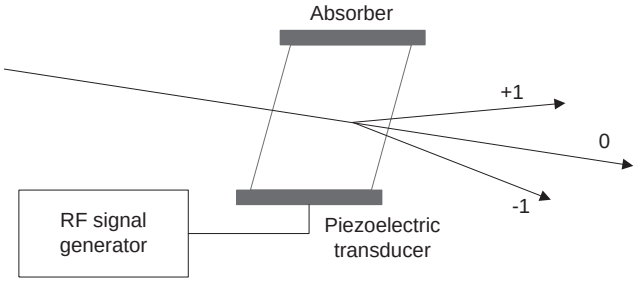

Figure 2.14. Operation of AOTF.

The diffracted light is directed into two orthogonally polarised first order beams (+1 and -1). The undiffracted zero order beam propagates the crystal without any spatial shifting. In typical applications this beam is blocked.

The main advantages of the AOTF are fast tuning speed and very narrow spectral resolution over a wide range of wavelengths. The disadvantages include the required RF generator, which needs several watts of power, limited choice in spectral resolution versus throughput trade-off and image distortions that vary with wavelength. The greatest limitation of the AOTF is the small optical aperture, which is limited to the

f-number of 8. The f-number defines the amount of energy collected by the optical system [29]. The smaller the f-number the higher the collected energy is.

Image blurring in an AOTF has been found to be a critical property. Wachman *et al.* demonstrated the usability of digital signal processing and deconvolution to reduce blur [30].

Chao *et al.* have demonstrated the AOTF based imaging spectrometer [31]. They found the angular aperture of the AOTF to be $\pm 5°$. When the FOV exceeds the angular aperture of the AOTF, the bandwidth will be increased causing blur to the output image. The AOTF demonstrated to be a feasible component for the imaging spectrometer.

2.4.5 Interferometer Spectrographs

An interferometer based spectrograph can be realised either with a Fourier or Fabry-Perot construction. In the next sections these are reviewed.

Fourier Transform Spectrographs

Fourier spectrographs can be realised with a Michelson-type interferometer construction, as shown in Figure 2.15 [5]. Incident radiation is partly reflected and partly transmitted by a beam splitter to two mirrors. Both mirrors reflect the radiation back to the beam splitter, where interference occurs. By moving one mirror, an interference signal, interferogram, is detected and the spectral content is given by the Fourier transform of this signal. This type of construction is suitable only for point sources.

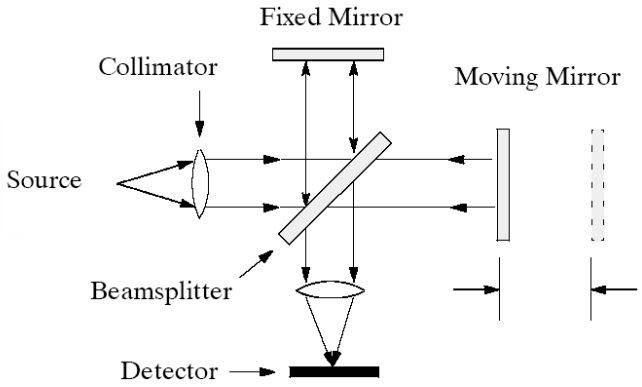

Figure 2.15. Michelson interferometer [5].

One example of this kind of spectrograph is the Fourier Transform Hyperspectral Imager FTHSI-MightySat II.1 [32], which is designed for terrain classification by the Air

Force Research Laboratory. The purpose of the instrument is to demonstrate the utility of the Fourier transform imaging spectrometer operating in space environment. The interferograms are produced by a monolithic Sagnac interferometer that is a variation of the Michelson interferometer. The instrument is operating in a pushbroom mode, swath width is 1024 pixels and the number of spectral samples is approximately 142 between the wavelengths of 475 nm and 1050 nm.

Fabry-Perot Spectrographs

Fabry-Perot interferometer consists of two face to face transmissive mirrors (see Figure 2.16) [33]. Incoming light traverses the first mirror, but will reflect between mirrors so that only wavelengths equal to twice the integer multiple of the distance between mirrors is capable of getting out, i.e.

$$\frac{\lambda}{2} = ND, \tag{2.14}$$

where D is the distance between mirrors and N is an integer.

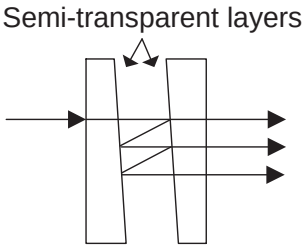

Figure 2.16. Fabry-Perot interferometer.

The transmission of the Fabry-Perot interferometer is [33]

$$T = \left(1 + \frac{4\rho^2 \sin^2 kD}{(1-\rho^2)^2}\right)^{-1}, \tag{2.15}$$

where $k = 2\pi/\lambda$ is the wavenumber and ρ is the reflectance of the mirrors. The transmission with some relevant values is shown in Figure 2.17.

The positions of the transmission peaks can be changed by tuning the distance of the mirrors. Therefore, it is possible to build an imaging spectrometer based on a framing camera. Electrically controlled Fabry-Perot imaging spectrometers have been used for a long time in astronomical telescopes.

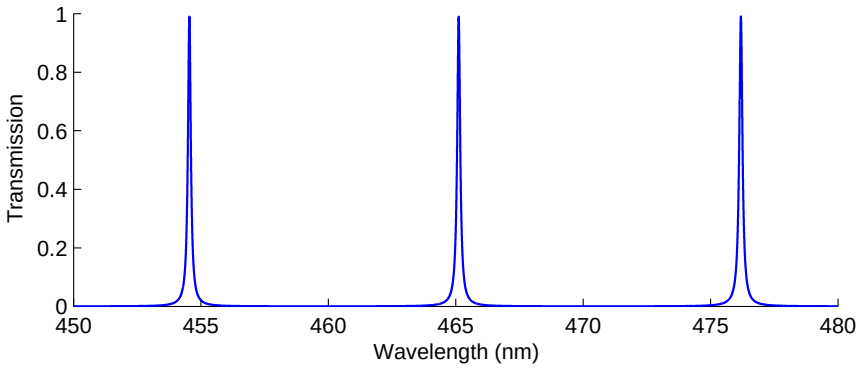

Figure 2.17. Transmission of Fabry-Perot interferometer. $D = 10\ \mu m$ and $\rho = 0.98$.

Gregg *et al.* have designed and built the ISO Long-Wavelength Spectrometer that employs a Fabry-Perot interferometer [34]. The distance of Fabry-Perot mirrors is tuned by changing the current of three coils that are mounted on one of the mirrors.

The other example is the Taurus Tunable Filter that is used as an interference filter in the TAURUS-2 telescope [35]. Large piezoelectric stacks are used to change the distance of the mirrors.

2.5 Spatial Light Modulators

A spatial light modulator (SLM) is a real-time reconfigurable device capable of modifying the amplitude, phase or polarisation of an optical wavefront as a function of position across the wavefront [36]. This ability of the SLMs to spatially and temporally modulate an optical wavefront in two dimensions opens many new possibilities for instrument design. The SLMs are capable of performing a number of useful operations on the optical signals. Some of the more important functions that have been demonstrated are analogue multiplication and addition, signal conversion, non-linear operations and short-term storage. Some applications for the SLMs are optical correlators, optical matrix processors and displays.

The ISSI employs the spatial amplitude light modulation in spectral and spatial domains, which is quite a special feature compared to the previously built imaging spectrometers. In this section, applicable light modulation techniques for the ISSI concept are discussed.

2.5.1 Micro-Mirror Array Spatial Light Modulators

Micro-mirror arrays (MMA) are manufactured on a silicon wafer using Micro-Electro-mechanical Systems (MEMS) technology [37]. These consist of an array of aluminium mirrors, one per pixel. The size of a mirror is typically $10 - 20$ μm. The mirrors are actuated individually by applying a voltage between a moving and an underlying electrode. Limiting factors of the tilting angle are air breakdown voltage and the mechanical stress of silicon [38].

Texas Instruments has been developing the MMAs since 1987 [39]. The layout of the mirrors is shown in Figure 2.18. A recent device, DMD 0.7 XGA 12° DDR DMD Discovery™, has 1024 x 768 pixels with a pitch of 13.68 μm and tilting angle of $\pm 12°$ [40]. It should be noted that mirrors have only two positions, $-12°$ and $12°$, thus $0°$ tilting angle cannot be used. Nowadays, these components are widely used in projectors. In these applications, variable modulation is created with pulse-width-modulation by tilting the mirrors.

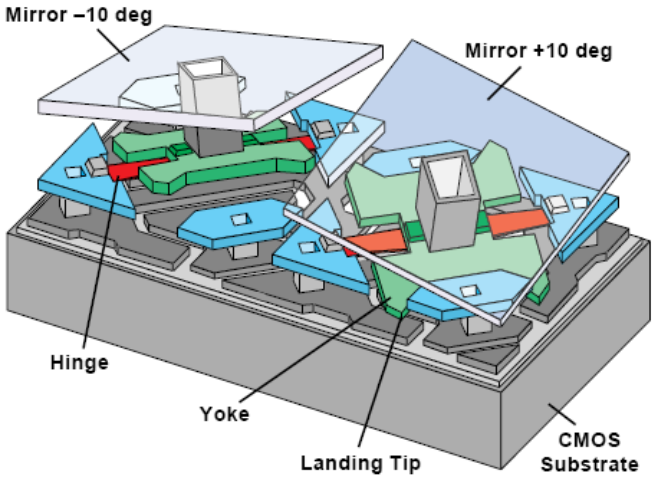

Figure 2.18. Layout of MMA pixel structure developed by Texas Instruments [39].

Fraunhofer Institut Photonische Mikrosysteme also manufactures MMA components mainly for lithography processes [41]. The size of a currently developed array is 2048 x 512 mirrors with pixel size of 16 μm x 16 μm. The tilting angle of the mirrors can be controlled continuously but is limited to $\sim 1.2°$.

Micro-mirror arrays have been used for multi-object spectrometers [42, 43] and image segmentation demonstrations [44].

2.5.2 Liquid Crystal Spatial Light Modulators

There are two types of liquid crystal (LC) based modulators, high-temperature polycrystalline silicon (HTPS) and liquid crystal on silicon (LCoS) [37].

The HTPS liquid crystal displays (LCD) are commonly used for laptops, monitor screens and projectors. A photograph of the Epson HTPS LCD, model L3P05S-46G10, is shown in Figure 2.19. The main operation principle of the HTPS LCD is shown in Figure 2.20.

The liquid crystal is a birefringent material; it has different refractive indexes for ordinary (n_o) and extraordinary (n_e) waves. Liquid crystals are situated between indium-tin-oxide (ITO) electrodes. When there is no voltage over the electrodes, the molecule structure acquires a spontaneous twist, i.e. a helix, about an axis normal to the layer. This causes the refractive indexes to rotate as a function of depth. Thus, the polarisation state of incoming light is rotated. After a voltage is switched on over the electrodes, the liquid crystal molecules turn parallel to the electric field. Thus refractive indexes are now constant, and the polarisation is not rotated. The liquid crystal layer is placed between two perpendicular polarisers. Therefore the transmission is maximum when the voltage is zero. Correspondingly, the transmission continuously decreases when the voltage is increased.

Driving transistors are needed for every pixel. As a consequence, the inter-pixel gaps are large which reduce the fill-factor. The fill-factor is the sensor area divided by the cell area, i.e. the area ratio between the actual pixels and total sensor [45].

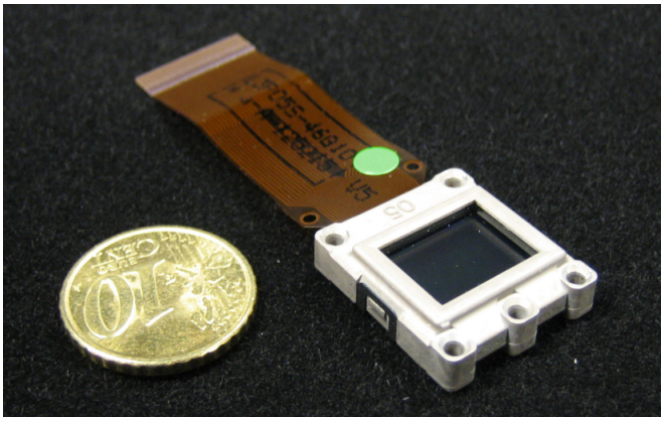

Figure 2.19. Photograph of Epson HTPS LCD, model L3P05S-46G10.

The rotation response time when a voltage is applied is

$$\tau_{on} = \frac{\gamma}{\epsilon_0 \Delta\epsilon E^2 - \pi^2 K_e / d^2}, \tag{2.16}$$

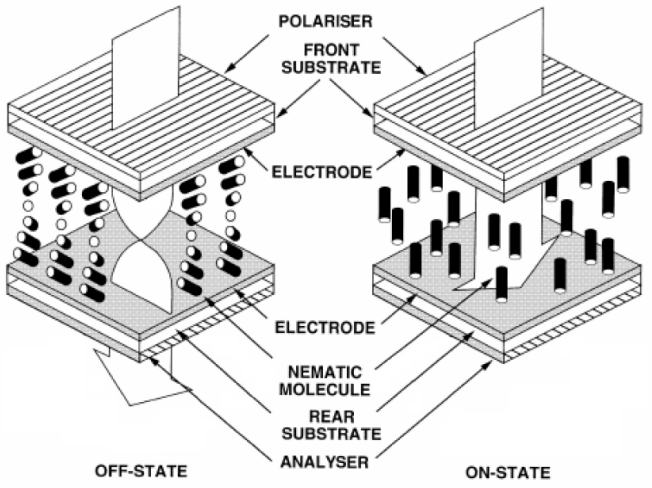

Figure 2.20. Operational principle of liquid crystal display (Adapted from [46]).

where γ is the rotation viscosity of the LC molecules, ϵ_0 is the dielectric constant in vacuum, $\Delta\epsilon$ is the anisotropic dielectric constant, E is the electric field strength, K_e is the effective elastic constant and d is the thickness of the LC layer. After the voltage is switched off, the rotation response time is

$$\tau_{off} = \frac{d^2\gamma}{K_e\pi^2}. \tag{2.17}$$

According to Equations 2.16 and 2.17, the turn-on time is controlled by the electric field strength as well as the rotation viscosity, but turn-off time is dominated by the thickness and the rotation viscosity. The thickness of the LC layer is typically around 10 μm.

The liquid crystal on silicon (LCoS) is a newer technology that has the advantages of both the LCD and MMA. It uses LC modulators on a passive mirror with a single polariser. Thus, the LCoSs are reflective components whereas HTPS LCDs are transmissive. Pixel brightness depends upon the polarisation state resulting from a double pass of the LC layer. A silicon back-plane allows integration of the pixel driving electronics on the same chip, thus increasing the fill-factor.

The optical and mechanical properties of Epson LCD, model L3P05S-46G10 [47], are listed in Table 2.2. The off-response time is much longer than the on-response time which was the assumption after Equations 2.16 and 2.17. The fill-factor is also quite low due to the transistors that are next to the pixels. The operational temperature is limited due to the clearing point and there is a parabolic relation between temperature and refractive indexes [48].

Table 2.2. Properties of Epson HTPS LCD, model L3P05S-46G10 [47].

Panel type	Transmissive HTPS LCD
Aperture size	11.3 mm x 8.5 mm
Pixel pitch	14.0 μm x 14.0 μm
Number of pixels	804 x 604
Fill-factor	48%
On-response time	7 ms
Off-response time	20 ms
Transmission	17%
Operation temperature	0°C-70°C

Another potential modulator is the LCoS device of LC-R 768 [49] from Holoeye. In Table 2.3 are listed some parameters for this device. The fill-factor is higher than that of the HTPS LCD due to transistors being placed below the pixels. The reflectance is higher than the transmission of the HTPS LCD. The pixel pitches and aperture sizes are similar.

Table 2.3. Properties of Holoeye LCoS, model LC-R 768 [49].

Panel type	Reflective LCoS
Aperture size	15.4 mm x 9.2 mm
Pixel pitch	12.0 μm x 12.0 μm
Number of pixels	1280 x 768
Fill-factor	92%
Reflectance	61% (blue), 64% (red)
Frame rate	60 Hz

2.5.3 Shutter Spatial Light Modulators

Micro-shutters can also be used for spatial light modulation. Micro-shutters have a number of micro-sized shutters with dimensions of some ten or hundred micrometres. Shutters are opened and closed, actuating the shutter 90°, using electrostatic-forces, thus operating in binary transmission mode. A shutter array with shutter size of 0.1 mm x 1 mm for astronomical infrared imaging was demonstrated by Takahashi *et al.* [50].

Also a two-dimensional shutter array with 128 x 128 and with shutter size of 100 μm x 100 μm was developed for the space telescope for the near-infrared region [51].

Pizzi *et al.* have developed a micro-optoelectromechanical (MOEMS) shutter array to function as a wavelength selective component for the spectrometer [52]. The size of the shutter array was 1 x 25 elements with shutter size of around 1 mm. The shutters were 1 μm thick metal pedals on the glass substrate. With no voltage applied between the electrodes, the pedals curl up away from the substrate because of the internal stresses built in the metal. When voltage is applied, the pedals roll down onto the substrate, thus closing the aperture of the pixel.

2.6 Summary

The relevant underlying functional principles of imaging spectral remote sensing were reviewed. Hyperspectral instruments, applications, spectrograph and spatial light modulation techniques were also discussed.

There are a number of techniques to realise an imaging spectrometer. Holographic imaging gratings are widely used in the narrow FOV applications. The PGP component is very useful and an elegant spectrograph. The LCTF could be used for some instruments but the device thickness and thus the transmission is poor if the resolution is a driving factor. The need for a separate high-power RF signal generator, image blurring and thermal control reduce the overall usefulness of the AOTF. Interferometer based spectrographs enable narrow transmission bands at the expense of the overall useful spectral range.

In the ISSI, the PGP component based ImSpector™ was found to be the right spectrograph thanks to the wide wavelength band, while still keeping high spectral resolution, polarisation-independent throughput, compact size and compliance for an imaging instrument.

Chapter 3

Proposed Novel Instrument Concepts

In this chapter, three possible concepts for the ISSI breadboard are introduced. The concepts are designed based on the requirements given by ESA. Some of these requirements are listed in Table 3.1. The components of the ISSI breadboard are characterised in Chapter 4 and the concepts are simulated and compared in Chapter 5.

Table 3.1. Some requirements for ISSI given by ESA [13].

Description	Value
F-number	4
MTF at Nyquist frequency	> 0.2
Flying altitude	2 km to 5 km
Ground pixel size	0.5 m @ 2 km, 1.25 m @ 5 km
Wavelength range	450 nm to 900 nm
Spectral resolution (FWHM)	< 7 nm

3.1 Two ImSpectors™ with Transmissive LCD

The first instrument concept is shown in Figure 3.1 and the 3D-model of the corresponding breadboard is shown in Figure 3.2. The objective focuses the image of the target (i.e. ground) on the input slit of the first ImSpector™. The image of the slit is dispersed and focused on the LCD. The image projected on the LCD is linearly polarised due to the first polariser. The LCD modulates each pixel independently by

rotating the polarisation state. The second polariser defines the intensity of each pixel. The modulated image is de-dispersed using the second ImSpector™ that focuses the image on the linear array sensor.

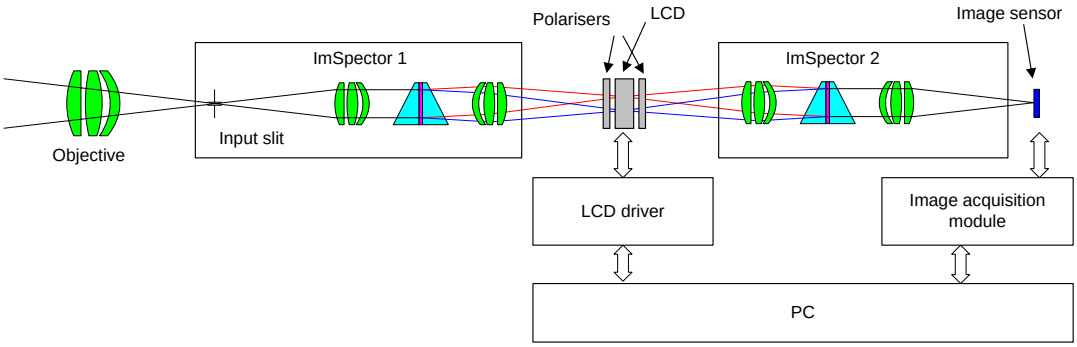

Figure 3.1. Instrument concept of two ImSpectors™ with transmissive LCD.

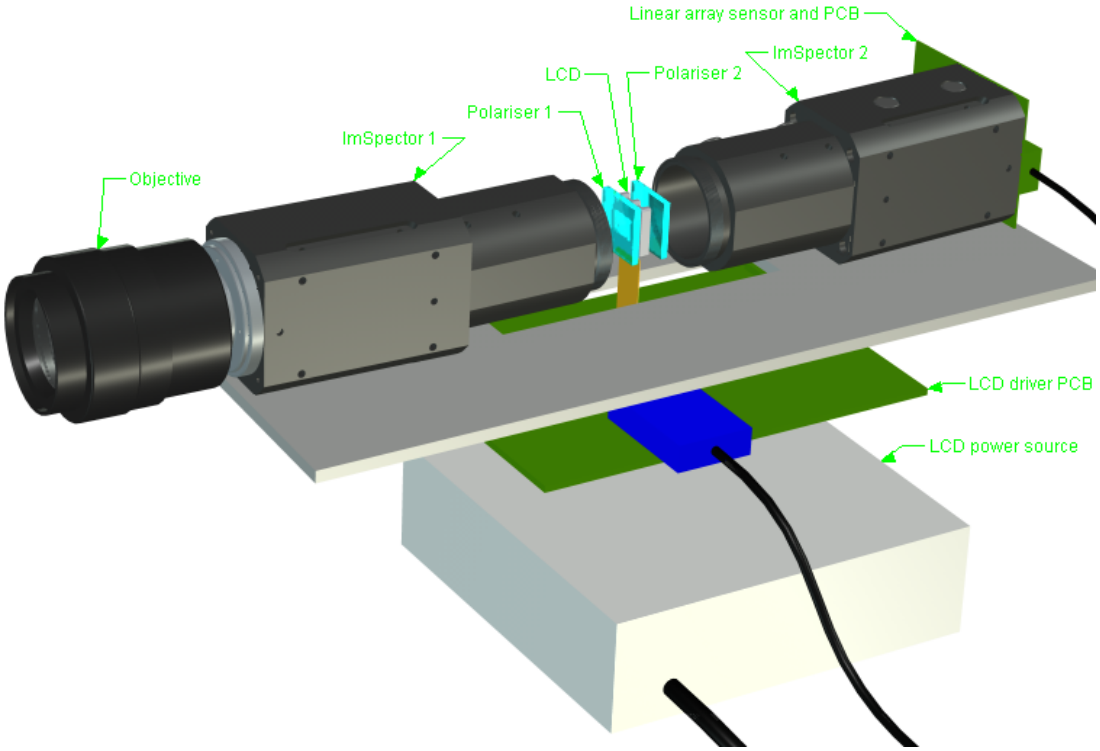

Figure 3.2. 3D model of instrument breadboard (3D model of ImSpector™ used courtesy of Specim).

It should be noted that this optical design is symmetric relating to the LCD, i.e. there is the same image geometry on both input slit and image sensor, the only difference is

that the image is modulated in spatial and spectral domains.

Both the LCD and image sensor are controlled through the driver cards and computer. The LCD driver generates correct voltage levels for each pixel. The image acquisition module sets integration and gain settings, reads the integrated image and sends it to the computer.

3.2 One ImSpector™ with Reflective SLM and Beam Splitter

The second instrument concept contains only one ImSpector™ with a reflective spatial light modulator. The concept is shown in Figure 3.3. The spatial light modulator could be based on a liquid crystal on silicon (LCoS) or a micro-mirror array (MMA). The LCoS is an LC derivative technique and it has a high reflectance in the perpendicular direction. The first part of the operation goes as in the previous concept. Light is dispersed on the SLM after the ImSpector™, selected spectral bands are reflected back to the ImSpector™ and after passing through the beam splitter focused on the image sensor. Non-selected spectral bands are absorbed or reflected, depending on the selected technique. This concept would be very compact in size compared to the previous one.

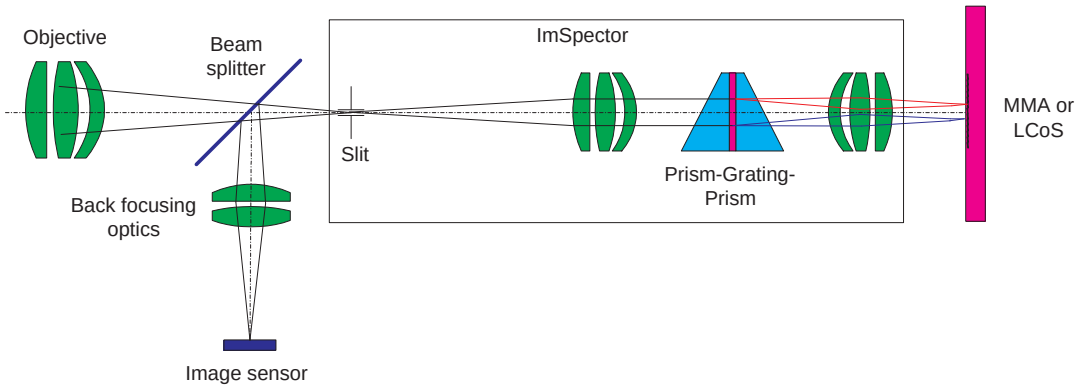

Figure 3.3. Instrument concept of one ImSpector™ with reflective SLM and beam splitter.

3.3 One ImSpector™ with Reflective SLM and Folding Mirror

The third instrument concept is shown in Figure 3.4. This concept is almost similar to the second concept presented. The only difference is a beam splitter which is replaced

with a folding mirror. The optical axis of the objective is slightly tilted with respect to the ImSpector™. The idea is to eliminate the signal attenuation in the beam splitter by using two different optical axes for light beams propagating in opposite directions thought the ImSpector™.

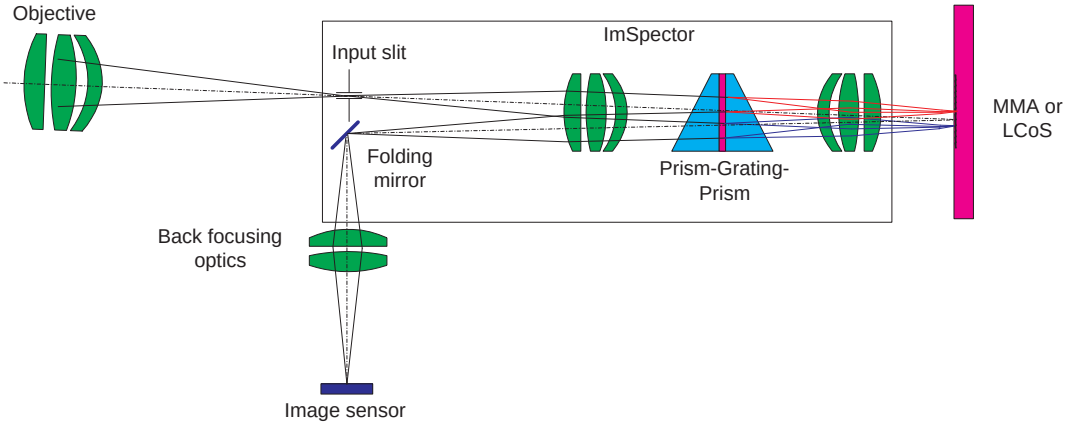

Figure 3.4. Instrument concept of one ImSpector™ with reflective SLM and folding mirror.

3.4 Discussion on the Presented Concepts

A geometrical analysis of the use of the micro-mirror array (MMA) is shown in Figure 3.5.

The f-number of the imaging system is defined by the marginal ray angle α that is capable of propagating through the system [29]:

$$f/\# = \frac{1}{2\sin\alpha}. \tag{3.1}$$

Using Equation 3.1, the marginal ray angle for the f-number of $f/\# = 4$ can be calculated as

$$\alpha = \sin^{-1}\left(\frac{1}{2 \cdot f/\#}\right) \approx 7.18°. \tag{3.2}$$

The minimum needed tilting angle should be analysed for the on-axis mirror ($s_1 = 0$) and thus it is

$$\beta = \frac{1}{2}\left(\tan^{-1}\left(\frac{D_{ap}/2 - s_1}{s_2}\right) + \alpha\right) \approx 18.5°. \tag{3.3}$$

Maximum achievable tilting angle when a Fraunhofer MMA is used is about 1.2° [41], which is about a tenth of the required. Therefore, it is not possible to use the MMA from Fraunhofer as shown in Figures 3.3 and 3.4. The MMA from Texas Instruments

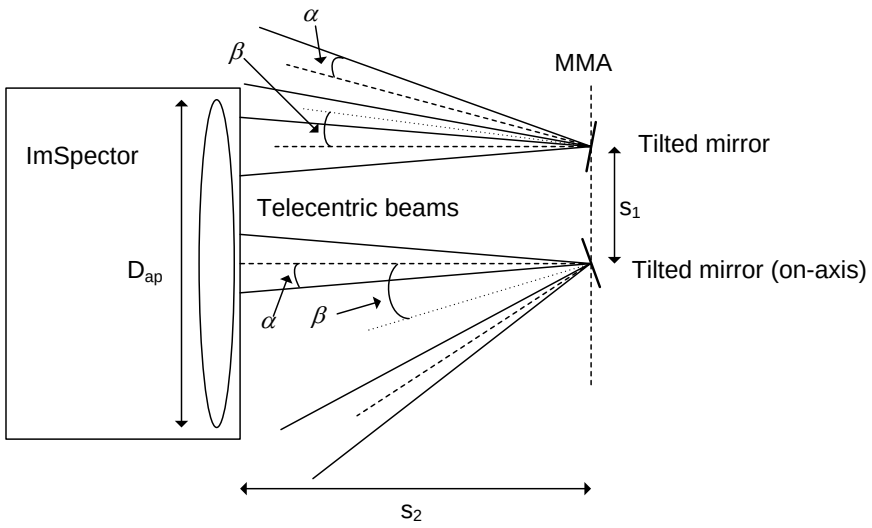

Figure 3.5. Geometrical analysis for tilting angle of micro-mirror array. D_{ap} is the aperture diameter of the ImSpector™, s_1 is the mirror distance from the optical axis, s_2 is the distance between the aperture and image plane, α is the marginal ray angle and β is the tilting angle of the mirror. Approx. values for the ImSpector™ were found to be $D_{ap} = 23$ mm and $s_2 = 20$ mm after a quick imaging test. According to [18] the output beams are telecentric, which means that the principal rays (shown dashed) are parallel to the optical axis [29].

(see Section 2.5.1 for details) is impossible to use due to the binary mode of the tilting angle of the mirrors which prevents the use of zero-tilting angle.

Reflective LCoS could be used for the concepts in Figures 3.3 and 3.4 due to the ability to reflect the signal back in its angle of incidence. Also, the possibility to use continuously variable modulation is an advantage compared to the MMAs.

The LC based spatial light modulators are best suited for the ISSI breadboard. The transmissive LCD from Epson, model L3P05S-46G10, is quite straightforward to utilise due to the availability of the projectors which include three of these kinds of LCDs. By disassembling the projector the LCDs can be easily used. Therefore, the LCD can be driven by the external monitor port of the computer. The only drawback is the low fill-factor and poor transmission as discovered in Section 4.2. The advantage is the transmissive structure which makes the optical and mechanical designs easier. Another possibility is to use the reflective LCoS from Holoeye, model LC-R 768. Possible advantages are high fill factor and high reflectance. The concept in Figure 3.4 that utilises the LCoS needs some modifications to the ImSpector™ to mount a folding mirror and back focusing optics. Such modification of the ImSpector™ is beyond the scope of this work.

Chapter 4

Characterisation of Components for ISSI

In this chapter, components used for the ISSI breadboard, polarisers, LCD and spectrograph, are characterised. Characterisation results are used for evaluating the feasibility of the components for the ISSI breadboard in light of the requirements shown in Table 3.1. The results are also used in the instrument performance simulator in Chapter 5.

4.1 Measurements of Polarisers

Polarisers are often the limiting components of instrument performance. The most vital parameters are contrast-ratio and transmission. Therefore, some kind of reference polarisers are needed for the selection process of suitable polarisers for the instrument. The quality of the Glan-Thompson polarisers is high, the contrast-ratio is also high, and the usable wavelength range is wide [53].

The transmission of Glan-Thompson polarisers was measured from 400 nm to 1000 nm. The measurement set-up is almost identical to that described in Appendix A.1, only the LCD is omitted. The light source was a continuous-arc xenon lamp and wavelengths were scanned using a motor controlled monochromator. A photo detector registered the changes in intensity at every wavelength with and without polarisers. The transmission measurement result of two parallel Glan-Thompson polarisers for linear polarised light is shown in Figure 4.1.

The result is consistent with the transmission data provided by the manufacturer [53]. It should also be noted that the theoretical transmission of two 50 mm thick glass cubes is approx. 85%, assuming transmission of 96% for each of four glass-air surfaces, which could be used as a theoretical maximum of the transmission.

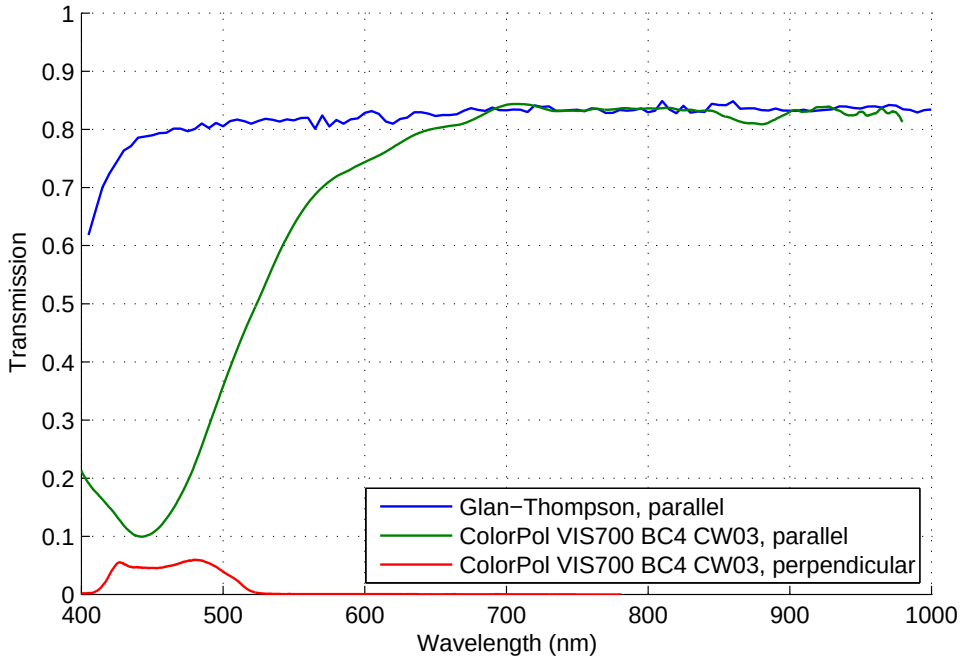

Figure 4.1. Measured transmission of polarisers. All transmission measurements are carried out with two polarisers and linear polarised light. Transmission for two perpendicular Glan-Thompson polarisers is zero.

An extensive manufacturer survey was carried out. As a result, ColorPol™ VIS 700 BC4 CW03 glass sheet polarisers from Codixx [54] were acquired and measured. Transmission measurement results for two polarisers are shown in Figure 4.1. The measured transmissions are consistent with the information provided by the manufacturer [54]. When compared to the Glan-Thompson polariser, the parallel transmission is slightly worse, but the thickness of these polarisers is only 1.6 mm [54] whereas the thickness for Glan-Thompson is 50 mm [53]. This has large impact on the optical design.

The transmission for perpendicular ColorPol™ polarisers is problematic. The transmission is too high at wavelengths shorter than 550 nm and thus an extra filter has to be used to reject the leakage signal.

4.2 Measurements of Epson HTPS LCD

4.2.1 Transmission Measurement

In this section, the transmission measurement of an Epson HTPS LCD, model L3P05S-46G10, is reported. The measurement set-up is shown in Appendix A.1. The f-number of the ISSI breadboard is proposed to be $f/\# = 4$ according the requirements shown in Table 3.1. Therefore, transmission of the LCD should be measured using the same value. The measurement set-up was first simulated with Zemax™ (see Figure 4.2) to find the correct lens positions to generate adequate incident ray angles on the LCD and to prevent stray light.

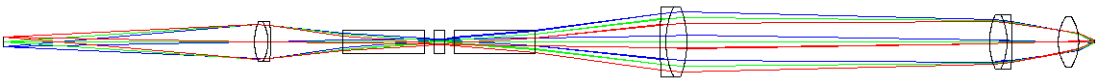

Figure 4.2. Simulated LCD transmission measurement set-up. From left to right there are the output slit of the monochromator (monochromator not shown), focusing lens, Glan-Thompson polariser, LCD, second Glan-Thompson polariser, three focusing lenses and finally the photo detector (only detector plane shown).

After the simulations, the laboratory set-up was built. The adjustment and measurement procedure can be divided into six steps:

1. All components were arranged according to the simulations. The focusing lenses were adjusted so that the spot size on the photo detector was sufficiently small.
2. The polarisers and LCD were removed and the reference measurement carried out by changing the wavelength of the monochromator and detecting the signal on the photo detector.

3. The first polariser and LCD were put back and the rotation angle of the polariser defined from the maximum signal of the photo detector when there were black pixels in the LCD.
4. The LCD was removed again and the reference measurement for the transmission of the first polariser measured.
5. The second polariser was put back, the rotation angle defined from the minimum signal of the photo detector and the transmission measured for the single polariser for linear polarised light .
6. The LCD was put back and the transmission measurement carried out.

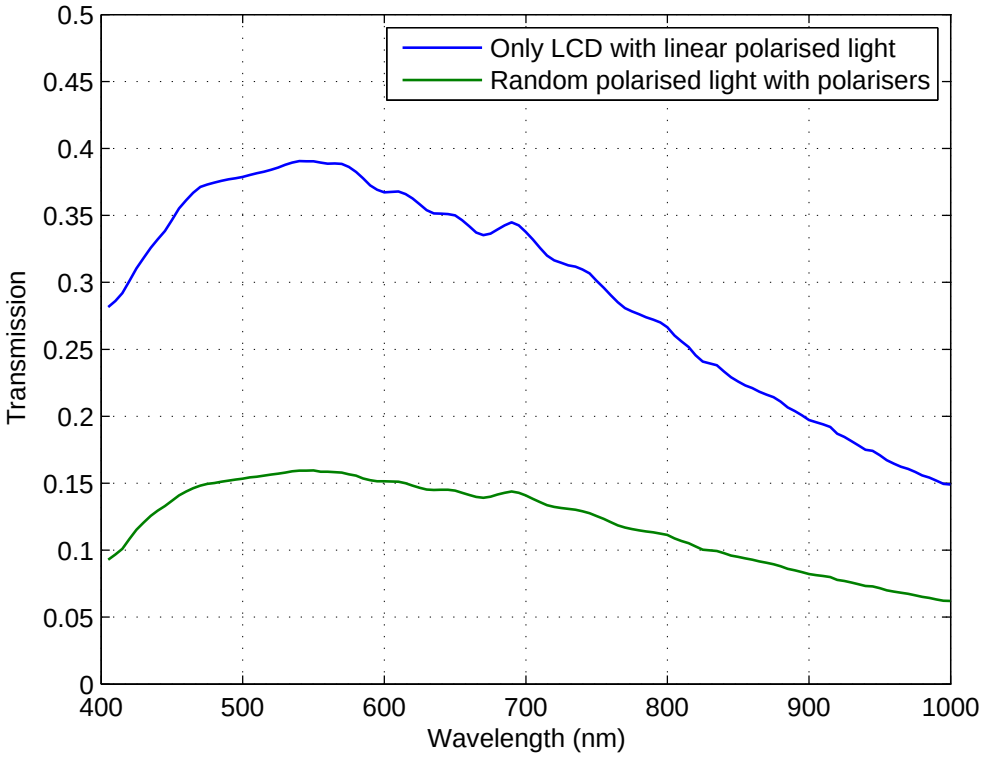

Figure 4.3. Measured transmission of Epson LCD, model L3P05S-46G10. Curves for the LCD with and without polarisers are shown. Curve with polarisers represents the true case, which includes transition from random to linear polarised light, two Glan-Thompson polarisers and the LCD. The effects of random polarised light and polarisers itself are eliminated from the other curve, which can be utilised with other polarisers.

The results of the LCD transmission measurement are shown in Figure 4.3, which shows that the transmission with polarisers is between 7% and 17%. This transmission is quite poor due to the fact that the LCD is the radiometric throughput limiting

component. The transmission of the ImSpector is between 20% and 70% according to Figure 2.10. The transmission of the LCD should be between 17% and 20% according to the manufacturer [47]. The polarisation or wavelength range are not specified in the manual but supposedly the transmission is averaged over the visible wavelengths and for random polarised light. The measured transmission is slightly lower but the difference is not significant.

4.2.2 Pixel Spatial Transmission Measurement

The block diagrams of the pixel spatial transmission measurement set-up are shown in Figure 4.4, and photographs of the set-up are shown in Appendix A.2. The main idea is to observe the LCD with a microscope camera when the LCD is illuminated with both collimated and diffuse light. Rays are parallel in collimated and randomly directed in diffuse light [55]. The incident angle of the collimated light was also changed to find the f-number.

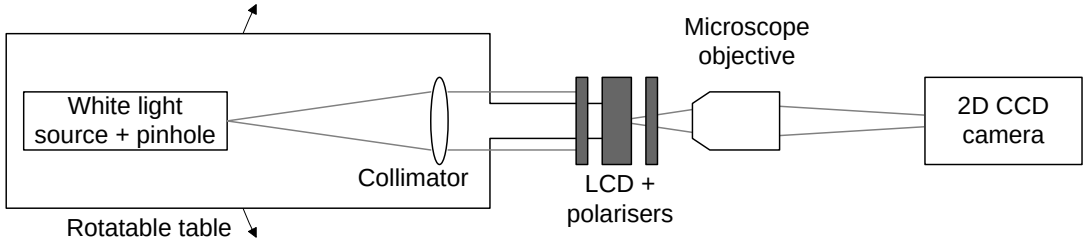

(a)

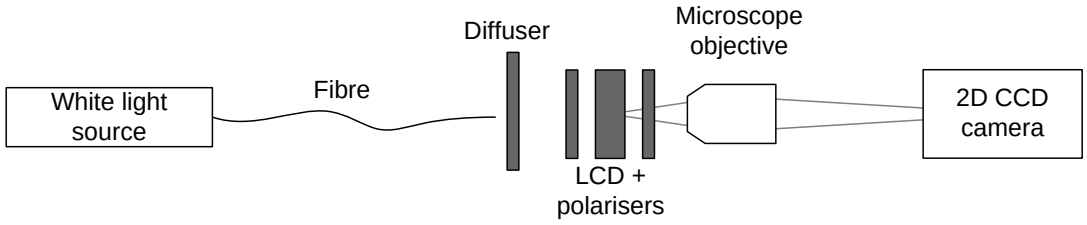

(b)

Figure 4.4. Block diagrams of LCD pixel spatial transmission measurement set-up for both collimated (a) and diffuse (b) light.

The pixel pitch of the image sensor was 4.65 μm and the magnification of the microscope objective was 6.3 [56]. The imaging resolution was verified by replacing the LCD with a USAF 1951 resolution target (see Figure 4.5). As a result, the resolution was found to be 0.86 ± 0.01 μm/pixel in both the row and column directions. This

resolution is adequate to analyse the pixel spatial transmission due to fact that the pixel pitch of the LCD should be 14 μm according to the datasheet [47].

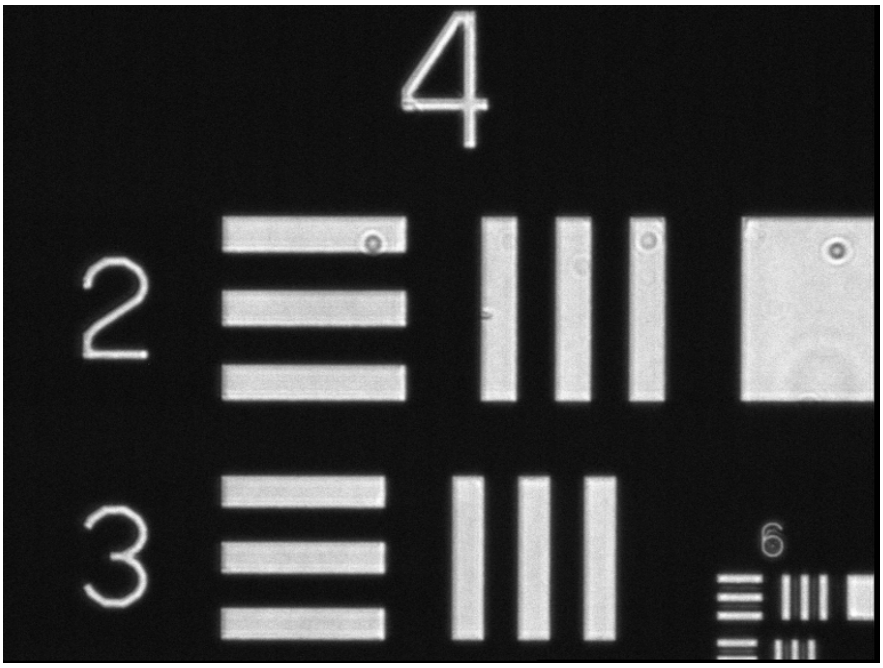

Figure 4.5. Sample image of USAF 1951 resolution target. The spatial frequency of the white lines in the top left corner is 17.9 lp/mm (group 4, element 2) thus the widths are 27.9 μm. Even smaller lines with spatial frequency 71.8 lp/mm thus widths 6.7 μm can be seen in the lower right corner for comparison. The spatial frequency defines the number of line pairs, black and white lines, per unit length [45]. The small circular artefacts are due to some dirt on the image sensor.

After that, the pixel pitch of the LCD was measured by observing the illuminated LCD. Sample pictures are shown in Figure 4.6 and pixel profiles for three adjacent pixels are shown in Figure 4.7. The pixel pitch was found to be $\Delta P_{SLM} = 14.0$ μm which is consistent with the information provided by the manufacturer [47].

The pixel spatial transmission was measured by turning a single pixel into white in the LCD and then illuminating it by the collimated and diffuse light. Pixel spatial transmission profiles for diffuse light and for different angles of collimated light are shown in Figure 4.8. The illumination angle was varied from $-6.9°$ to $5.0°$. The transmission profile of diffuse light is an envelope for the collimated light curves with different incident angles. This proves that measurements for the collimated and diffuse light match each other.

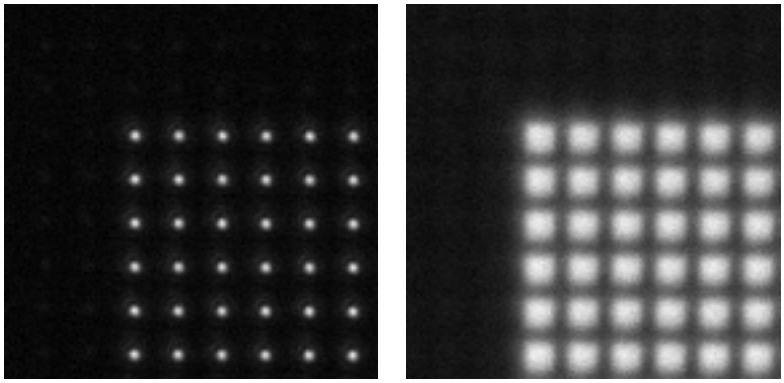

(a) (b)

Figure 4.6. Area of 6x6 pixels of corner of white square for both collimated (a) and diffuse (b) light. The incident angle of the light was perpendicular.

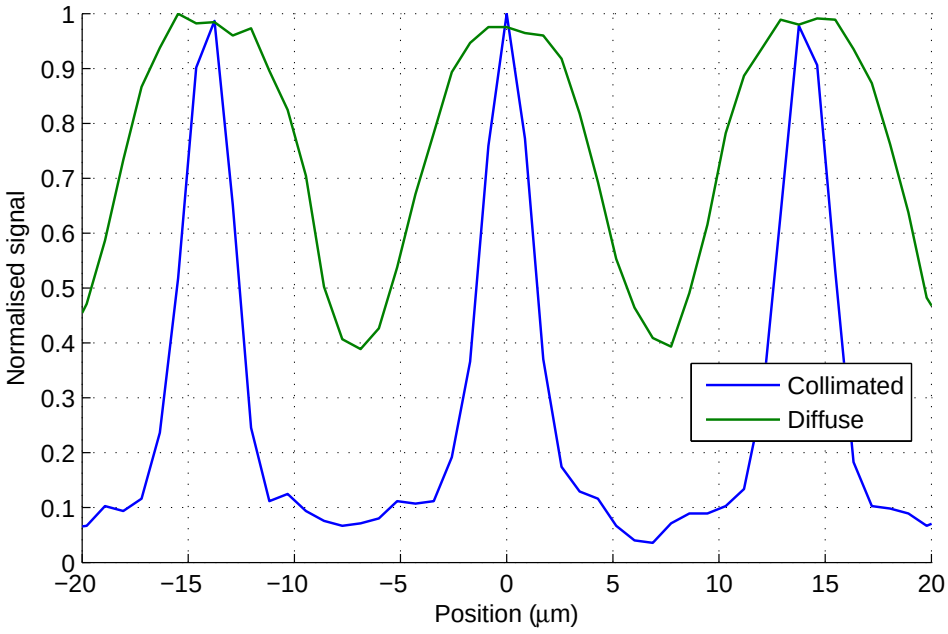

Figure 4.7. Pixel spatial transmission profiles of three adjacent pixels for both collimated and diffuse light. The incident angle of the light was perpendicular.

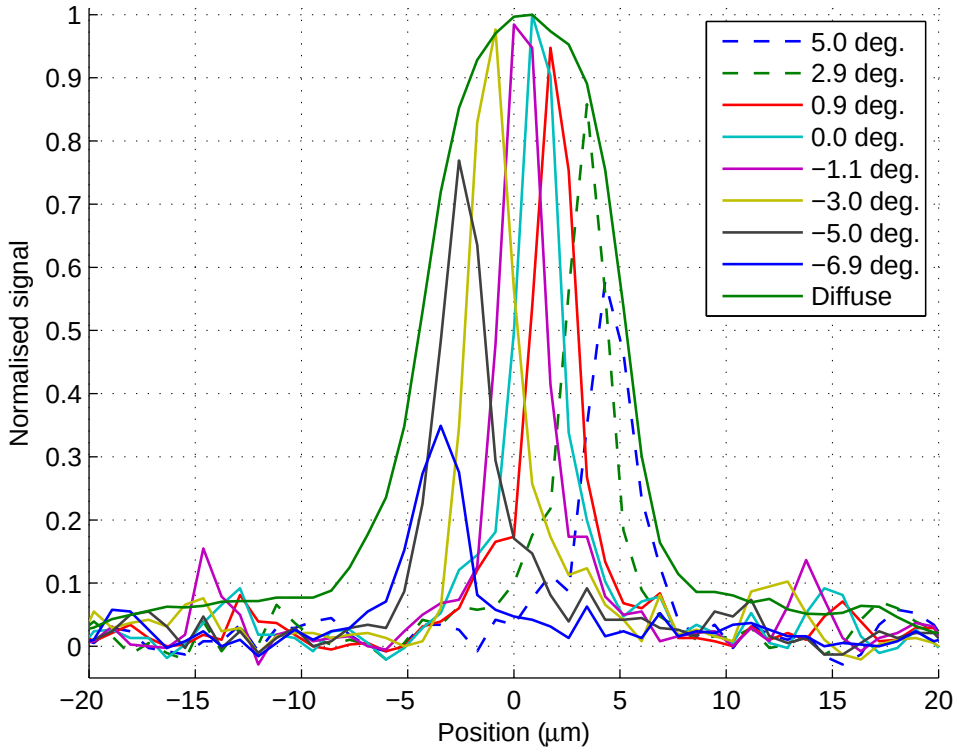

Figure 4.8. Epson LCD, model L3P05S-46G10, pixel transmission profiles for diffuse and collimated light for different incident angles. The incident angle of the diffuse light was perpendicular.

The f-number of the imaging system is defined by the marginal ray angle that is capable to propagate through the system [29]. In this measurement, the angle of collimated light can be used to estimate the f-number using Equation 3.1. According to Equation 3.1 and Figure 4.8, the normalised signal is 0.35 for the f-number of $f/\# = 4.16$. Correspondingly, the normalised signal is 0.57 for $f/\# = 5.7$. The f-number of the microscope objective is $f/\# = 2.5$ [56] thus the objective is not limiting. As a result, the minimum f-number for the LCD is approx. $f/\# = 4$. This result is adequate, because the f-number requirement given by ESA is $f/\# = 4$ according to Table 3.1.

Pixel profiles for both row and column directions for diffuse light were also analysed to find the symmetry of the pixel. The results are shown in Figure 4.9. As a result, the pixel aperture seems to be symmetric in the vertical and horizontal directions. The diameter of pixel aperture is the FWHM of the profiles, which is $D_{ap} = 10$ μm in both directions. The fill-factor for the rectangular aperture is [45]

$$F = \frac{D_{ap}^2}{\Delta P_{SLM}^2}. \tag{4.1}$$

where ΔP_{SLM} is the pixel pitch of the LCD. Correspondingly, the fill-factor for the circular aperture is

$$F = \frac{\pi(D_{ap}/2)^2}{\Delta P_{SLM}^2}, \tag{4.2}$$

According to Equations 4.1 and 4.2, the fill-factors for the rectangular and circular LCD pixels are 51.0% and 40.1%, respectively. According to Table 2.2, the fill-factor is 48%. Therefore, the aperture should be more square than circular. Looking at Figure 4.6(b), the pixel aperture can again be said to be more square than circular.

4.3 ImSpector™ Measurements

In this section, ImSpector™ characterisation measurements in terms of spatial and spectral resolution are reported.

The measurement set-up consists of the ImSpector™, an image sensor, an objective and the target. The target is a neon lamp with a replaceable slit or fibre. The 3D model of the breadboard was illustrated in Figure 3.2. In this measurement, two first components, an objective and first ImSpector™, are used and the image sensor is positioned in place of the LCD. An image of the target is shown in Appendix A.3. The ImSpector™ was fixed on the optical table and the 2D image sensor was mounted on a 3-axis motorised positioning stage. The objective and image sensor were focused on a slit at a distance of 2680 mm. The slit was illuminated by the neon lamp thought

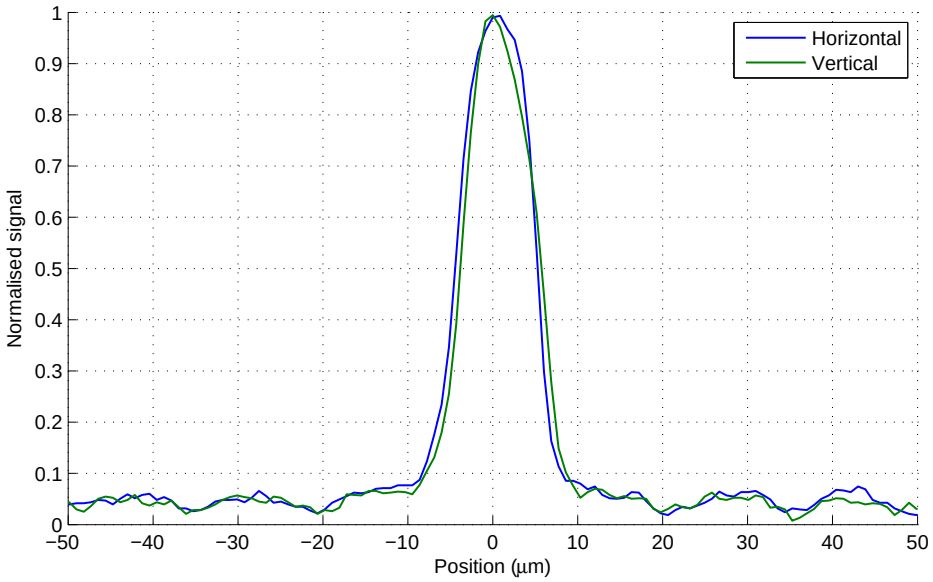

Figure 4.9. Epson LCD pixel transmission profile for diffuse light in vertical and horizontal directions.

a fibre. In this measurement, there are four adjustable degrees of freedom; three axes for the position of the image sensor and one for focusing the objective.

The initial situation is shown in Figure 4.10(a), where the neon lamp was put near the objective which was focused at infinity. Thus, the input slit of the ImSpector™ was filled by the uniform illumination. After that, the image sensor was focused based on the contrast in spectral direction. Second, shown in Figure 4.10(b), the light source with a slit was moved 2680 mm apart and the objective was focused while the image sensor was kept in the same position.

These two steps allowed a coarse focusing, but more accurate focusing is needed to be carried out. The best focus was found through the iterative process of focusing both the objective and image sensor for maximum signal on the image sensor. The output image of the ImSpector™ is shown in Figure 4.11. 400 pixels in the spectral axis and 80 pixels in the spatial axis are shown in this image. A 3D illustration of Figure 4.11 is shown in Appendix C.1.

According to the manual of ImSpector™ [18], the dispersion D_λ is constant. The dispersion defines the spatial separation of wavelengths [29]. Thus, the correlation between the wavelengths λ_i and pixels N_i is linear:

$$\lambda_i = \Delta P_{CCD} D_\lambda (N_i + N_{offset}), \tag{4.3}$$

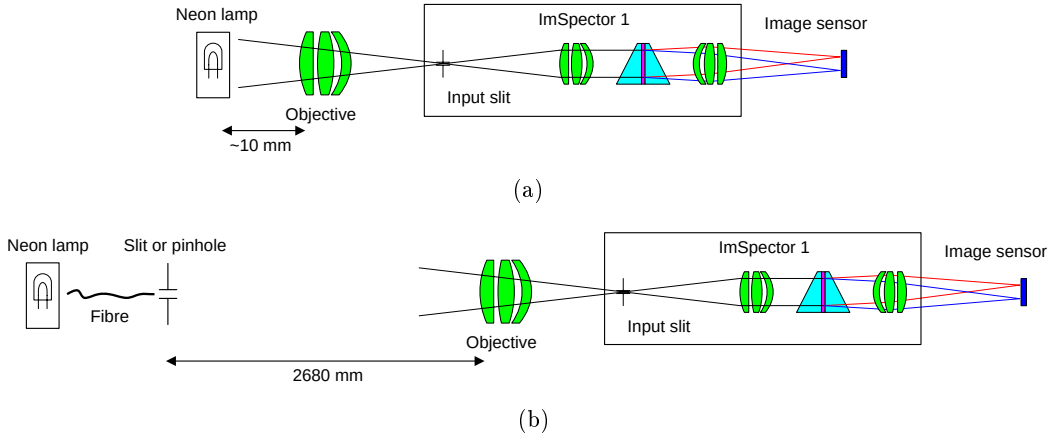

Figure 4.10. Block diagrams of ImSpector™ measurement. (a) The neon lamp is next to the objective in the first step and (b) faraway in the second step.

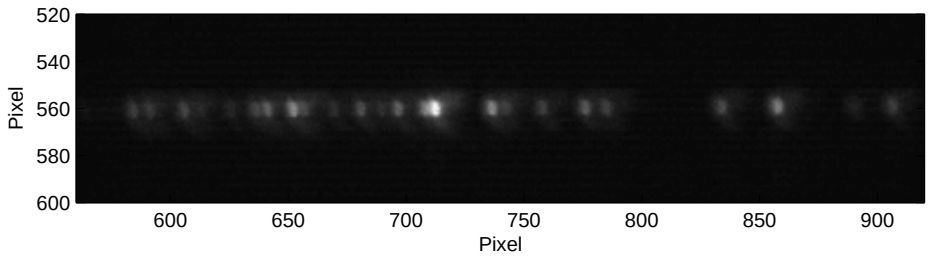

Figure 4.11. Output image of ImSpector™. The slit width of the light source was 2 mm at a distance of 2680 mm.

where N_{offset} is an adjustable pixel number offset, $\Delta P_{CCD} = 4.4$ μm is the pixel pitch of the image sensor and $D_\lambda = 97.5$ nm/mm is the dispersion of ImSpector™ [18].

When the pixel pitch and dispersion are known, the spectral and spatial resolutions can be analysed. The spectral profile of Figure 4.11 is shown in Figure 4.12. From Figure 4.12, the spectral peaks of the neon lamp can be seen which correspond to the known spectral peaks of the neon. The FWHMs of the measured peaks are between 2 nm and 3 nm. The FWHM values for different sizes of target slit or pinhole do not differ significantly because the spectral resolution is defined by the input slit of the ImSpector™. The manufacturer reports the spectral resolution to be 2.8 nm for a 30 μm input slit [18]. This information is consistent with the measured value.

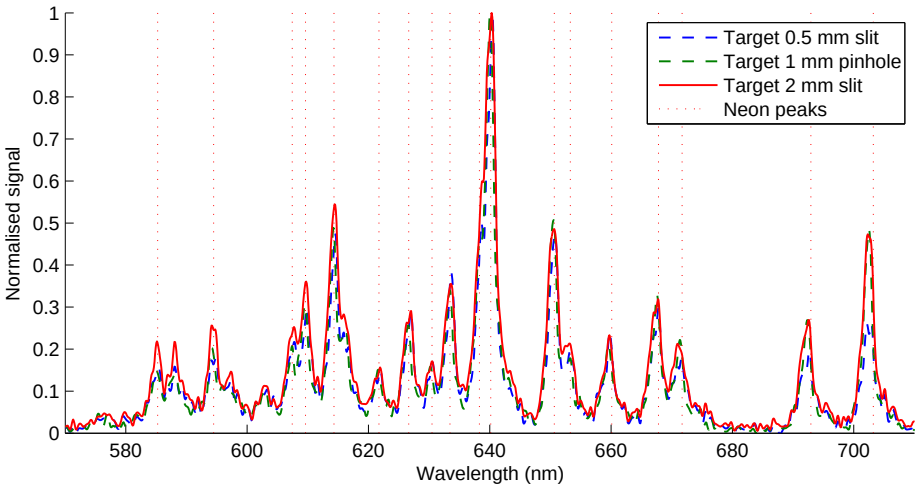

Figure 4.12. Spectral profile of output image of ImSpector™ in Figure 4.11. The horizontal axis has been converted from pixel numbers to wavelength using pixel pitch and dispersion (see Equation 4.3). Known positions of neon spectral peaks are marked with vertical lines. The FWHM values of the peaks are FWHM=3.0 nm @ 615 nm, FWHM=2.8 nm @ 640 nm, FWHM=2.2 nm @ 650 nm, FWHM=2.5 nm @ 667 nm and FWHM=2.0 nm @ 702 nm. FWHM values for the different sizes of target slit or pinhole do not differ significantly.

The spatial profile of Figure 4.11 at the highest peak is shown in Figure 4.13. The FWHM values of the peaks are 29.3 μm for a 2 mm target slit, 16.3 μm for a 1 mm target pinhole, and 8.1 μm for an 0.5 mm target slit. In this set-up the slit size of 0.5 mm could be considered as a point source. That is because the image of the target slit on the input slit of ImSpector™ is only 6.6 μm whereas the size of the input slit of the ImSpector™ is 30 μm. The spatial resolution reported by the manufacturer is < 9 μm [18].

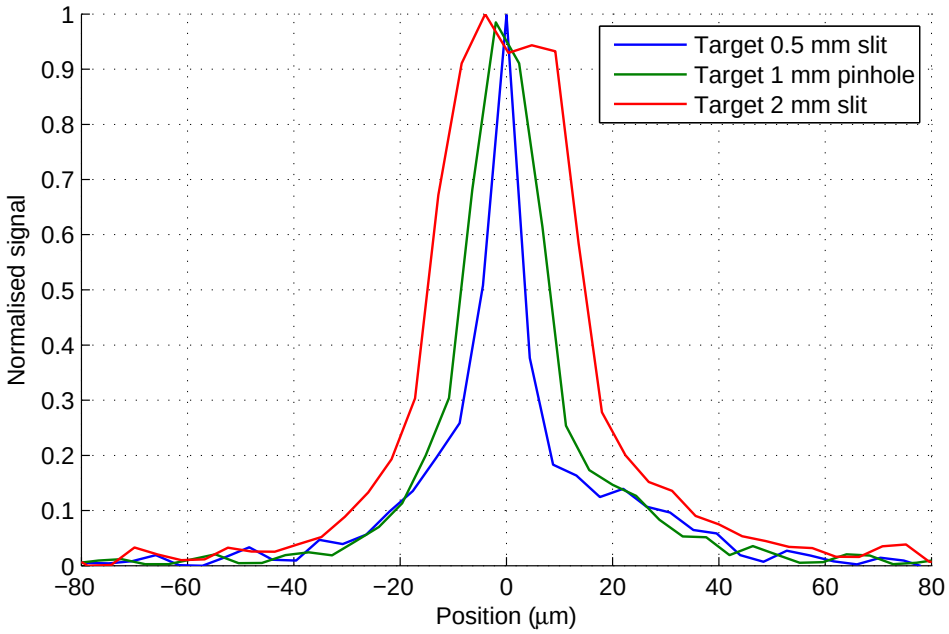

Figure 4.13. Spatial profile of output image of ImSpector™ in Figure 4.11 at 640 nm. Horizontal axis has been converted to micrometres using the pixel pitch.

Figure 4.13 presents the widths of target slits seen by the system. In fact, a more general way is to show a Fourier transform of the peaks shown in Figure 4.13 [45]. These curves, shown in Figure 4.14, represent the modulation between light and dark areas of the target image (see Figure 4.5 for example) as a function of spatial frequency. These curves are discussed in more detail in the following chapters.

4.4 Summary

In this chapter, components planned for the ISSI breadboard were characterised. The characterisation measurements were carried out for polarisers, Epson HTPS LCD and ImSpector™.

The polarisers were characterised by means of transmission. The transmission was found to be adequate for wavelengths longer than 450 nm. But the contrast-ratio of ColorPol™ polarisers was found to be problematic at wavelengths shorter than 550 nm. Because of this, an extra filter has to be used to reject leakage signal.

Epson HTPS LCD was characterised by means of overall transmission and pixel spatial transmission. The total transmission of the LCD and polarisers for random polarised light was found to be between 7% and 17% that is quite poor, but consistent

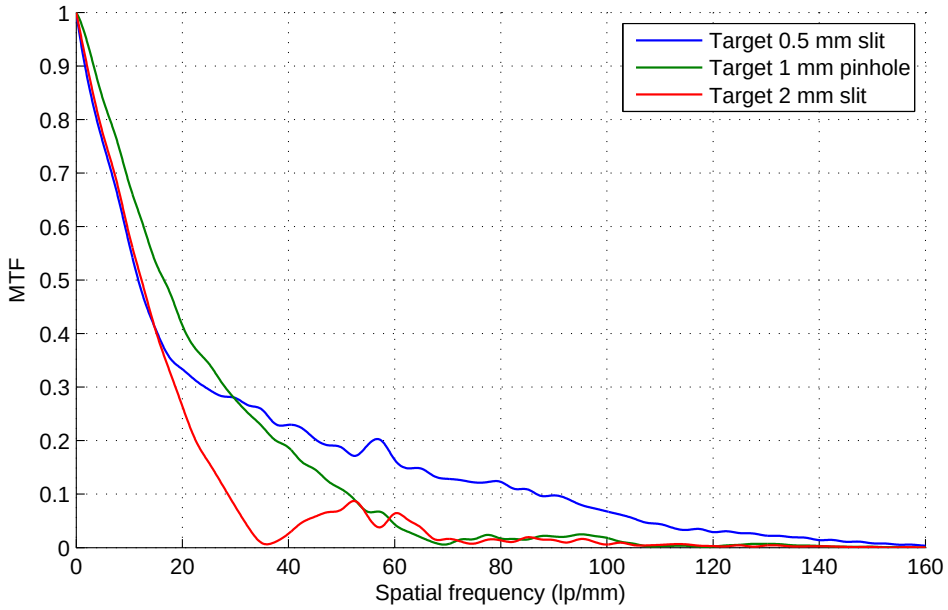

Figure 4.14. Spatial resolution of ImSpector™.

with the information provided by the manufacturer. Also, the LCD pixel aperture behaviour was characterised by using a pixel spatial transmission measurement. As a result, the aperture size was found to be slightly rectangular with horizontal and vertical sizes of 10 μm. Pixel pitch was found to be 14 μm which is consistent with the information provided by the manufacturer. The minimum f-number for the LCD was found to be approx. 4 which is adequate for the planned ISSI breadboard.

The ImSpector™ was characterised by means of spectral and spatial resolution. The results are fully consistent with the information provided by the manufacturer. The spectral resolution was found to be between 2 nm and 3 nm and spatial resolution below 9 μm at the wavelengths between 600 nm and 700 nm.

As a summary, the components planned for the ISSI breadboard were characterised and the results were consistent with the information provided by the manufacturers.

Chapter 5

Simulation of Instrument Performance

In this chapter, the instrument performance simulator is introduced and comparison simulations are carried out for the concepts described in Chapter 3. The purpose is to find a feasible concept for the breadboard in terms of mass, volume and budget.

5.1 Instrument Performance Simulator

The purpose of the instrument performance simulator is to find out preliminary radiometric and resolution performances. The measure of radiometric performance is the signal-to-noise ratio (SNR) at the image sensor. By means of the point spread function (PSF), the resolution performance can be evaluated. The PSF describes how much a singular light spot spreads when propagating through an optical component or system. In this case, this further determines the spatial and spectral resolutions.

The instrument performance simulator has been developed in the Matlab environment. As as result, three separate scripts can be used to simulate the performance of the ISSI concepts; radiometric, spatial resolution and spectral resolution.

5.1.1 Radiometric Simulator

In the radiometric simulator, the spectral radiant flux is calculated after every component by beginning from the atmospheric radiation at the altitude of the objective. A block diagram of the radiometric simulator is shown in Figure 5.1.

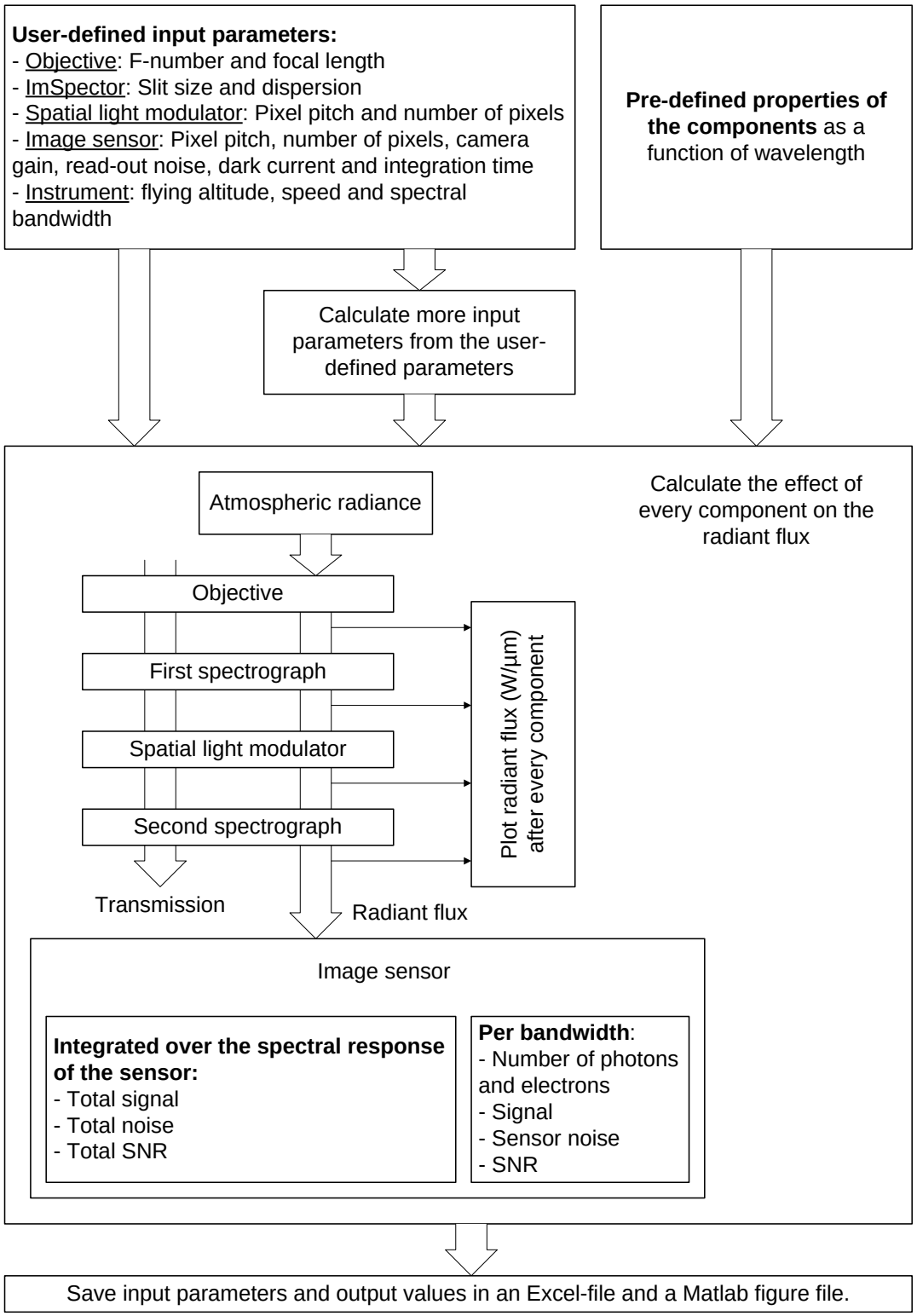

Figure 5.1. Diagram of radiometric simulator.

In the simulator, spectral radiant fluxes $\Phi_{\lambda,i+1}$ are calculated after every component, using the equation

$$\Phi_{\lambda,i+1} = T_i \Phi_{\lambda,i}, \tag{5.1}$$

where T_i is the transmission and $\Phi_{\lambda,i}$ is the spectral radiant flux after the i:th component, respectively.

Objective

Magnification of the objective is [29]

$$M = \frac{f}{H - f} \approx \frac{f}{H}, \quad H >> f, \tag{5.2}$$

where f is focal length and H is flying altitude. Field-of-view (FOV) indicates the angular aperture size of the instrument. The across-track FOV of the instrument in this case is

$$FOV = 2 \tan^{-1} \left(\frac{1}{2} \frac{\min\{H_{slit}, H_{SLM}, H_{CCD}\}}{f} \right), \tag{5.3}$$

where H_{slit}, H_{SLM} and H_{CCD} are the heights of the slit, SLM and image sensor, respectively. Instantaneous FOV (IFOV) defines the angular aperture for a single pixel. The IFOV in the along-track direction on-axis is

$$IFOV_{\parallel} = 2 \tan^{-1} \left(\frac{1}{2} \frac{W_{slit}}{f} \right), \tag{5.4}$$

where W_{slit} is the input slit width. Correspondingly, the IFOV in the across-track direction on-axis is

$$IFOV_{\perp} = 2 \tan^{-1} \left(\frac{1}{2} \frac{\max\{\Delta P_{CCD}, \Delta P_{SLM}\}}{f} \right), \tag{5.5}$$

where ΔP_{CCD} and ΔP_{SLM} are the pixel pitches of the image sensor and spatial light modulator, respectively. Ground sampling distance (GSD) indicates the distance between two adjacent ground pixels. The GSD in the across-track direction on-axis is therefore

$$GSD_{\perp} = 2H \tan \left(\frac{IFOV_{\perp}}{2} \right) = \frac{\max\{\Delta P_{CCD}, \Delta P_{SLM}\}}{M}, \tag{5.6}$$

where the latter part is given by Equations 5.5 and 5.2. And the GSD in the along-track direction on-axis is

$$GSD_{\parallel} = 2H \tan \left(\frac{IFOV_{\parallel}}{2} \right) = \frac{\Delta W_{slit}}{M}, \tag{5.7}$$

where the latter part is given by Equations 5.4 and 5.2. The ground pixel is seen in the solid angle [29]

$$\Omega = \frac{GSD_{\parallel} GSD_{\perp}}{H^2} \tag{5.8}$$

from the objective. The area of the objective is [29]

$$A_{\text{obj}} = \pi \left(\frac{f}{2 \cdot f/\#} \right)^2, \tag{5.9}$$

where f/# is the f-number of the objective. Thus, the received spectral radiant flux from the nadir ($\psi = 0°$) per image sensor pixel can be calculated using Equation 2.5:

$$\Phi_\lambda = L_{\lambda,a} A_{obj} \Omega, \tag{5.10}$$

where $L_{\lambda,a}$ is the spectral radiance at the altitude of the objective.

LCD and polarisers

Transmission of two polarisers as a function of the mutual rotation θ for random polarised light is [29]

$$T_\theta = T_{\parallel} \cos^2 \theta + T_{\perp} \sin^2 \theta, \tag{5.11}$$

where $T_{\parallel}$ and $T_{\perp}$ are the transmission of the two polarisers in parallel and perpendicular directions, respectively. The contrast-ratio C is the ratio between maximum and minimum transmissions, i.e. [37]

$$C = \frac{T_{\parallel}}{T_{\perp}}. \tag{5.12}$$

Thus, using Equation 5.12, Equation 5.11 can be written as

$$T_\theta = T_{\parallel} \left(\cos^2 \theta + \frac{1}{C} \sin^2 \theta \right). \tag{5.13}$$

Including the LCD, which turns the polarisation state, can be thought to be equivalent to the situation where two single polarisers are turned. Therefore, the modulation m can be written as

$$m = \cos^2 \theta \quad \text{and} \tag{5.14a}$$

$$1 - m = \sin^2 \theta. \tag{5.14b}$$

According to Equation 5.13, the transmission of two parallel polarisers is the product of two polarisers for linear polarisers light and the transition from random to linear

polarisation, i.e.

$$T_{\parallel} = T_p^2 \frac{\int_0^{2\pi} (\cos^2\theta + C^{-1}\sin^2\theta)\, d\theta}{\int_0^{2\pi} d\theta} = T_p^2 \frac{1 + C^{-1}}{2}, \tag{5.15}$$

where T_p is the transmission of a single polariser for linear polarised light. For most of cases the effect of contrast-ratio can be omitted because the contrast-ratio is usually very large, typically $10 \ldots 10000$.

Substituting Equations 5.14 and 5.15 into Equation 5.13, the transmission of two parallel polarisers and the LCD as a function of modulation is

$$T_{\parallel,p+LCD} = T_\theta T_{LCD} = T_p^2 \frac{1 + C^{-1}}{2} \left(m + \frac{1}{C}(1 - m) \right) T_{LCD}, \tag{5.16}$$

where T_{LCD} is the transmission of the LCD for linear polarised light. The modulation m of the LCD is a function of applied voltage and it is between 0 and 1.

Image sensor

The total spectral radiant energy incident on the image sensor is the product of spectral radiant flux, integration time and wavelength band according to Equation 2.2. The number of incident photons on the image sensor is the total spectral radiant energy divided by the energy of a single photon. According to Equations 2.1 and 2.2, the number of incident photons on the image sensor is

$$n_{photons} = \frac{\Phi_{\lambda,i-1} t_{int} \Delta\lambda}{Q} = \Phi_{\lambda,i-1} \frac{\lambda}{hc} t_{int} \Delta\lambda, \tag{5.17}$$

where Q is the energy of a single photon, $\Phi_{\lambda,i-1}$ is incident spectral radiant flux, t_{int} is integration time and $\Delta\lambda$ is wavelength band. The number of electrons that are produced by the photons is [45]

$$n_{electrons} = \eta n_{photons}, \tag{5.18}$$

where η is the quantum efficiency of the image sensor. The signal per pixel can now be calculated as [45]

$$S = \frac{n_{electrons}}{K}, \tag{5.19}$$

where K is a camera gain (e^-/ADU). The noise in electrons is [45]

$$\sigma_{tot} = \sqrt{\sigma_{ro}^2 + I_{dark} t_{int} + n_{electrons} + \left(\frac{K}{\sqrt{12}} \right)^2}, \tag{5.20}$$

where σ_{ro} and I_{dark} are read-out noise (rms e^-) and dark current of the image sensor (rms e^-/s), respectively. The last term in Equation 5.20 represents the quantization noise of the analogue-to-digital conversion. So, read-out noise, dark current noise, photon shot noise and quantization noise are included in the calculations.

The signal-to-noise ratio (SNR) is [45]

$$SNR = \frac{n_{electrons}}{\sigma_{tot}}. \tag{5.21}$$

In remote sensing applications, the integration time and flying speed should be chosen so that there wouldn't be any blind areas between the acquired images and, on the other hand, the smear should be kept low. Therefore the maximum integration time is

$$t_{int,max} = \frac{(1 - POL)GSD_{\parallel}}{v}, \tag{5.22}$$

where POL is pixel overlapping and v is flying speed. Pixel overlapping defines how much the ground pixels on the swath are overlapped between two consecutive pixel lines, i.e. if $POL = 0.25$, then 25% of the along-track GSD is overlapped. The situation is clarified in Figure 5.2.

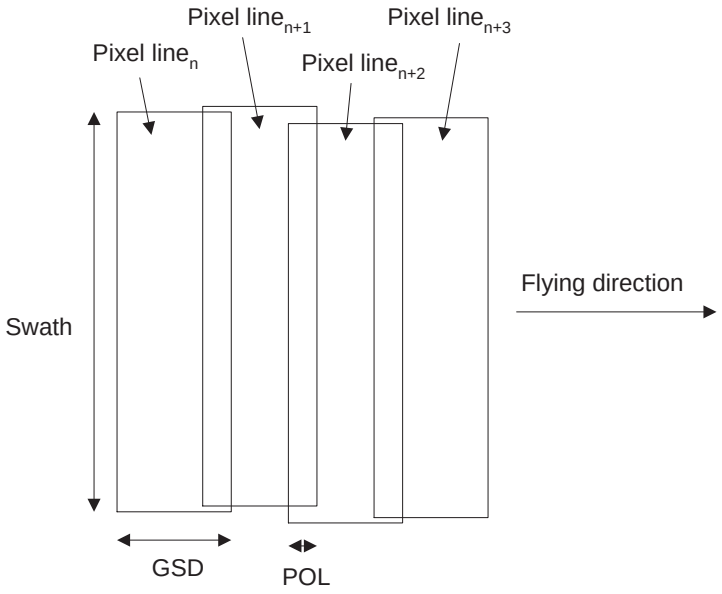

Figure 5.2. Definition of pixel overlapping.

5.1.2 Spatial and Spectral Resolution Simulators

The resolution of the instrument is evaluated by defining the PSF for the whole instrument, which is started by defining the PSF for every component. The flow chart of the calculation process in the spatial resolution simulator is shown in Figure 5.3 and for the spectral resolution simulator in Figure 5.4.

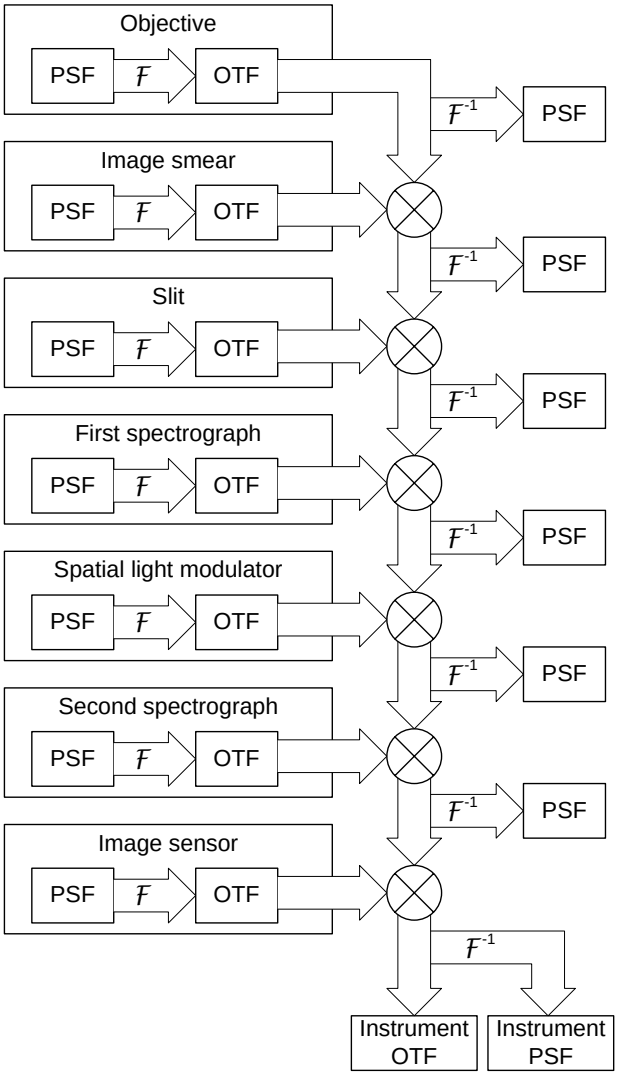

Figure 5.3. Diagram of spatial resolution simulator. Using component-specific point spread functions (PSF) and Fourier transform, optical transfer function (OTF) for the instrument can be calculated by taking a product of component-specific OTFs.

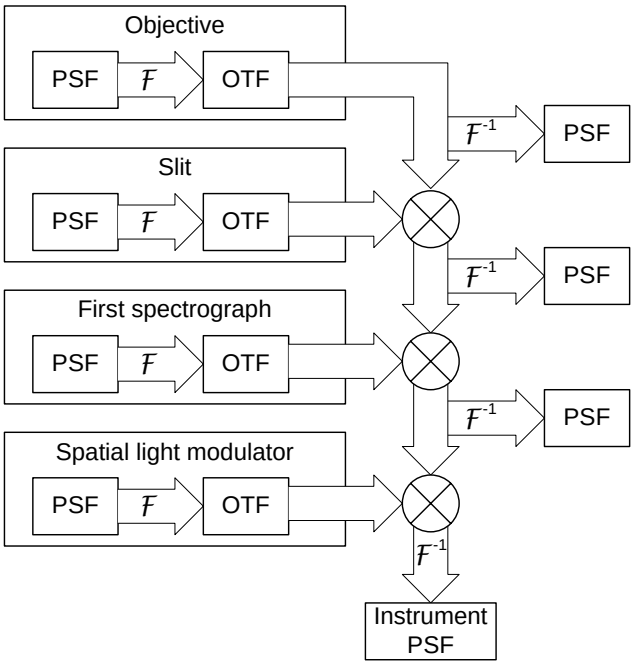

Figure 5.4. Diagram of spectral resolution simulator.

An analytic approximation for the PSF is

$$PSF = \left(1 + \left(\frac{s}{0.5 \cdot FWHM}\right)^{p}\right)^{-1}, \tag{5.23}$$

where p is a parameter that defines the steepness of the edge, $FWHM$ is full-width at half-maximum of the PSF and s is spatial position, in steps of Δs,

$$s = -s_{min} \ldots s_{max}, \tag{5.24}$$

where s_{min} and s_{max} are the outermost spatial positions considered. The function defined in Equation 5.23 is simply an unit box function with slightly inclined and rounded edges. The PSF should be measured for every component if it is possible, and if not, the analytic approximation of Equation 5.23 can be used.

The optical transfer function (OTF) is a Fourier transform of the PSF and vice versa, i.e. [29]

$$OTF_i = \mathcal{F}\{PSF_i\} \quad \text{and} \tag{5.25a}$$

$$PSF_i = \mathcal{F}^{-1}\{OTF_i\}, \tag{5.25b}$$

where the different components are separated with lower index. In the discrete Fourier transform, the spatial positions are changed to spatial frequencies:

$$\nu = 0 \ldots \Delta\nu(N_s - 1), \tag{5.26}$$

where the frequency step is

$$\Delta\nu = \frac{1}{\Delta s \cdot N_s} \tag{5.27}$$

and N_s is a number of spatial points (i.e. the number of s:s in Equation 5.24), that is

$$N_s = 1 + \frac{s_{max} - s_{min}}{\Delta s}. \tag{5.28}$$

The PSF of two serial connected components is a convolution of the PSFs of the two components, i.e

$$PSF_{i,i+1} = PSF_i * PSF_{i+1}. \tag{5.29}$$

According to the convolution theorem [57], the OTF of serial connected components is the product of the individual OTFs,

$$OTF = \prod_{i=1}^{N_c} OTF_i, \tag{5.30}$$

where N_c is the number of components. Further, using Equations 5.25 and 5.30, the PSF for the whole instrument can be written as

$$PSF = \mathcal{F}^{-1}\left\{\prod_{i=1}^{N_c} \mathcal{F}\{PSF_i\}\right\}. \tag{5.31}$$

The OTF is a complex function. The modulation transfer function (MTF) gives the amplitude of the OTF and the phase transfer function gives the phase. In this context, the MTF is the most interesting function

$$MTF = |OTF|. \tag{5.32}$$

5.2 Simulation Results

In this section, the simulation results are presented. The purpose is to compare the performance of the concepts and to find the most feasible concept for the ISSI bread-board.

First, the radiometric throughputs of the concepts are analysed. The throughput is analysed by means of transmission as clarified in Figure 5.1. The transmission of the objective is unknown; thus the constant value $T = 0.95$ is used. The transmission of the ImSpector™ is given by Specim and was shown in Figure 2.10. The measured transmission of the polarisers and the Epson HTPS LCD were presented in Sections 4.1 and 4.2. The extra filter, OG515 (see Appendix D.1 for the transmission data), is included due to the poor contrast-ratio of the polarisers at wavelengths below 550 nm. The reflectance of the Holoeye LCoS was approximated to be constant, $T = 0.6$, based on [49]. Both the transmission and reflectance of the beam splitter were approximated to be $T = 0.5$. Based on these assumptions, the transmission simulation results are shown in Figure 5.5.

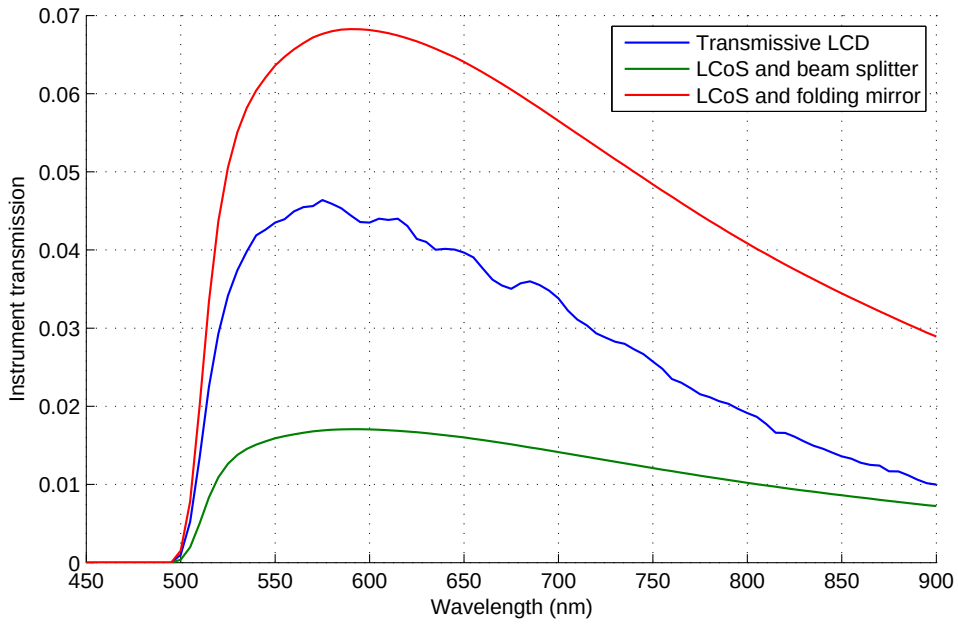

Figure 5.5. Simulated instrument transmissions. Transmissions for the concepts described in Chapter 3 are shown.

Figure 5.5 shows the difference between the concepts. The transmission is highest for the concept with the folding mirror. Correspondingly, transmission is lowest when the beam splitter is used due to the attenuation of signal every time the beam splitter is traversed. Transmission between these values can be obtained using the concept of the transmissive LCD. With the LCD, the transmission is between 1% and 4.5%. The result is barely adequate, because the result shows that more than 95% of the signal is lost while propagating through the instrument. In this concept, the biggest reason for

low transmission is the transmission of the LCD itself. Also, the first polariser always changes the random polarised light into linear polarised light thus halving the signal (see Equation 5.15 for details).

The spatial resolution of the concepts is evaluated by means of the MTF. The calculation procedure was clarified in Figure 5.3. Since the PSF of the objective is unknown, it was approximated using the PSF of the Rodenstock Apo-Rodagon-D objective. The spatial profile of the PSF of ImSpector™ was used. Specim delivered the Zemax™ simulated 3D PSF data for the ImSpector™. In Section 4.2.2, the measured pixel spatial transmission of the Epson LCD was used in this simulation to represent the PSF. Only two simulations are needed because the spatial resolution is exactly the same for the two concepts based on the LCoS. On-axis simulation results for the wavelength 700 nm are shown in Figure 5.6.

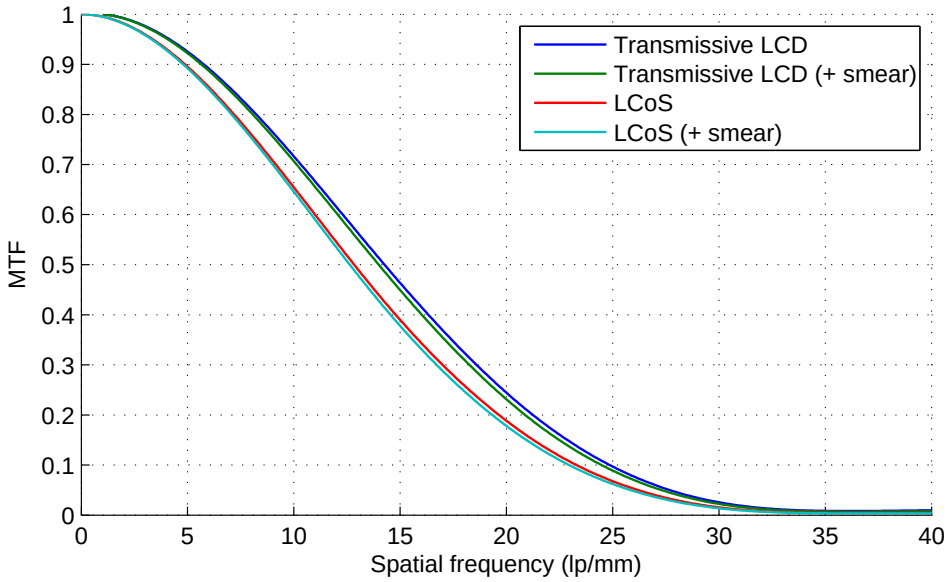

Figure 5.6. Simulated instrument spatial resolutions. Simulations were carried out on-axis at 700 nm. The effect of smear was calculated using assumptions of $H = 5$ km, $v = 65$ m/s and $t_{int} = 20.0$ ms, which is negligible because the other components have more significant effect to the total spatial resolution.

Figure 5.6 shows that the resolving power of the transmissive LCD based concept seems to be slightly better than two other concepts with the reflective LCoS. The difference is due to the PSF of the objective which is used twice in the LCoS based concepts; an extra imaging objective is not needed in the transmissive LCD based concept (see Figures 3.1, 3.3 and 3.4).

Finally, the spectral resolutions of the concepts are analysed. The simulation procedure was shown in Figure 5.4. The spectral resolutions are analysed by means of the FWHM values of the PSF curves at the spectral axis after the SLM. The components from the objective to the SLM define the spectral resolving power of the instrument. The spectral profile of the PSF of the ImSpector™ was used. The simulation results are shown in Figure 5.7. The spectral resolving power seems to be quite similar for all concepts which is due to quite similar optical paths. The result indicates that the instrument is capable of discriminating between wavelengths that are approx. 3 nm apart from each other.

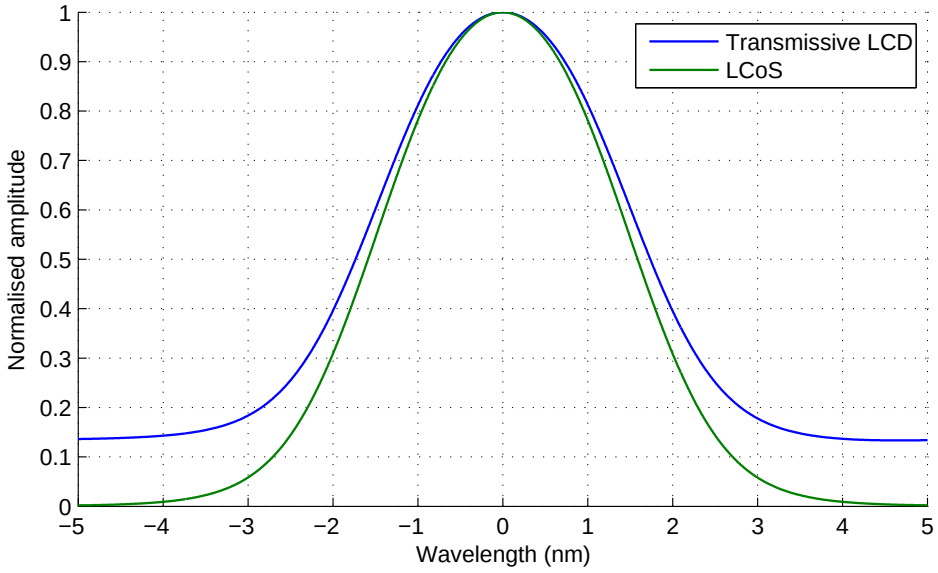

Figure 5.7. Simulated instrument spectral resolutions. Simulations were carried out on-axis at 700 nm. The FWHM values for the peaks are 3.2 nm for the LCoS and 3.5 nm for the LCD based instrument. Non-zero values at both ends of the curve for the LCD is due to leakage signal outside the pixel that can be seen in Figure 4.9. This leakage is caused by the polarisers.

5.3 Radiometric Simulations of Airborne Imaging Data

In this section, some relevant atmospheric radiation values are presented which are used as input values for the radiometric simulator.

The spectral radiance values are generated using the MODTRAN4 [8] atmosphere simulation program. The input parameters are listed in Appendix B.1. The place, year and time of day of the simulation are selected to represent the average imaging

conditions for the mission. Simulated spectral radiance values at the altitude of 5 km are shown in Figure 5.8.

Figure 5.8 shows that radiance values differ greatly. Atmospheric attenuation (see Figure 2.4) can be clearly seen at the wavelengths of 720 nm, 760 nm, 814 nm, 930 nm and also below 400 nm.

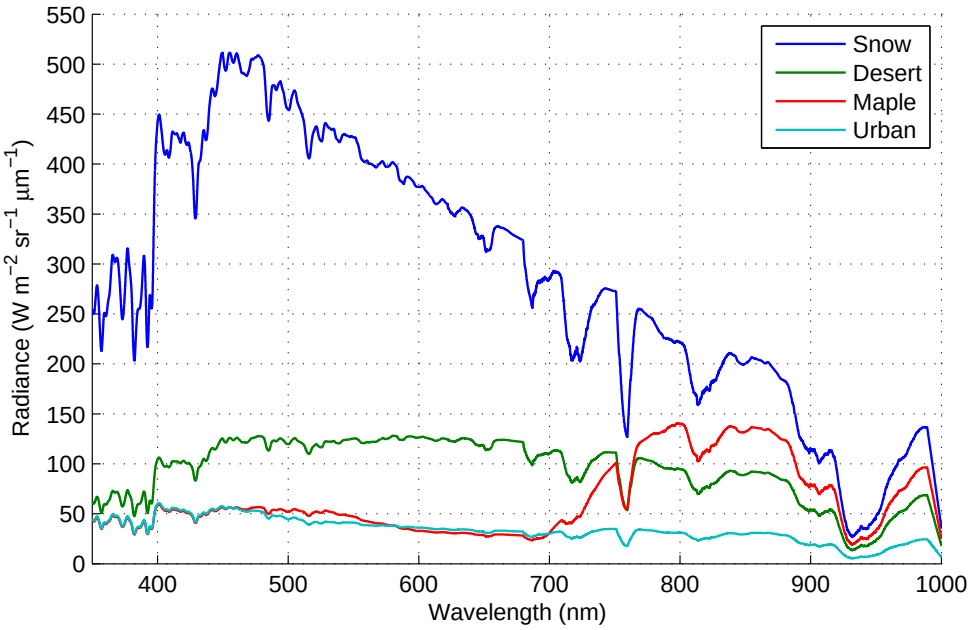

Figure 5.8. MODTRAN4 spectral radiance simulations for different ground types in the wavelengths from 350 nm to 1000 nm. Simulation parameters are shown in Appendix B.1.

The spectral radiant flux after every component, detector signal and SNR values, can be estimated using the radiometric simulator as shown in Figure 5.1. The concept with two ImSpectors™ and the transmissive LCD, which was described in Section 3.1, is analysed using these values. The simulation parameters are the same as in Section 5.2. In all these simulation, only one wavelength band of $\Delta\lambda = 7$ nm is selected at a time on the LCD. The simulation parameters are shown in Appendix B.2. The simulated spectral radiant fluxes after every component for the ground type of maple are shown in Figure 5.9. It can be clearly noted that the LCD and polarisers attenuate the signal dramatically when compared to the effects of the other components. Also, the effect of the extra filter, OG515 (see Appendix D.1 for the transmission data), which is mounted between the polarisers, is seen in Figure 5.9.

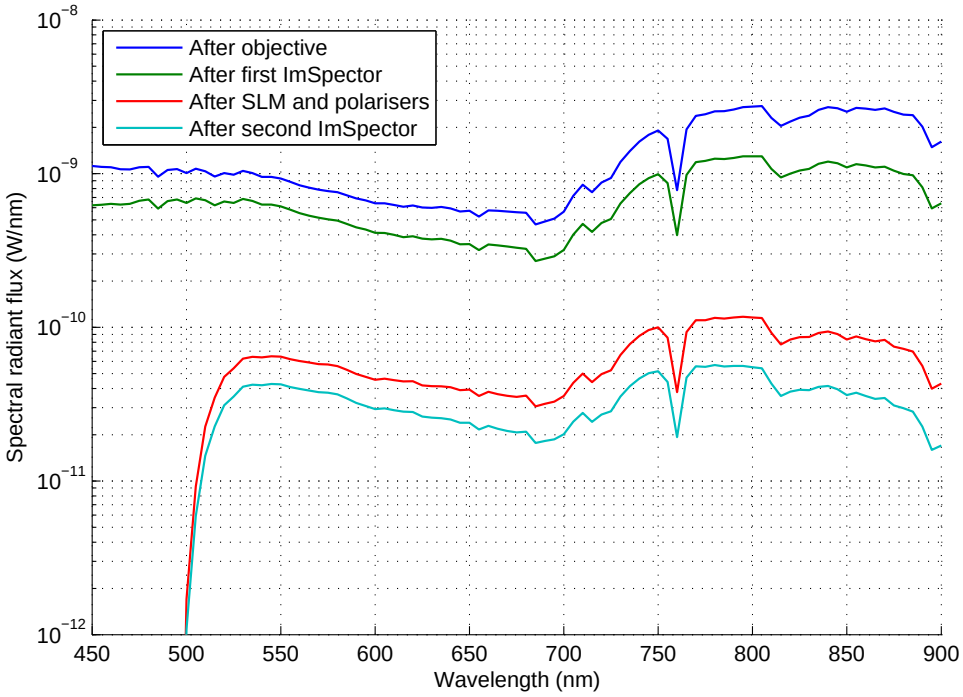

Figure 5.9. Simulated spectral radiant flux values. Ground type is maple. A wavelength band of $\Delta\lambda = 7$ nm was used.

The lowest curve in Figure 5.9 represents the spectral radiant flux incident on the image sensor. Using integration time and properties of a typical image sensor, signal values can be calculated using the method described in Section 5.1.1. The signal and SNR values for some different ground types are shown in Figures 5.10 and 5.11. From these figures it can be seen that the signal, but also the SNR, get quite low for some ground types. These simulations represent the case when a single band of 7 nm is selected on the spatial light modulator. The signal and SNR values increase linearly with increasing bandwidth. The spectral bandwidth can be increased either by broadening a single band or selecting multiple separated bands. The latter is probably the case to be used in the final application.

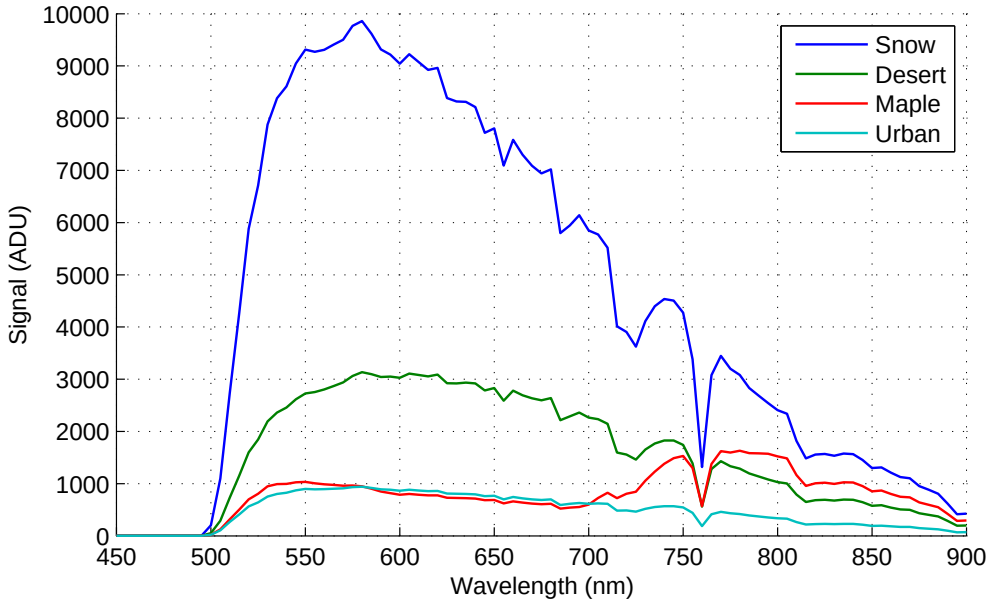

Figure 5.10. Simulated image sensor signal values. A wavelength band of $\Delta\lambda = 7$ nm and integration time $t_{int} = 20.0$ ms were used.

5.4 Summary

All ISSI concepts have now been described and simulated. Spectral and spatial resolution differences between the concepts are negligible. Also, off-axis simulations were carried out, but the difference is insignificant. However, remarkable differences arise when the throughput properties are analysed. The most suitable concepts seems to be the ImSpector™ with the Holoeye LCoS with the folding mirror and the concept with the transmissive Epson LCD. The first concept does not offer a dramatic improvement

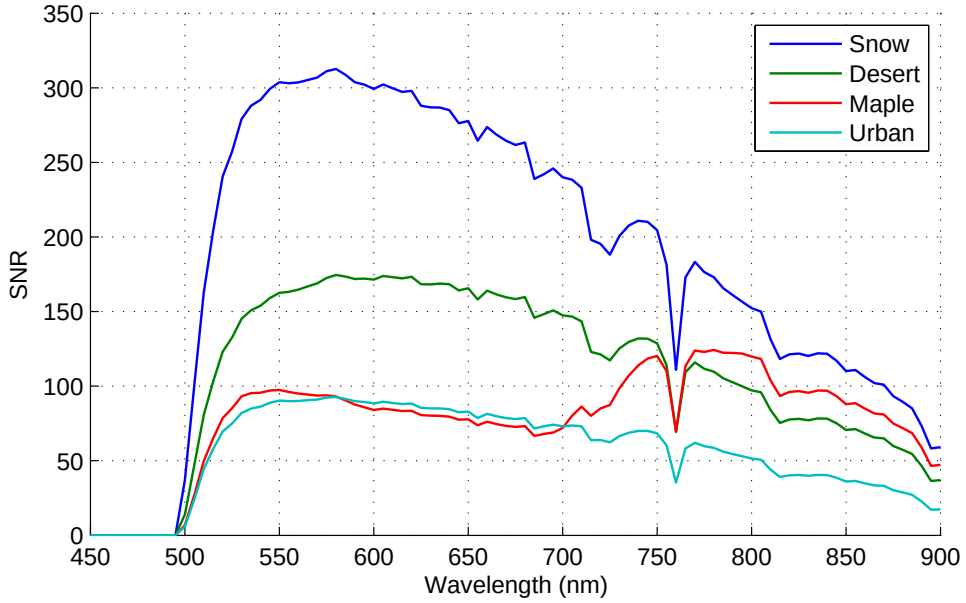

Figure 5.11. Simulated image sensor SNR values. A wavelength band of $\Delta\lambda = 7$ nm and integration time $t_{int} = 20.0$ ms were used.

in performance with respect to the transmissive LCD. The modification of the ImSpector™ is beyond the project scope due to budget reasons. Therefore, the best concept for the ISSI breadboard is two ImSpectors with a transmissive LCD as described in Section 3.1.

The radiometric simulations for a mission with the selected concept was carried out. The simulations show that the LCD has biggest impact on the radiometric performance due to it's poor transmission. Despite of that, the image sensor signal and SNR are barely adequate for imaging when only a single band of 7 nm is selected on the LCD. After increasing the spectral band, the signal and SNR values improve significantly, which is probably the case in the final application.

Chapter 6

Instrument Characterisation

In this chapter, the ISSI breadboard is introduced and performed characterisation measurements are analysed. The components for the breadboard are selected based on the analysis done in the previous chapters. Finally, measurement results are compared to the simulated ones. Photographs of the breadboard and target are shown in Appendix A.3.

6.1 Instrument Breadboard Components

The selected objective is Schneider-Kreuznach with $f = 35$ mm and $f/\# = 4$ due to its easy availability and adequate feasibility for the breadboard. In this objective, the focus and f-number can be manually adjusted. Even though, the simulations were carried out using the Rodenstock Apo-Rodagon-D objective, the difference is negligible. The difference is small because all other components have much larger impact on the total resolution performance.

Two V10E ImSpectors™ are used [18]. The width of the input slit of the first ImSpector™ is 30 μm. The slit of the second ImSpector™ is removed because the image sensor should be placed exactly on the same place as the slit (see Figure 3.1 for details). The spatial and spectral resolutions were measured and compared with the information provided by the manufacturer in Section 4.3.

The selected spatial light modulator is the Epson HTPS LCD, model L3P05S-46G10 [47]. This component was characterised for the transmission, pixel structure and f-number in Section 4.2.

The manufacturer of the polarisers is Codixx and the model is ColorPol™ VIS 700 BC4 CW03 [54]. The measured transmission was reported in Section 4.1. An extra filter is also used, OG550 (see Appendix D.1 for the transmission data), due to the

poor contrast-ratio at wavelengths shorter than 550 nm. Simulations in Chapter 5 were carried out using OG515 (see Appendix D.1 for the transmission data) as an extra filter, but in the breadboard the OG550 filter is used to ensure that no leakage signal exists.

The selected image sensor is Atmel AViiVA SM2 CL line image sensor with 2048 pixels [58]. The image is acquired using a Labview™ and Camera Link interface.

The target is the same as in Figure 4.10(b), which consists of a neon lamp, fibre and replaceable slit or pinhole (see photograph in Appendix A.3). The distance between the target and objective was 2680 mm.

6.2 Component Adjustment Procedure

The objective focusing was reported in Section 4.3. After that, the 2D image sensor was replaced with the LCD that was observed with a microscope camera, in the same way as in Section 4.2.2. The LCD and image sensor were adjusted iteratively to find maximum signal on the image sensor. After that, the LCD was rotated with respect to the optical axis to adjust the spectral lines of a neon parallel to the LCD pixel rows. The pixel profile along the spectral axis seen by the microscope camera is shown in Figure 6.2.

The third step was to replace the microscope camera with the second ImSpector™ and position it accordingly using the same 2D image sensor as in the first step. Focusing was carried out in the same way as in the previous steps; adjusting both components iteratively to find the maximum signal on the image sensor. After that, the 2D image sensor was replaced with a line image sensor. Focusing was done by adjusting the image sensor to find maximum signal. Also, it was checked that the signal would be as even as possible between the pixels when the input slit of the first ImSpector™ was filled with uniform light. This was done by placing the neon lamp close to the objective.

After all adjustment steps, the ISSI breadboard was as photographed in Appendix A.3.

6.3 Characterisation Measurements

In this section, the ISSI breadboard characterisation measurements are reported. The measured values are spatial and spectral resolutions and also light modulation dynamic range.

6.3.1 Spatial Resolution Measurement

The spatial resolution was characterised in the same way as in Section 4.3 for the ImSpector™. Different sizes of target slits and pinhole were imaged to find the PSF. The slits and pinhole were illuminated with a neon lamp. During the measurements, all pixels of the LCD were selected. The MTF is a Fourier transform of the pixel values of the image sensor as described in Section 5.1.2.

The measured MTF curves for different sizes of the target slits are shown in Figure 6.1. Also, the corresponding ImSpector™ curves are shown that were reported in Section 4.3. Simulations in Section 5.2, model the spectral performance of the ISSI breadboard. Therefore, the simulated MTF is also shown in Figure 6.1 to compare measurements and simulations.

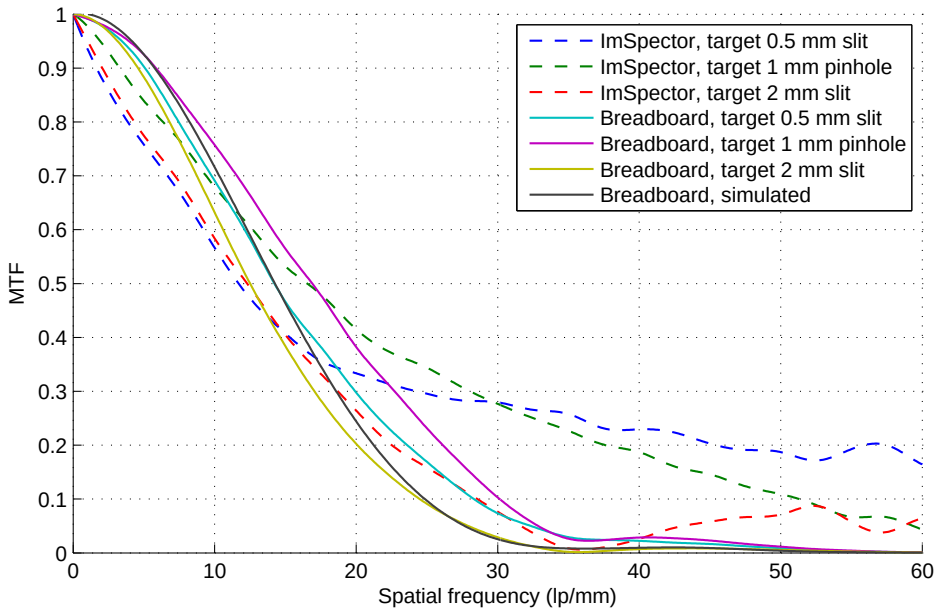

Figure 6.1. Measured breadboard spatial resolution.

Figure 6.1 shows that the simulated spatial resolution corresponds quite well with the measured one. The simulated MTF is for a singular point source and in this set-up the slit size of 0.5 mm could be considered as a point source. That is because the image of the target slit on the input slit of ImSpector™ according to Equation 5.2 is only 6.6 μm whereas the size of the input slit of the ImSpector™ is 30 μm.

The MTF, i.e. modulation between black and white areas, is defined as [45]

$$MTF = \frac{S_{max} - S_{min}}{S_{max} + S_{min}}, \tag{6.1}$$

where S_{max} are S_{min} maximum and minimum signal values in the black and white areas, respectively. According to Figure 6.1 for the MTF of 0.5 the spatial frequency is 14.2 lp/mm and for MTF=0.2, it is 23.6 lp/mm. These spatial frequencies are on the image sensor, but those can be projected on the ground using Equation 5.2 and simulation parameters in Appendix B.2. Corresponding across-track line widths on the ground are 5 m and 3 m, respectively. For the flying altitude of 2 km corresponding line widths are 2 m and 1.2 m, respectively.

The sampling frequency of an image sensor is [45]

$$\nu_s = \frac{1}{\Delta P_{CCD}}, \tag{6.2}$$

where ΔP_{CCD} is the pixel pitch of the image sensor. The highest frequency that can be faithfully reconstructed is one-half of the sampling frequency. This frequency, the Nyquist frequency, is therefore [45]

$$\nu_N = \frac{\nu_s}{2} = \frac{1}{2\Delta P_{CCD}} \tag{6.3}$$

Equation 6.3 gives the Nyquist frequency $\nu_N = 35.7$ lp/mm for the pixel pitch of $\Delta P_{CCD} = 14$ μm. According to the ISSI requirements in Table 3.1, the spatial resolution requirement is not met because the modulation should be 0.2 at the Nyquist frequency.

6.3.2 Spectral Resolution Measurement

The spectral resolution was measured using the ISSI breadboard in scanning mode. The slit of 2 mm was observed to fill the whole input slit of the ImSpector™. The spectral axis of the LCD, i.e. rows, was scanned by selecting two adjacent spectral pixels at a time and the signal value at the image sensor was detected. Two adjacent LCD pixels were selected because the spectral resolution of the first ImSpector™ is defined by the width of the input slit that is 30 μm. Therefore, the width of spectral sampling on the LCD should be as similar as possible. The pixel size of the LCD is 14 μm thus two adjacent pixels should be used for spectral scanning.

The signal value as a function of wavelength was gathered and is shown in Figure 6.2. In Figure 6.2 are also shown the spectral profile of the image of ImSpector™ reported in

Section 4.3 and the pixel profile along the spectral axis seen by the microscope camera described in Section 6.2.

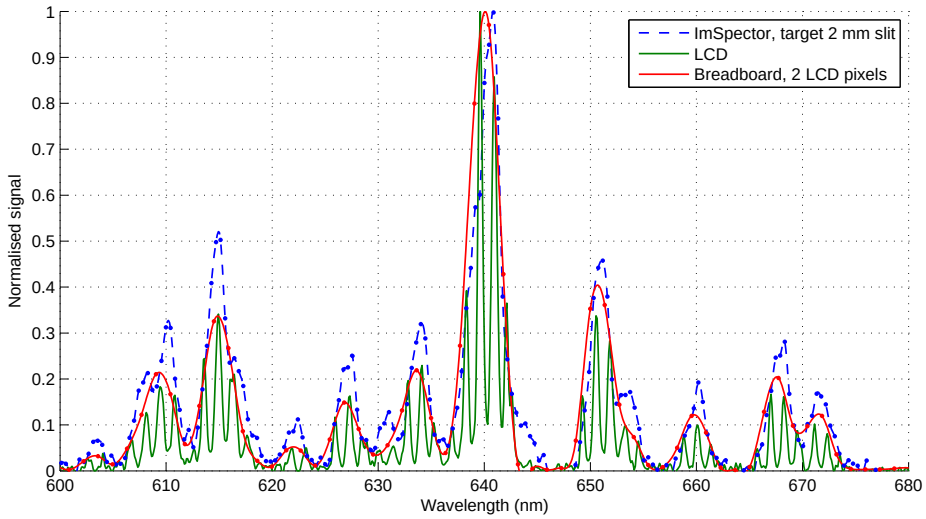

Figure 6.2. Measured breadboard spectral resolution. The FWHM values of the breadboard spectral resolution when two adjacent LCD pixels are selected are FWHM=3.1 nm @ 615 nm, FWHM=3.3 nm @ 640 nm, FWHM=3.0 nm @ 650 nm and FWHM=2.9 nm @ 667 nm.

From Figure 6.2 it can be seen that the FWHM values of the spectral peaks are slightly larger and some double peaks are merged together. This is due to additional optical components which decrease the resolution. The differences between the FWHM values, however, are negligible. The simulated spectral resolution in Section 5.2 was FWHM=3.5 nm at the wavelength of 700 nm. The measured values are slightly better for the wavelengths between 600 nm and 680 nm. The wavelength difference is negligible and also the FWHM difference is rather small.

This effect of the spectral sampling of the LCD that has the pixel pitch of 14 μm but the aperture size is only 10 μm (see Section 4.2.2 for measurements) can be clearly seen in Figure 6.2. The spectral sampling of the LCD is 1.37 nm/pixel after the calculated simulation parameters in Appendix B.2. However, this has only a minor effect to the total spectral resolution due to fact that there is always the minimum FWHM of spectral peaks which limited spectral resolution of ImSpector™. Because of that, a single spectral peak is always spread over two LCD pixels.

6.3.3 Light Modulation Dynamic Range and Linearity Measurement

The last measurement carried out for the ISSI breadboard was the analysis of the light modulation dynamic range and linearity. The purpose is to find the effective number of light modulation steps that the LCD is capable of producing. The capability to generate a feasible number of light modulation steps was one of the most important factors in the concept evaluation between the MMA and LC based concepts in Chapter 3.

The measurement was carried out by changing the transmission of the LCD and simultaneously detecting the signal at the image sensor. There are 255 possible voltage values to drive the LCD due to the driving being handled by the secondary monitor of the computer that has 8-bit quantization. The results for two consecutive measurements are shown in Figure 6.3.

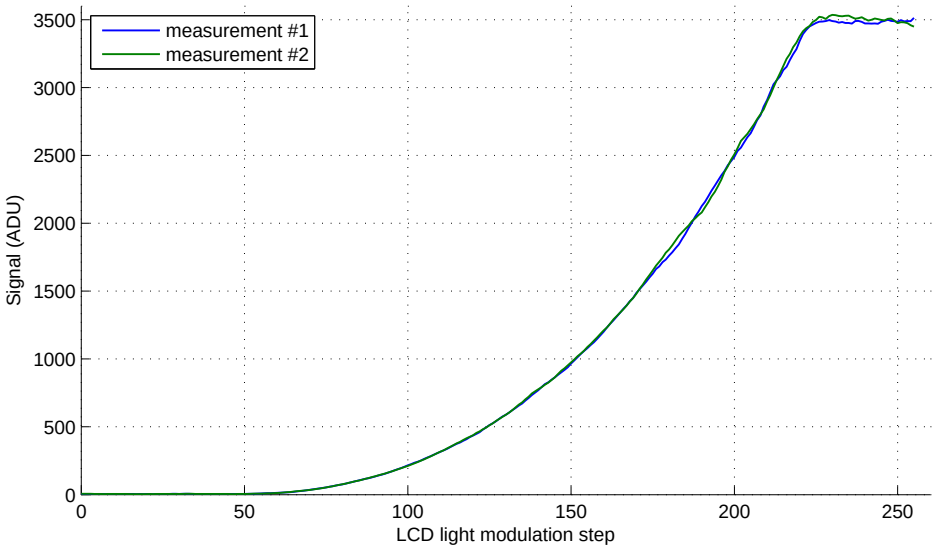

Figure 6.3. Measured light modulation dynamic range and linearity. The effective number of light modulation steps is approximately 180.

From Figure 6.3 it can be seen that the difference between the two consecutive measurements is negligible. There are saturation effects at both ends of the curve. From the same figure can also be noted the non-linear response that may be due to the gamma-factor of the graphic card.

6.4 Summary

In this chapter, the instrument breadboard adjustment procedure and characterisation measurements were reported. The adjustment procedure was a multi-phased task and included many adjustable dimensions. After that the instrument breadboard was characterised by means of spectral and spatial resolutions which agreed with the simulations quite well. The spectral resolution measurements showed that the FWHM of spectral peaks was approximately 3 nm at the wavelengths between 600 nm and 680 nm. Thus, the spectral resolution is noticeably better than required. For a modulation of 50%, the spatial frequency on the image sensor was 14.2 lp/mm and for a modulation of 20%, it was 23.6 lp/mm. The ISSI requirements given by ESA are not met due to fair modulation at the Nyquist frequency.

Also, the light modulation dynamic range and linearity measurement was carried out. As a result, the effective number of light modulation steps at this time was approximately 180 and the response was non-linear. Hopefully, future research will find a way to increase this number.

Chapter 7

Discussion and Future Work

The major advantage of the ISSI concept is instantaneous parallel optical processing. A weighted sum of the desired wavelengths over a large area can be observed simultaneously. However, usually in imaging spectroscopy the ratio between some wavelengths is computed. One idea of the ISSI is to implement the same data processing algorithms used in ground based data processing units in the on-board instrument to reduce the amount of acquired data, and especially, to reduce the data processing time so that real-time object recognition and analysis are possible. This may not be possible when only the weighted sum of wavelengths is possible to be utilised and thus, also the ratio between the sums of wavelengths should be available.

There are at least two possibilities to implement this feature. First, the spatial light modulation pattern, i.e. the pixel transmission pattern of the LCD, can be temporally switched between a few patterns to generate a set of the weighted sums of wavelengths. After that, the ratio between these sets is calculated in the on-board controller or computer. On a moving platform, aeroplane or satellite, along-track resolution is reduced and distorted because different images using different modulation patterns are taken off different ground targets. Second, two ISSI instruments could be used in parallel so that they are directed on the same target. Of course, possible misalignment between the instruments should be minimised so that the ground pixels coincide. However, this second option doubles all properties like mass, volume and power dissipation, which is not desired for the spaceborne instrument.

Possible applications for the ISSI may be the remote sensing of the Earth by means of thematic mapping of roads, water systems, forests and other objects that need to be recognised. There are also other application areas for the ISSI in addition to airborne or spaceborne remote sensing. In the paper machine industry there are many paper parameters that are monitored for example brightness, chromaticity and ink

concentration. Brightness is measured at the wavelength of 457 nm [59]. For the chromaticity measurements, a special kind of light source is needed to produce the desired spectrum of light at the wavelengths between 300 nm and 780 nm [60]. Ink concentration is measured at the wavelength of 950 nm [61]. The ISSI could be used in a multipoint measurement manner if the objective is replaced with an optical fibre bundle. Also, an image sensor could be replaced with an optical fibre bundle. Then the ISSI would be a dynamic optical filter that could be used, for example, in front of illuminance to produce the desired spectrum of light.

At this point, the ISSI concept seems quite useful and functional and thus it's suitable for further development. There are many tasks for future development. The instrument performance simulator was found to be very useful. However, the breadboard measurements should be carried out for some off-axis target positions to find the agreement with the simulations. Off-axis positions can be easily performed due to the moving capability of the already built target. The target can be moved and rotated along the swath of the instrument breadboard so that the slit is always pointing to the objective (see Appendix A.3 for the photographs).

The simulations were performed for the whole spectral range of the instrument but the measurements were carried out only for quite a narrow spectral range. This generates some modification demand for the target. The current target slit is illuminated using a neon lamp that has spectral peaks only at quite a narrow spectral range. One possibility to overcome this obstacle is to use a white light source with a number of narrow replaceable interference filters to generate spectral peaks all over the spectral range of the instrument. For example, interference filters with FWHM=10 nm at spectral separations approximately 50 nm should be adequate for the characterisation of the instrument breadboard.

Radiometric performance was simulated but not measured. Measurements for the instrument breadboard for the radiometric performance should be carried out for comparison purposes. The resolutions for the off-axis targets should be measured due to fact that the resolution is usually better in the on-axis rather than the off-axis situation.

Also some future research is needed. The inability to take ratios between the wavelengths is a major drawback of the ISSI concept at this time. Therefore, possibilities to implement this feature should be investigated. The overall performance and usefulness of the instrument would increase if it were capable of taking real-time sums and ratios of desired wavelengths.

In this work, the preliminary performance of the instrument was simulated and measured. However, in the future, the use of the instrument itself, comprehensively, should be characterised in more detail. This would require imaging experience of

natural targets acquired either in a laboratory or from an aeroplane. Preliminary characterisation results show that the instrument is capable of discriminating spectral properties of a target at quite a reasonable spatial resolution.

Chapter 8

Conclusions

The primary purpose of remote sensing is to collect information of the Earth. This information is used mainly for environmental monitoring, collecting information of natural resources and monitoring human activities. There are a number of satellites and airborne instruments that are performing data acquisition to satisfy the need of these application areas. The amount of this generated data is enormous. In fact, nowadays the major challenge of remote sensing is the management, handling and processing of this data.

In this thesis, the feasibility of a novel concept utilising on-board data processing for airborne spectral imaging was studied. The main idea of the concept is to modulate the image of scenery in the spectral and spatial domains. The purpose of this modulation is to perform on-board data processing to reduce the amount of data and, in particular, to speed up data processing to enable real-time target analysis and recognition. This kind of an instrument could be used in the data acquisition missions where the data processing algorithm is known beforehand.

Three different kinds of concepts, to solve the above-mentioned challenge, were discussed. An instrument performance simulator was developed for comparing the concepts. The most promising concept consists of two ImSpector™ spectrographs and one liquid crystal display spatial light modulator. This concept was further simulated to find airborne mission performance after which a breadboard was designed. The components used for the breadboard were studied, measured and characterised individually and the results were used in the simulations. The performance was then analysed by means of radiometric throughput and spatial and spectral resolutions. The simulations were performed at wavelengths of 450 nm to 900 nm. The throughput was found to be between 1% and 4.5%.

After that, the instrument breadboard was built, characterised and the results were compared to the simulated ones. The set-up was characterised using a neon lamp and slit at a distance of two and a half metres. The measurements were performed on-axis at wavelengths between 600 nm and 680 nm. There was good correlation between the simulations and measurements. The spectral resolution was found to be 3 nm. For a modulation of 50%, the spatial frequency on the image sensor was 14 lp/mm and for a modulation of 20%, it was 24 lp/mm. After projecting these spatial frequencies on the ground, using flying altitude of 5 km and focal length of 35 mm, the line widths were 5 m and 3 m, respectively. For flying altitude of 2 km, the corresponding line widths were 2 m and 1.2 m. The spatial resolution does not meet the requirements. The spectral resolution is, however, better than required.

The characterisation results were so promising that further development of the instrument is very probable. The results show that the concept is suitable for feature-specific airborne spectral imaging thanks to its good spectral resolution and reasonable radiometric throughput and spatial resolution.

Bibliography

[1] P. N. Slater, *Optics and Optical Systems*, ser. Remote Sensing, D. S. Simonett, Ed. Addison-Wesley, 1980.

[2] R. G. Sellar and G. D. Boreman, "Classification of imaging spectrometers for remote sensing applications," *Optical engineering*, vol. 44, no. 1, Jan. 2005.

[3] A. F. Goetz, "Imaging spectrometry for remote sensing: vision to reality in 15 years," in *Proc. SPIE Imaging Spectrometry*, M. R. Descour *et al.*, Eds., vol. 2480, June 1995, pp. 2–13.

[4] P. Shipper, "Why use hyperspectral imagery?" *Photogrammetric engineering & remote sensing*, pp. 377–380, Apr. 2004.

[5] H. Kramer, *Observation of the Earth and Its Environment*, 4th ed. Springer, 2002.

[6] E. Schanda, *Physical fundamentals of remote sensing.* Springer-Verlag, 1986.

[7] R. B. Gomez, "Hyperspectral imaging: a useful technology for transportation analysis," *Optical Engineering*, vol. 41, no. 9, pp. 2137–2143, Sept. 2002.

[8] A. Berk *et al.*, *MODTRAN4 Version 3 Revision 1*, User's manual, Air Force Research Laboratory, Feb. 2003.

[9] G. A. Shaw and H. h. K. Burke, "Spectral imaging for remote sensing," *Lincoln Laboratory Journal*, vol. 14, no. 1, pp. 3–28, 2003.

[10] M. R. Descour and E. L. Dereniak, "Nonscanning no-moving-parts imaging spectrometer," in *Proc. SPIE Imaging Spectrometry*, M. R. Descour *et al.*, Eds., vol. 2480, June 1995, pp. 48–64.

[11] R. O. Green *et al.*, "Imaging spectroscopy and the airborne visible/infrared imaging spectrometer (AVIRIS)," *Remote Sensing of Environment*, vol. 65, no. 3, pp. 227–248, Sept. 1998.

[12] F. A. Kruse, "Advances in hyperspectral remote sensing for geologic mapping and exploration," in *Proceedings 9th Australasian Remote Sensing Conference*, July 1998, p. 19.

[13] "Imaging spectral signature instrument, statement of work," Internal, ESA, p. 15, July 2005, TEC-MMO/2005/950.

[14] H. Saari, *Optics, detectors and ground-based star spectra measurements of the GOMOS Spectro-A Bench Model*, ser. VTT Publications 252. Technical Research Center of Finland, 1995, Ph.D. dissertation.

[15] J. Fisher *et al.*, "Comparison of low-cost hyperspectral sensors," in *Proc. SPIE Imaging Spectrometry IV*, M. R. Descour and S. S. Shen, Eds., vol. 3438, Oct. 1998, pp. 23–30.

[16] P. Mouroulis *et al.*, "Convex grating types for concentric imaging spectrometers," *Applied Optics*, vol. 37, no. 31, pp. 7200–7208, Nov. 1998.

[17] M. Aikio, *Hyperspectral Prism-Grating-Prism Imaging Spectrograph*, ser. VTT Publications 435. Technical Research Center of Finland, 2001, Ph.D. dissertation.

[18] "Imspector imaging spectrographs," Product brochure, Specim Ltd, Jan. 2003. [Online]. Available: http://www.specim.fi/products-imspector.html

[19] K. Mäkisara *et al.*, "Airborne imaging spectrometer for applications (AISA)," in *Geoscience and Remote Sensing Symposium, 1993. IGARSS '93. 'Better Understanding of Earth Environment', International*, vol. 2, Aug. 1993, pp. 479–481.

[20] "AISA airborne hypespectral systems," Product brochure, Specim Ltd, Mar. 2006. [Online]. Available: http://www.specim.fi/products-aisa.html

[21] J. Bland-Hawthorn *et al.*, "A tunable Lyot filter at prime focus: A method for tracing supercluster scales at $z \sim 1$," *The Astrophysical Journal*, no. 563, pp. 611–628, Dec. 2001.

[22] H. J. Masterson, G. D. Sharp, and K. M. Johnson, "Ferroelectric liquid-crystal tunable filter," *Optics Letters*, vol. 14, no. 22, pp. 1249–1251, 1989.

[23] Boulder Nonlinear Systems, "Ferroelectric liquid crystal based polarization filters," p. 5, May 2001, technical whitepaper.

[24] E. W. Weisstein. (2006, Aug.) Full Width at Half Maximum. MathWorld–A Wolfram Web Resource. [Online]. Available: http://mathworld.wolfram.com/FullWidthatHalfMaximum.html

[25] T. G. Chrien, C. Chovit, and P. J. Miller, "The development of visible and near-IR LCTF-based spectroscopic imaging system for macroscopic samples," in *SPIE Imaging Spectrometry of the Terrestrial Environment*, G. Vane, Ed., vol. 1937, 1995, pp. 256–261.

[26] C. Mao and J. Heitschmidt, "Hyperspectral imaging with liquid crystal tunable filter for biological and agricultural assessment," in *SPIE Conference on Precision Agriculture and Biological Quality*, G. E. Meyer and J. A. DeShazer, Eds., vol. 3543, Nov. 1998, pp. 172–181.

[27] J. R. Mansfield, M. G. Sowa, and H. H. Mantsch, "The development of visible and near-IR LCTF-based spectroscopic imaging system for macroscopic samples," in *SPIE Spectral Imaging: Instruments, Applications and Analysis*, G. H. Bearman *et al.*, Eds., vol. 3920, 2000, pp. 99–107.

[28] J. Olson, R. K. Jungquist, and Z. Ninkov, "Tunable multispectral imaging system technology for airborne applications," in *Proc. SPIE Imaging Spectrometry*, M. R. Descour *et al.*, Eds., vol. 2480, June 1995, pp. 268–279.

[29] W. J. Smith, *Modern Optical Engineering.* McGraw-Hill, 2000.

[30] E. S. Wachman, W. hua Niu, and D. L. Farkas, "Imaging acousto-optic tunable filter with 0.35-micrometer spatial resolution," *Applied Optics*, vol. 35, no. 25, pp. 5220–5226, Sept. 1996.

[31] T.-H. Chao, J. W. Yu, L.-J. Cheng, and J. L. Lambert, "Acousto-optic tunable filter imaging spectrometer for nasa applications: breadboard demonstration," in *Proc. SPIE Optical Information Processing Systems and Architectures II*, B. Javidi, Ed., vol. 1347, Dec. 1990, pp. 655–663.

[32] S. Yarbrough *et al.*, "MightySat II.1 hyperspectral imager: summary of on-orbit performance," in *Proc. SPIE Imaging Spectrometry VII*, M. R. Descour and S. S. Shen, Eds., vol. 4480, Jan. 2002, pp. 186–197.

[33] E. Ikonen, *Optiikan perusteet.* Helsinki University of Technology, 1995.

[34] P. Clegg *et al.*, "The ISO long-wavelength spectrometer," *Astronomy and astrophysics*, no. 315, pp. L38–L42, 1996.

[35] J. Bland-Hawthorn and D. H. Jones, "Taurus tunable filter: A flexible approach to narrowband imaging," *Astronomical Society of Australia*, no. 15, pp. 44–49, 1998.

[36] J. A. Neff *et al.*, "Two-dimensional spatial light modulators: a tutorial," in *Proceedings of the IEEE*, vol. 78, no. 5, May 1990, pp. 826 – 855.

[37] M. G. Robinson, J. Chen, and G. D. Sharp, *Polarization Engineering for LCD Projection.* Wiley, 2005.

[38] J. Antila, "Micro-electromechanical mirror for fourier transform interferometry," Master's thesis, Helsinki University of Technology, 2003.

[39] L. J. Hornbeck, "Digital light processing for high-brightness, high-resolution applications," in *Electronic Imaging, EI '97, Projection Displays III.* Texas Instruments, Feb. 10–12, 1997, p. 16.

[40] Texas Instruments, "DMD 0.7 XGA 12° DDR DMD Discovery," p. 22, Aug. 2004, product preview data sheet.

[41] Fraunhofer Institut Photonische Mikrosysteme, "Spatial light modulators," June 2006, product brochure. [Online]. Available: http://www.ipms.fraunhofer.de/en/products/lightmodulator.shtml

[42] R. D. Mayer *et al.*, "RITMOS: A micromirror-based multi-object spectrometer," in *Proc. SPIE Ground-based Instrumentation for Astronomy*, vol. 5492, Sept. 2004, pp. 200–219.

[43] J. W. MacKenty and the NGST-MOS Study Team, "NGST-MOS: A multi-object spectrometer using micro mirror arrays," final report, NASA, Sept. 1999.

[44] M. P. Christensen *et al.*, "Active-eyes: An adaptive pixel-by-pixel image-segmentation sensor architecture for high-dynamic-range hyperspectral imaging," *Applied Optics*, vol. 41, no. 29, pp. 6093–6103, Oct. 2002.

[45] G. C. Holst, *CCD Arrays, Cameras and Displays.* SPIE Optical Engineering Press, 1996.

[46] S. Kelly and M. O'Neill, *Liquid Crystals, Display and Laser Materials*, ser. Handbook of Advanced Electronic and Photonic Materials and Devices. Academic Press, 2000, vol. 7, ch. 1, pp. 1–66.

[47] Seiko Epson Corporation, "L3P05S-46G10 LCD module," p. 6, Feb. 2005, datasheet.

[48] J. Li, S. Gauza, and S.-T. Wua, "Temperature effect on liquid crystal refractive indices," *Journal of Applied Physics*, vol. 96, no. 1, pp. 19–24, July 2004.

[49] "LC-R 768 spatial light modulator," Product brochure, Holoeye, Aug. 2006. [Online]. Available: http://www.holoeye.com/spatial_light_modulator_lc_r_768.html

[50] T. Takahashi, M. Mita, H. Fujita, and H. Toshiyoshi, "Electrostatic micro-shutter array for infrared spectrograph," in *IEEE/LEOS Optical MEMs 2005 conference*, Aug. 2005, pp. 119–120.

[51] D. Mott *et al.*, "Magnetically actuated microshutter arrays," in *Proc. SPIE MOEMS and Miniaturized Systems II*, E. Motamedi and R. Göring, Eds., vol. 4561, Oct. 2001, pp. 163–170.

[52] M. Pizzi *et al.*, "Spectrometer based on MOEMS shutter array," in *IEEE/LEOS Optical MEMs 2005 conference*, Aug. 2005, pp. 179–180.

[53] Edmund Optics. (2006, July) Glan-Thompson polarizers. [Online]. Available: http://www.edmundoptics.com

[54] CODIXX AG, "ColorPol™ VIS 700 BC4 CW03 glass sheet polarizer," May 2005, product brochure.

[55] E. Hecht and A. Zajac, *Optics*. Addison-Wesley, 1974.

[56] Melles Griot. (2006, July) Microscope objectives. [Online]. Available: http://www.mellesgriot.com/pdf/X_17_9-12.pdf

[57] E. Kreyszig, *Advanced Engineering Mathematics*, 8th ed. John Wiley & John, 1999.

[58] Atmel, "Camera Link Linescan Camera AViiVA SM2 CL," June 2005, product brochure.

[59] "Brightness of pulp, paper, and paperboard (directional reflectance at 457 nm)," Official Test Method, Optical Properties Committee of the Process and Product Quality Division, 1998, T 452 om-98.

[60] "Visual grading and color matching of paper," Standard Practice, Optical Properties Committee of the Process and Product Quality Division, 1999, T 515 sp-99.

[61] "Determination of effective residual ink concentration by infrared reflectance measurement," Provisional Method, Optical Properties Committee of the Process and Product Quality Division, 1997, T 567 pm-97.

[62] "FILTER '99 Catalog Optical Glass Filter," SCHOTT Glass Technologies Inc., version 1.1US.

Appendix A

Measurement Set-up Photographs

A.1 LCD Transmission Measurement

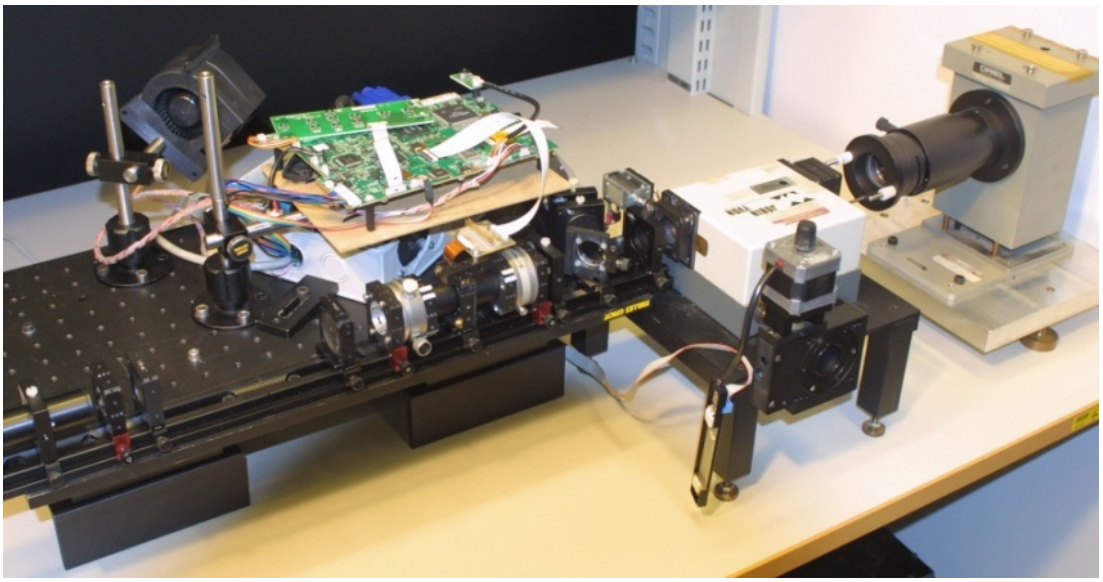

Figure A.1. Liquid crystal display transmission measurement set-up. From right to left: xenon lamp, monochromator, beam splitter and reference photo detector, focusing lens, first Glan-Thompson polariser, liquid crystal display, second Glan-Thompson polarisers, three focusing lenses and photo detector. In the background are the driver and power source for the liquid crystal display.

A.2 LCD Pixel Spatial Transmission Measurements

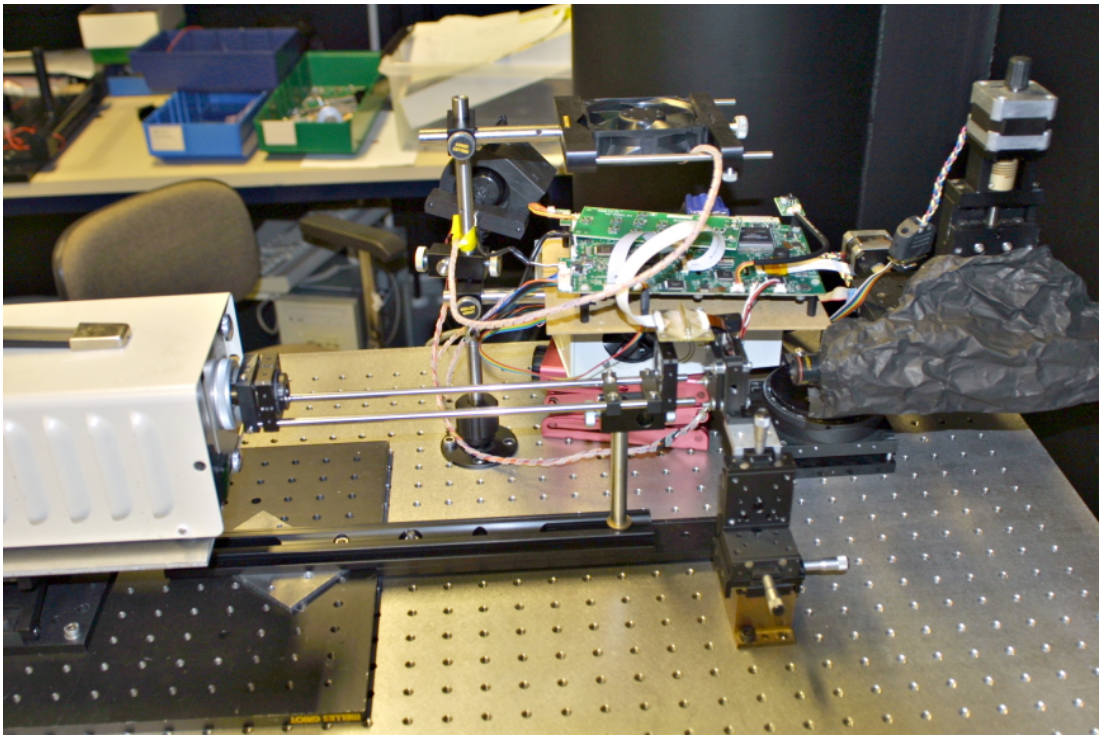

Figure A.2. Liquid crystal display pixel spatial transmission measurement set-up. From left to right: white light source, pinhole and collimating lens, liquid crystal display with sheet polarisers and microscope camera. In the background are the driver and power source for the liquid crystal display.

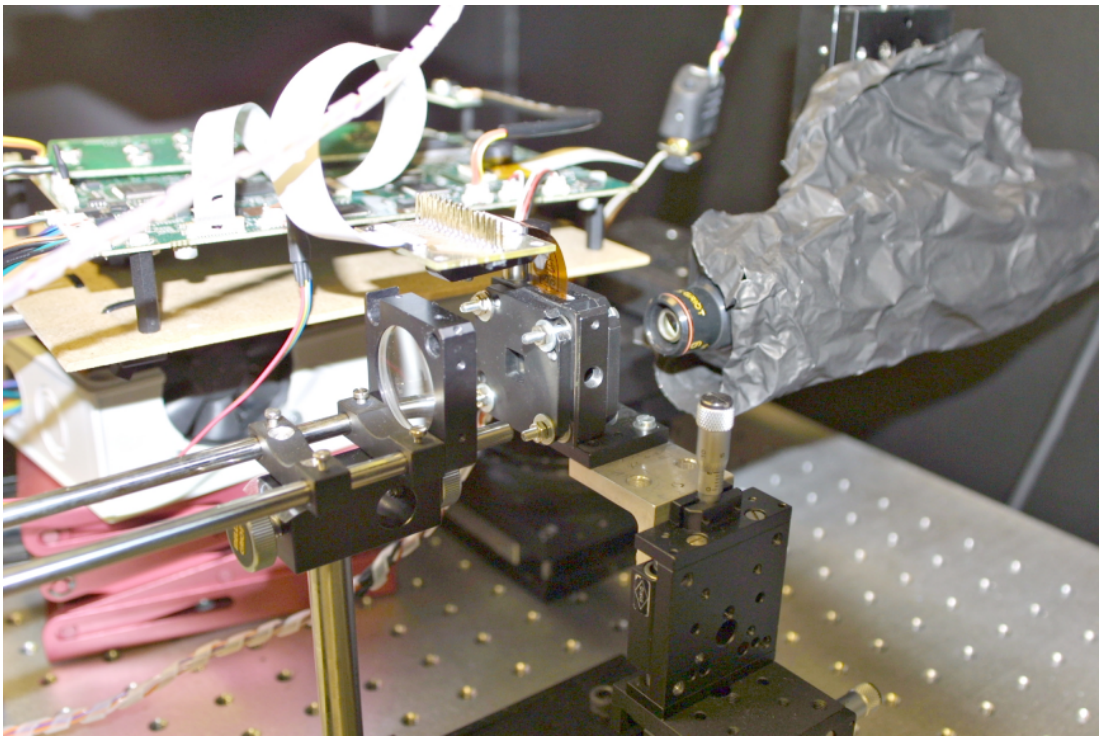

Figure A.3. Liquid crystal display pixel spatial transmission measurement set-up. Closer look of collimating lens, liquid crystal display with sheet polarisers and microscope camera in Figure A.2.

A.3 Instrument Breadboard Measurements

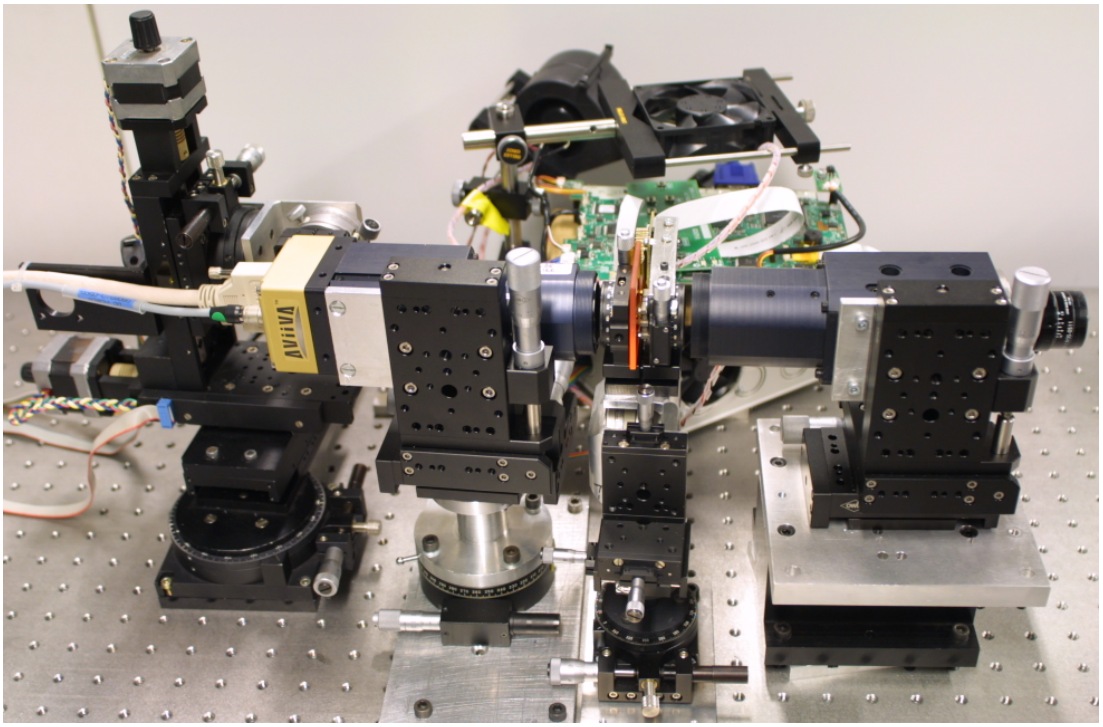

Figure A.4. Side view of instrument breadboard measurement set-up. From right to left: objective, first ImSpector™, first sheet polariser, liquid crystal display, OG550 filter, second sheet polariser, second ImSpector™ and line image sensor. In the background are the driver and power source for the liquid crystal display.

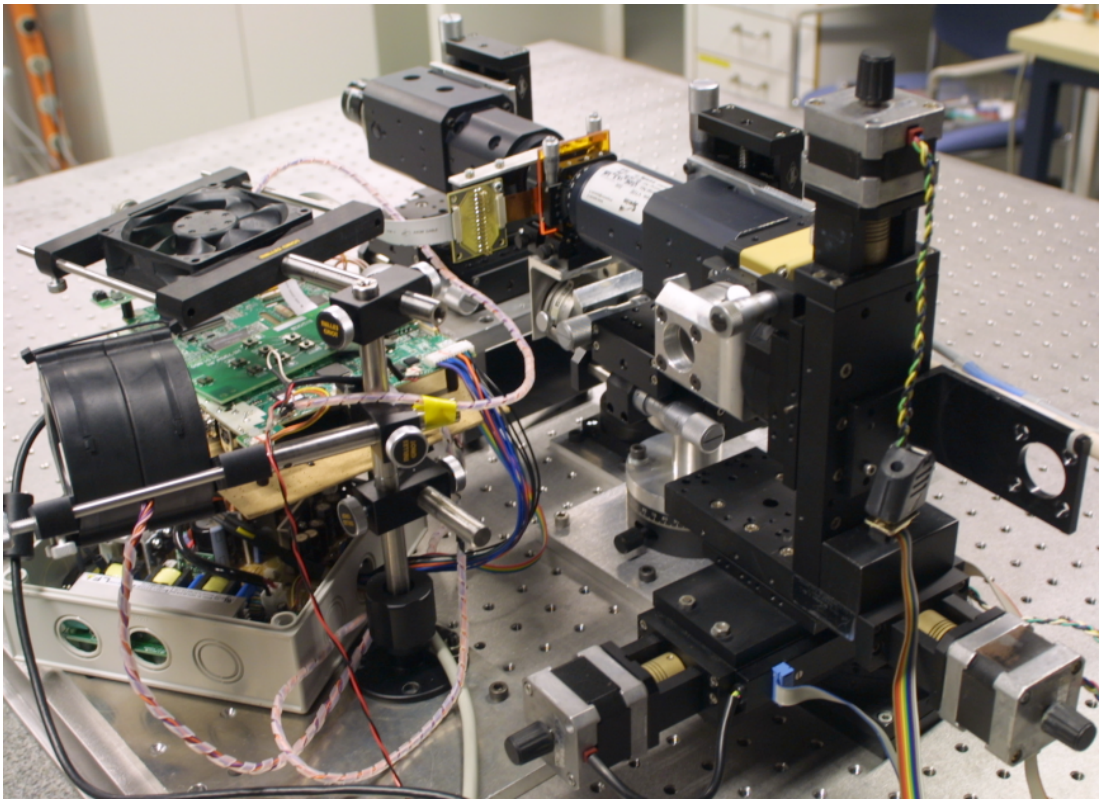

Figure A.5. Back view of instrument breadboard measurement set-up. The driver and power source for the liquid crystal display are seen more clearly.

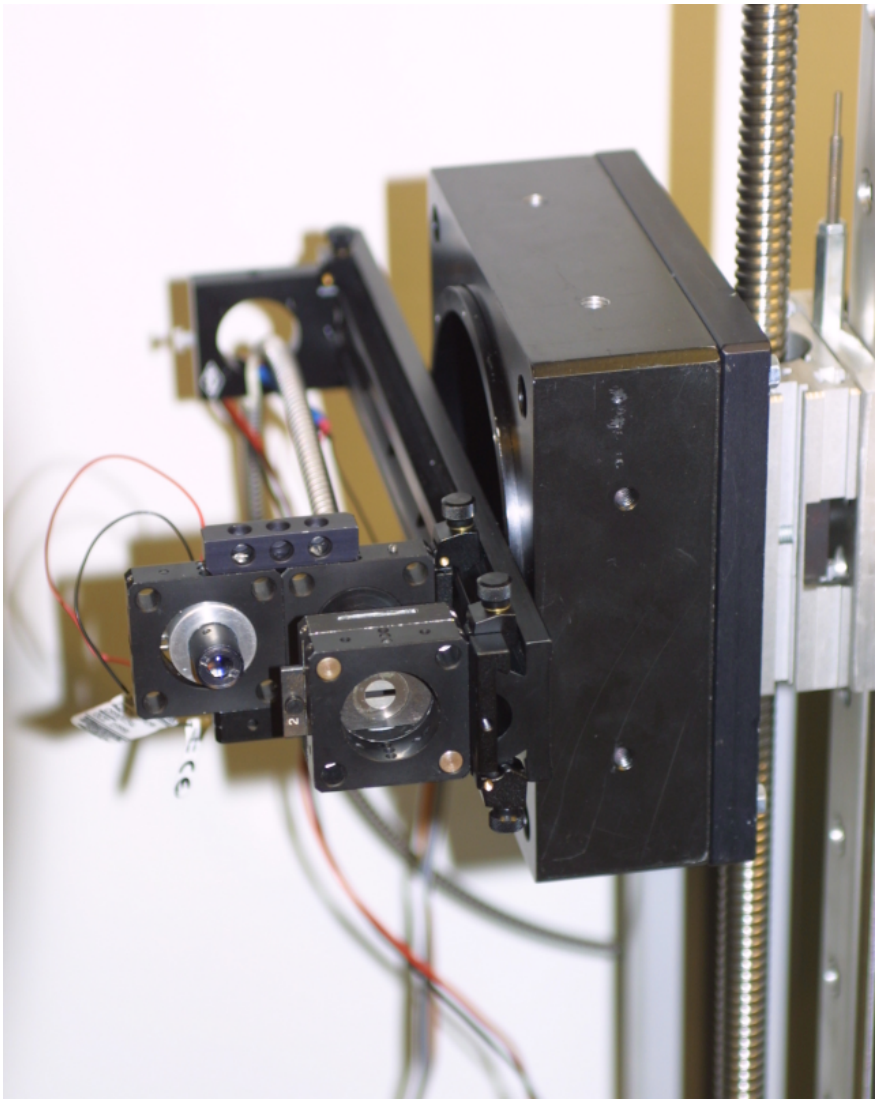

Figure A.6. Instrument breadboard target, which consist of neon lamp (not shown), fibre and replaceable slit. The target can be moved and rotated along the swath of the instrument breadboard so that the slit is always pointing to the objective. The laser is only for pointing purposes to ensure that the slit is always pointing to the objective. The distance between the target and objective was 2680 mm.

Appendix B

Parameters of Simulations

B.1 MODTRAN4 Simulation

Table B.1. MODTRAN4 simulation parameters used in Section 5.3.

Paramater	Value
Atmospheric model	Subarctic summer (60° north latitude)
Multiple scattering	enabled
Surface type	Lambertian (snow, desert, maple, urban)
Clouds or rain	none
Wind speed	0 m/s
Altitude	5 km
View angle	zenith
Latitude	60° north of Equator
Longitude	25° east of Greenwich
Greenwich time	10:00
Day of year	150
Wavelength range	350 nm - 1000 nm
Wavelength step	3 nm
Wavelength band	7 nm
Output format	Radiances (μW/sr/cm^2/nm) vs. wavelengths (nm)

B.2 Radiometric Simulation

Table B.2. Simulation parameters for radiometric simulation used in Section 5.3.

Parameter	Value
Flying altitude	5 km
Flying speed	65 m/s
Wavelength band	7 nm
Objective f-number	4
Objective focal length	35 mm
ImSpector™ slit width	30 μm
ImSpector™ slit height	12 mm
ImSpector™ dispersion	97.5 nm/mm
LCD pixel pitch	14 μm
LCD spatial pixels	800
LCD spectral pixels	600
Image sensor pixel pitch	14 μm
Image sensor camera gain	10 e/ADU
Image sensor read-out noise	30 e
Image sensor dark current	300 e/s
Image sensor integration time	20.0 ms

Table B.3. Calculated parameters for radiometric simulation used in Section 5.3.

Parameter	Value
FOV	18.18°
IFOV along-track	0.0491°
IFOV across-track	0.0229°
GSD along-track	4.29 m
GSD across-track	2 m
Objective diameter	8.8 mm
LCD spatial image height	11.2 mm
LCD spectral image height	8.4 mm
LCD spectral sampling	1.37 nm/pixel
Pixels per bandwidth of FWHM=7 nm	5.1

Appendix C

Measurement Results

C.1 ImSpector™ Measurements

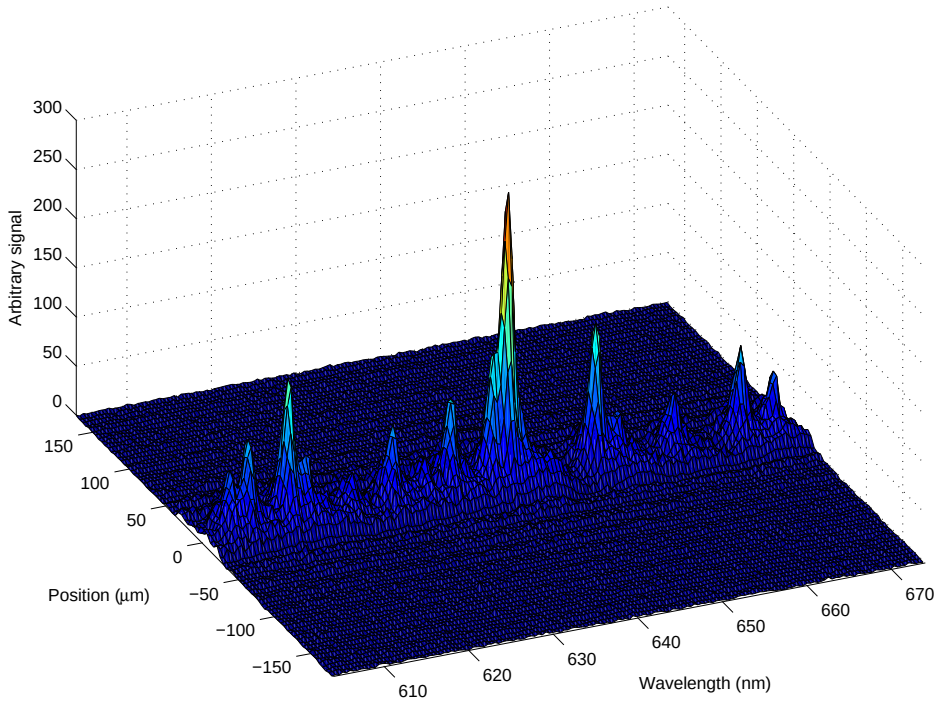

Figure C.1. 3D illustration of output image of ImSpector™ shown in Section 4.3.

Appendix D

Filter Information

D.1 Transmissions of Filters

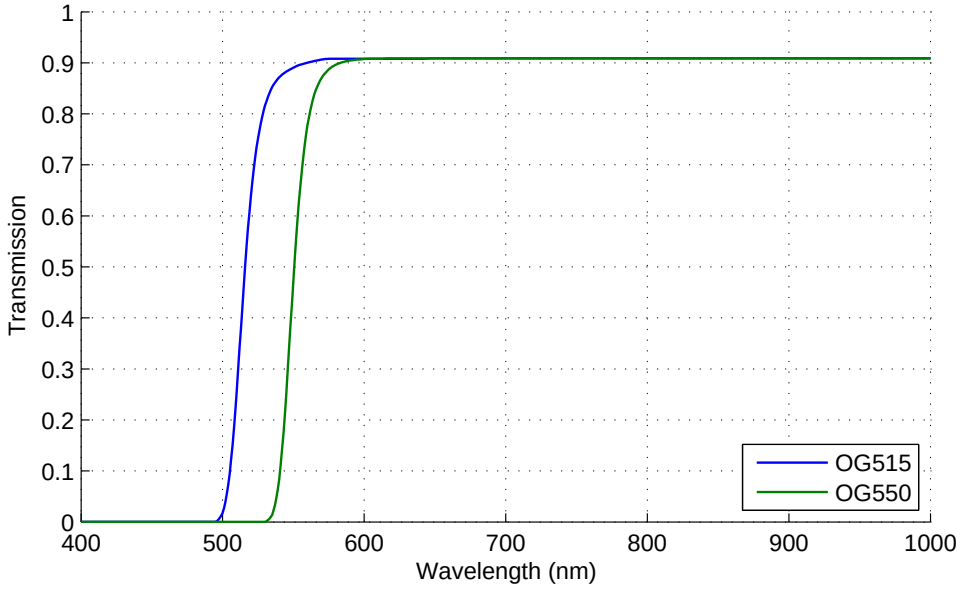

Figure D.1. Transmissions of OG515 and OG550 filters [62].